Synthesis, Fabrication of Graphene Oxide Membranes, and Controlling their Diffusion by Thermal Reduction

by

Abdulrahman Alhadhrami

A thesis
presented to the University of Waterloo
in fulfillment of the
thesis requirement for the degree of
Doctor of Philosophy
in
Chemistry

Waterloo, Ontario, Canada, 2016

AUTHOR'S DECLARATION

I hereby declare that I am the sole author of this thesis. This is a true copy of the thesis, including any required final revisions, as accepted by my examiners.

I understand that my thesis may be made electronically available to the public.

Abstract

Graphene and graphene oxide have many applications in different fields such as electronic devices, electrochemical energy storage, catalysis, polymer composite, and liquid crystal devices. Oxidation of graphite to graphite oxide permits the separation of its newly formed graphene oxide molecular layers. Graphene oxide, easily deposited in the form of a film through vacuum filtration, can be partially reduced by various methods to imperfectly restore the π-network system of graphene. Reduced graphene oxide (rGO) films possess functional properties with practical applications. The main objective of this research is to carry out controlled extents of thermal reduction of graphene oxide to manipulate the d-spacing of the layers within the partially reduced films to optimize their characteristics with respect to metal ion diffusion across the films. In addition to this main objective, several other features of rGO were explored, including mechanical properties and electrical conductivity. Since GO is an electrical insulator, thermal or chemical reduction methods must be utilized in order to make it electrically conducting. Both of these methods have been used in this thesis.

In the first project, the primary aim of this work, reduction of GO films was done via thermal treatment (60, 180, 200, 225, 250, and 300 $^{\circ}$C) and also by ascorbic acid as well as hydrazine vapour. Chemical cross-linking (Na^{+}, Mg^{2+}, Ba^{2+}, Fe^{2+}, Fe^{3+}) was performed to explore the reduction in the d-spacing between reduced GO layers. Tensile strength test was conducted on non-reduced and the GO films reduced at different temperatures to investigate their strength. In the second project, thermally reduced GO films were used in diffusion studies of 100 mM NaCl and 100 mM $CaCl_2$. Current-voltage measurements were also conducted on these films to investigate the impact of the change in the d-spacing by thermal treatment on their electrical conductivity.

In the third project, ZnO nanorods were grown on GO film by hydrothermal method and colloidal ZnO as well as GO-ZnO composite were prepared and then used in photodegradation of methylene blue as organic pollutant.

In the forth project, ZnO nanorods were incorporated between reduced GO layers so that they would segregate the reduced GO layers to provide a large surface area, after which manganese divalent ions were added to form manganese dioxide so that greater charge can

be stored, hence increasing the capacitance of these films for energy storage. Finally, surface potential was applied to these films to explore its influence on the diffusion of 100 mM $CaCl_2$ through different thermally reduced GO films.

Based on the results, the d-spacing for GO films was reduced from 7.36 to 4.59 Å on increasing the temperature of thermal reduction from 60 °C to 250 °C. This impacts both the in-plane and out of plane electrical conductivity of the GO films and also their diffusion characteristics. The in-plane electrical conductivity increases by over seven orders of magnitude between 60 °C and 250 °C, and the out-of-plane electrical conductivity also increases by over six orders of magnitude. Similarly, the diffusional resistance for NaCl increases by over 500 times and that of $CaCl_2$ by over 60 times.

Powder XRD, SEM, FTIR spectroscopy, Raman spectroscopy, XPS, UV-vis spectroscopy, and TGA were conducted to confirm the phase, morphology, reduction, and thermal stability of these films.

Acknowledgements

First of all, I would like to express my deep thanks to my supervisor Prof. Vivek Maheshwari for his invaluable guidance, support, motivation, and critical comments. He has opened many avenues in my research career which in turn will be reflected in my future academic career.

I would also like to thank my supervisory committee: Prof. Juewen Liu, Prof. Frank Gu, and Prof. Eric Prouzet for their guidance and participation. Their advice was truly significant. Special thanks go to my external examiner Prof. Lee Wilson for taking the time to come to Waterloo and participate in my thesis defense.

I would also like to thank my great lab mates for their support and their encouragement. It has been a privilege to have worked with them. They are: Long Pu, Shehan Salgado, Abdullah Abbas, Maarij Baig, and Huayi Gao.

Special thanks go to our crystallographer in the department Dr. Jalil Assoud. I would like to thank my wonderful family, my wife, and my daughter Hoor. They have been wonderfully supportive.

Finally, I would like to extend my appreciation and my deep thanks to the Saudi Cultural Bureau in Ottawa, Ministry of Education in Saudi Arabia, and Taif University for their scholarship to pursue my graduate studies in Canada. I am extremely grateful for them.

Dedication

I dedicate this thesis to my family, my wife, and my daughter.

Table of Contents

List of Figures

List of Tables

List of Abbreviations

GO	Graphene Oxide
σ	Electrical Conductivity
R	Resistance
PXRD	(Powder) X-ray Diffraction
SEM	Scanning Electron Microscopy
FT-IR	Fourier Transform Infrared
XPS	X-ray Photoelectron Spectroscopy
ESCA	Electron Spectroscopy for Chemical Analysis
E_b	Binding Energy
E_k	Kinetic Energy
ω	Work Function
$h\nu$	Photon Energy
UV-Vis	Ultraviolet Visible
TGA	Thermal Gravimetric Analysis
DMTA	Dynamic Mechanical Thermal Analyzer
rGO	Chemically reduced Graphene Oxide
TrGO	Thermally reduced Graphene Oxide

Chapter 1. Introduction to Graphite Oxide, Graphene Oxide, and Graphene

1.1 Purpose of Research

Graphene, graphene oxide, and their derivatives are currently the subject of a great deal of research, both in terms of their fundamental physical, chemical, and materials science properties, as well as the exciting promise of their practical applications in diverse fields.[1,2,3,4,5,6,7,8,9,10,11] The tuning of defects in graphene based materials is of interest for application in several areas. The remarkable potential of graphene-based technologies has prompted us to explore several areas of application centered around the controlled reduction of graphene oxide to varying degrees and consequently also a partial restoration of its π network system.[12,13,14,15] The imperfect restoration of graphene oxide and its consequence for the functional properties of the resulting macroscopic material is the basis of our attempt to control its behavior in several applications.

A cost-effective method is required for producing sufficient quantities of graphene based materials for use in practical applications and for our research. The solution-based method of Hummer`s and its modified protocols is one such route that starts with inexpensive graphite and results in the formation of solubilized and exfoliated graphene oxide sheets. The large quantities of the material generated as a result permit us to make macroscopic films of graphene oxide with ease.

In this work, graphene oxide films were reduced chemically and thermally; thermal reduction was selected as the more suitable method for our studies. The main purpose of this research is to carry out controlled thermal reduction of graphene oxide films to manipulate the d-spacing between the graphene sheet layers within the partially reduced films. We then use the

control over d-spacing to study its affect on the diffusion properties of these films, which is crucial for their application in water desalination. In addition, several other areas, both fundamental and practical, were explored, among them: d-spacing control through chemical reduction or chemical cross linking; film tensile strength determinations; film electrical property studies; organic pollutant photodegradation through ZnO nanorod deposition on graphene oxide films; increasing capacitance of graphene oxide films through ZnO nanorod or divalent manganese ions introduction, for the purpose of energy storage; and, the influence of surface potential on these films to hinder the diffusion of $CaCl_2$ solutions.

This chapter explores the background and history of graphite oxide and graphene, various methods of reduction, characterization techniques, and electrical and diffusion properties of graphene oxide membranes.

1.2 History of the Synthesis of Graphite Oxide

Synthetic Approaches

Graphite oxide has a significant history starting in 1859 with the British Chemist B.C. Brodie, who investigated the structure of graphite for the synthesis of graphene oxide (GO) by adding species of potassium chlorate ($KClO_3$) to a slurry of graphite in fuming nitric acid (HNO_3).[12] Brodie was able to determine that carbon, hydrogen, and oxygen were present in the resulting material. Brodie proved that graphite could be oxidized if it was treated with oxidizing agents. In 1898, L. Staudenmaier made a slight change to enhance the oxidation process of graphite by adding concentrated sulfuric acid (H_2SO_4), fuming nitric acid (HNO_3) and adding potassium chlorate ($KClO_3$) over the reaction. By increasing the activity of the mixture, Staudenmaier increased the degree to which GO became oxidized.[13] In 1958, Hummers introduced an alternative oxidation method, which is the most commonly used nowadays,[14] by

employing a mixture of potassium permanganate ($KMnO_4$) with concentrated sulfuric acid (H_2SO_4) and sodium nitrate ($NaNO_3$) to oxidize graphite.

Nitric acid, which is used in both the Brodie and Staudenmaier methods, is being used as an oxidizing agent (e.g. aqua regia). Aromatic carbon surfaces are capable of reaction with nitric acid producing different oxygen containing functional groups such as carboxyl, hydroxyl, and epoxy.[15] Similarly, potassium chlorate is another oxidizing agent acting as the reactive species. Likewise, potassium permanganate is another oxidizing agent (e.g. dihydroxylations). Some toxic gases such as NO_2, N_2O_4, and ClO_2 are generated in all the aforementioned methods,[15] consequently, basic precautions must be taken into account. Natural graphite can be divided into micro-crystalline and macro-crystalline in terms of the size of crystallite.[16] Micro-crystalline graphite or amorphous graphite has lower purity and crystallinity which influences its conductivity and lubricating properties and which make it inappropriate for electrochemical applications. Macro-crystalline graphite, on the other hand, has two forms, vein and flake. Flake graphite comprises large crystals which are oriented uniformaly, and are of high purity, which make it the most well-known source for graphite used in oxidation reactions. Many localized defects exist in the π-structure of flake graphite`s which assist the oxidation process.[15] Dimanganese heptoxide (Mn_2O_7), which is produced in the Hummers method, has the ability to selectively oxidize unsaturated aliphatic double bonds over aromatic double bonds in styrene, which was reported by Trömel and Russ.[15] If their claims could be applied to graphite then it is probable that the aromatic system is not susceptible to oxidation. The clarification of precise oxidation mechanisms is rather challenging due to the complicated structure of graphite in addition to its defects.[15] Dimanganese heptoxide (Mn_2O_7) dark red, indeed, is the active species. Reaction between potassium permanganate and concentrated sulfuric acid would form dimanganese heptoxide as it shows in the following equation:[15]

$$KMnO_4 + 3H_2SO_4 \rightarrow K^+ + MnO_3^+ + H_3O^+ + 3HSO_4^- \quad \textbf{(1.1)}$$

$$MnO_3^+ + MnO_4^- \rightarrow Mn_2O_7 \quad \textbf{(1.2)}$$

1.3 Structural Model of Graphene Oxide

Several structural models have been proposed by different scientists, all of which involve regular lattices comprising distinct repeat units. Their suggestions are different in terms of the existence of some particular oxygen functional groups in the basal plane of GO or the hybridization of the involved carbon atoms. Fig. 1.1 depicts the proposed structural models. Hofmann and Holst`s structure assumed a net molecular formula of C_2O and the epoxy groups are spread over the basal planes of graphite.[15] In 1946, Russ suggested addition of hydroxyl groups into the basal plane, which in turn, altered the hybridization of the carbon atoms from sp^2 to sp^3. In 1969, Scholz and Boehm proposed taking away the epoxide and ether groups and quinoidal species were substituted regularly in their model.[17] Nakajima and Matsuo have assumed their lattice framework analogous to poly (dicarbon monofluoride), $(C_2F)_n$, which introduces intercalation to the graphite structure.[18]

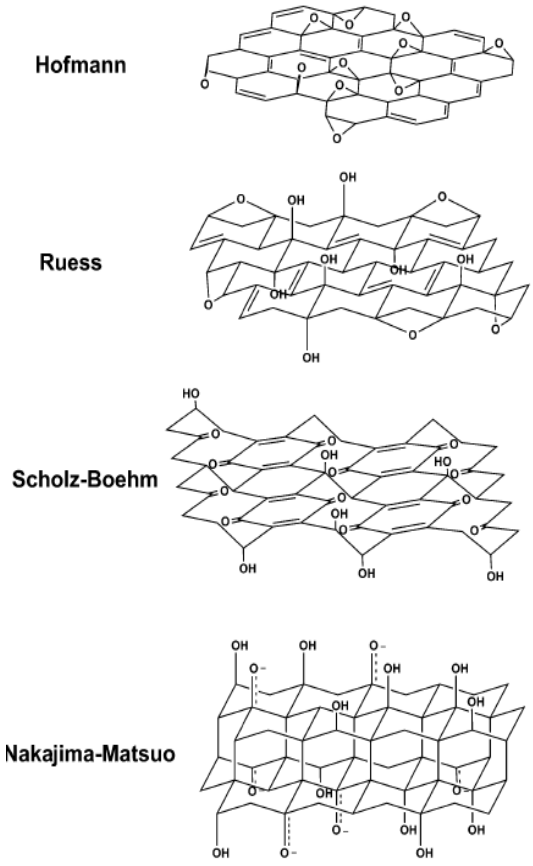

Fig. 1.1: Older structural models of GO (taken from ref.[19] with permission from American Chemical Society).

Recently a non-stoichiometric amorphous model has been reported by Anton Lerf and Jacek Klinowski [20] (Fig. 1.2). Lerf had investigated some of GO derivatives and structural features have been isolated in terms of the reactivity of the material.[21]

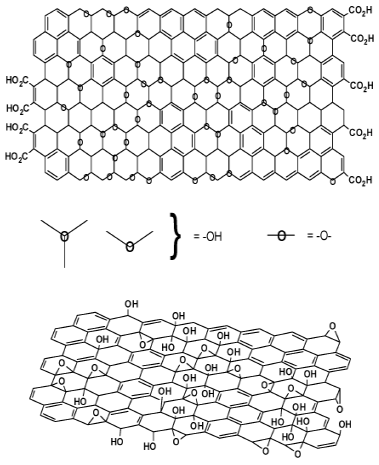

Fig. 1.2: Lerf- Klinowski structural model of GO (top, taken from ref.[20]; bottom, taken from ref.[21] both with permission from American Chemical Society).

Lerf and coworkers were able to find out the distribution of functional groups such as epoxy and hydroxyl through hydrogen bonding interactions with water. The GO and water had strong interactions via hydrogen bonding in which the stacked structure of GO is maintained. Fig. 1.3. This interaction supports the approach for the modified Hummers method. Brodie, Lerf and his workers had noticed that GO was thermally unstable, CO and CO_2 are released instead of O_2. This is because of the presence of the active surface species in GO.

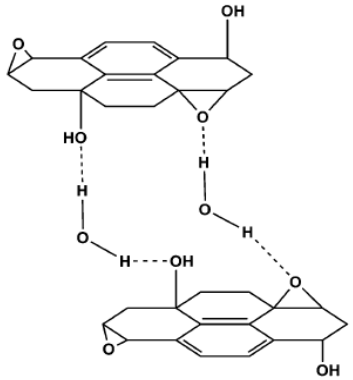

Fig. 1.3: Hydrogen bonding network formed between oxygen functional groups between GO and water (taken from ref.[15] with permission from Royal Society of Chemistry).

Dékány and coworkers have supported the Ruess and Scholz-Boehm models by revising their model. They did not assume the existence of the carboxylic groups in the GO.[15] Fig. 1.4:

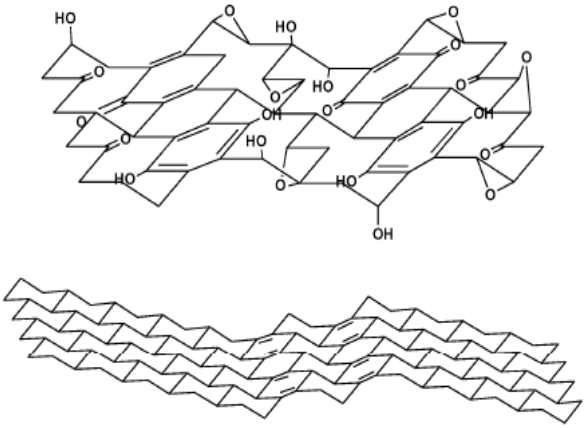

Fig. 1.4: Proposed model of GO by Dékány and coworkers (taken from ref.[19] with permission from American Chemical Society).

It can be concluded that the oxidation degree would cause significant variation in the structure of graphite which would influence its properties.

1.4 Properties of Graphene and Graphene Oxide

Due to remarkable mechanical, electrical, thermal, and optical properties, graphene has inspired researchers in many fields. It is a flat single layer of carbon atoms, sp^2 hybridized and bonded into a two-dimensional (2D) honeycomb lattice with single carbon atom thickness.[22] It has a large theoretical specific surface area (2630 m^2g^{-1}),[22] high intrinsic mobility (200,000 $cm^2v^{-1}s^{-1}$),[23] high Young`s modulus (~1,100 GPa),[22] fracture strength (125 GPa),[22] thermal conductivity (~5000 $Wm^{-1}K^{-1}$),[23] excellent transport phenomena such as room temperature quantum effect and high optical transmittance (~97.7%).[23,24] Graphene was first isolated by Scotch tape in 2004 by two Russian researchers at the University of Manchester, Andre Geim and Kostya Novoselov.[25] In 2010, they were awarded the Nobel Prize in Physics for their breakthrough in the isolation of graphene and the determination of its properties.[9] Graphene is

the thinnest known material.[11] Graphene and its derivatives (chemically modified graphene) have many applications in electronic devices such as solar cells,[26] electrochemical energy storage such as supercapacitors,[27] hydrogen storage,[28] catalysis,[29] transistors,[30] polymer composites,[10] liquid crystal devices,[31] and mechanical resonators.[32] Graphene can be synthesized by four different methods:[22] 1- chemical vapor deposition (CVD).[33,34] 2- micromechanical exfoliation of graphite,[25] 3- epitaxial growth on electrically insulating surfaces such as SiC.[35] 4- chemical reduction of GO.[36, 37, 38] The real advantage of using either CVD or chemical reduction of GO is to produce a large amount of graphene whereas micromechanical exfoliation produces a small amount of graphene.[22] Reduced graphene oxide is produced from graphite oxide by one of the three oxidative methods: (Brodie,[12] Staudenmaier,[13] or Hummers[14]) followed by chemical reduction to form chemically reduced graphene oxide. In all of them, graphite is being oxidized by strong acids and oxidants. The degree of oxidation is the only difference between these methods. The chemical structure of graphite oxide was revealed by solid-state ^{13}C NMR spectroscopy, and is shown in Fig. 1.5:

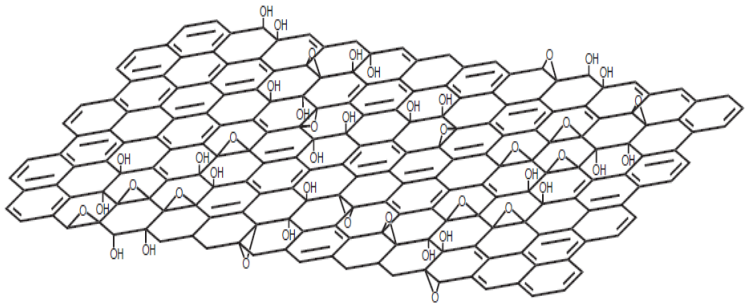

Fig. 1.5: Chemical structure of graphite oxide[Lerf model] (taken from ref.[22] with permission from Nature Publishing Group).

It can be seen that the sp^2 hybridized carbon atoms form a network with defects arising from the functional groups introduced during the oxidation process disrupting this network. A fraction of hydroxyl and epoxy groups are distributed in the basal plane and another fraction of carboxylic

or carbonyl groups are present at the edge of the graphite oxide.[22] Graphite oxide comprises a layered structure of graphene oxide sheets. The presence of oxygen-containing functional groups leads to its hydrophilicity.[39] A suspension of graphene oxide can be produced by exfoliation of graphite oxide via simple sonication.[40] Graphene oxide sheets have negative charge when they are dispersed in water, which has been determined by the measurements of zeta potential (i.e. surface charge of graphene oxide sheets).[39] This accounts for the stability of aqueous suspensions in which there is a repulsion between the negative charges of the graphene oxide. Some researchers have claimed that simple sonication of graphite oxide in aqueous and organic solvents can produce homogenous colloidal suspensions of graphene oxide.[41, 40,42,43,44] . Since graphene oxide is hydrophilic, it can be dispersed in water. The color of the resulting suspension is brown to dark brown depending on the concentration of graphite oxide in the required solvent.[41,40,42,43,44] Fig. 1.6 depicts the difference in the color of the suspension:

Fig. 1.6: Effect of the concentration on the colour of the suspensions. Right is 0.1 mg / ml. Left is 2 mg / ml.

The thickness of a single reduced graphene oxide sheet is ~1 nm height on a mica substrate, which was determined by atomic force microscopy (AFM).[22] Some polar solvents can be used for the dispersion of graphite oxide such as ethylene glycol, DMF, and THF.[22]

Graphene oxide can be chemically reduced by the following reducing agents: hydrazine,[36,37] cellulose,[45] sodium borohydride ($NaBH_4$),[46,38] HI,[47,48] dimethylhydrazine,[10] hydroquinone,[49] Vitamin C,[50] and alkaline solutions.[51] It could also be reduced by thermal,[52,53] and ultraviolet assisted methods.[54] Despite the fact that the reduced graphene oxide sheets develop unavoidable structural defects during the reduction process, they possess beneficial qualities such as catalytic properties, high conductivity, and mechanical strength.[24]

Due to the interrupted sp^2 bonding in the network of graphite oxide, it is an electrically insulating material, and by reduction using chemical agents, thermal treatment, or UV exposure, electrical conductivity can be partially restored.[15] Sonicating and/or stirring graphite oxide in water is a common method of exfoliation.[15] One of the most significant reactions of graphene oxide is its reduction, as it allows scientists and engineers to utilize graphene in large scale applications such as energy storage.[15]

1.5 Reduction Methods of Graphene Oxide

Reduction can be done by chemical, thermal, or electrochemical methods. All of these methods provide products which, to various extents, approach graphene in terms of electrical, thermal, and mechanical properties.[15] Hydrazine monohydrate is one of the most common reducing agents that has been used to reduce graphene oxide to graphene. The oxidation of graphite to graphene oxide and its subsequent reduction with hydrazine is illustrated in Scheme 1.7:

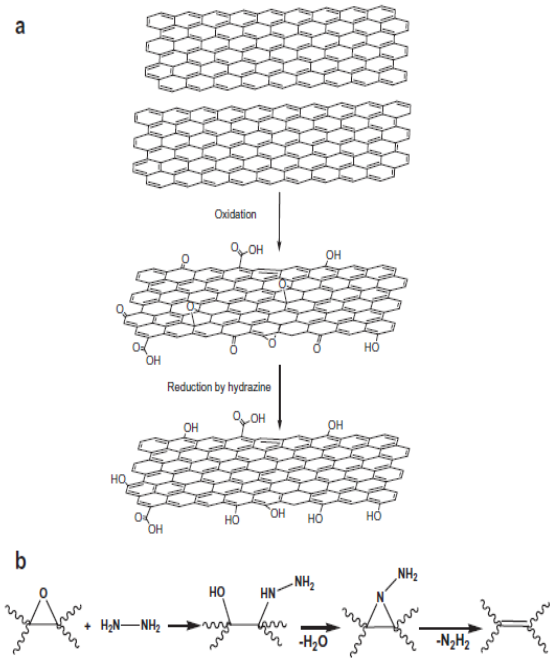

Fig. 1.7: a. Oxidation of graphite to graphene oxide and reduction to reduced graphene oxide. b. A proposed reaction pathway for reduction of epoxide by hydrazine (taken from ref.[9] with permission from Elsevier).

During the reduction process, the brown colour of the graphene oxide dispersion is turned to black upon addition of hydrazine, after which the reduced graphene sheets aggregated and precipitated.[44,40] The removal of oxygen atoms causes the reduced graphene oxide to become less hydrophilic, resulting in its precipitation.[9]

Another approach to reduce graphene oxide is by heat treatment that removes the oxygen containing functional groups on its surface.[9] The stacked graphene oxide is exfoliated and reduced by heating it to 1050 $^{\circ}$C, which has been done by Aksay`s group. During the heating process, oxide functional groups are expelled as carbon dioxide.[52,53] The authors reported that when the decomposition rate of the oxygen functional groups exceeds the diffusion rate of the evolved gases, exfoliation takes place due to pressures higher than the van der Waals forces which hold the graphene sheets together.[9] To separate graphene oxide

sheets, a pressure of 2.5 MPa is required, however, the exfoliation generates pressures 1–2 orders of magnitude higher.[9] According to the AFM studies, 80% single layer reduced graphene oxide can be produced via thermal reduction and exfoliation. Approximately 30% mass loss, vacancies, and defects result upon the removal of the oxide groups which can affect the mechanical and electrical properties of the reduced graphene oxide.[9]

1.6 Chemical cross-linking of Graphene Oxide Sheets

One of the most significant themes in recent graphene-based research is to explore changes in physicochemical properties of graphene, graphene oxide, and its derivatives.[55,56] Divalent cations can be used as cross-linkers between graphene oxide sheets leading to a change in the mechanical properties and inter-layer spacing of GO membranes. The chemical interactions occur between the oxygen-containing functional groups and the cations.[41,57] The interaction can occur either via binding of the cross-linker ions to the carboxylic acid groups at the edges of the graphene oxide sheets, or via introduction of the cross-linker ions into the ring of epoxides.[41] The two models are shown in Fig. 1.8:

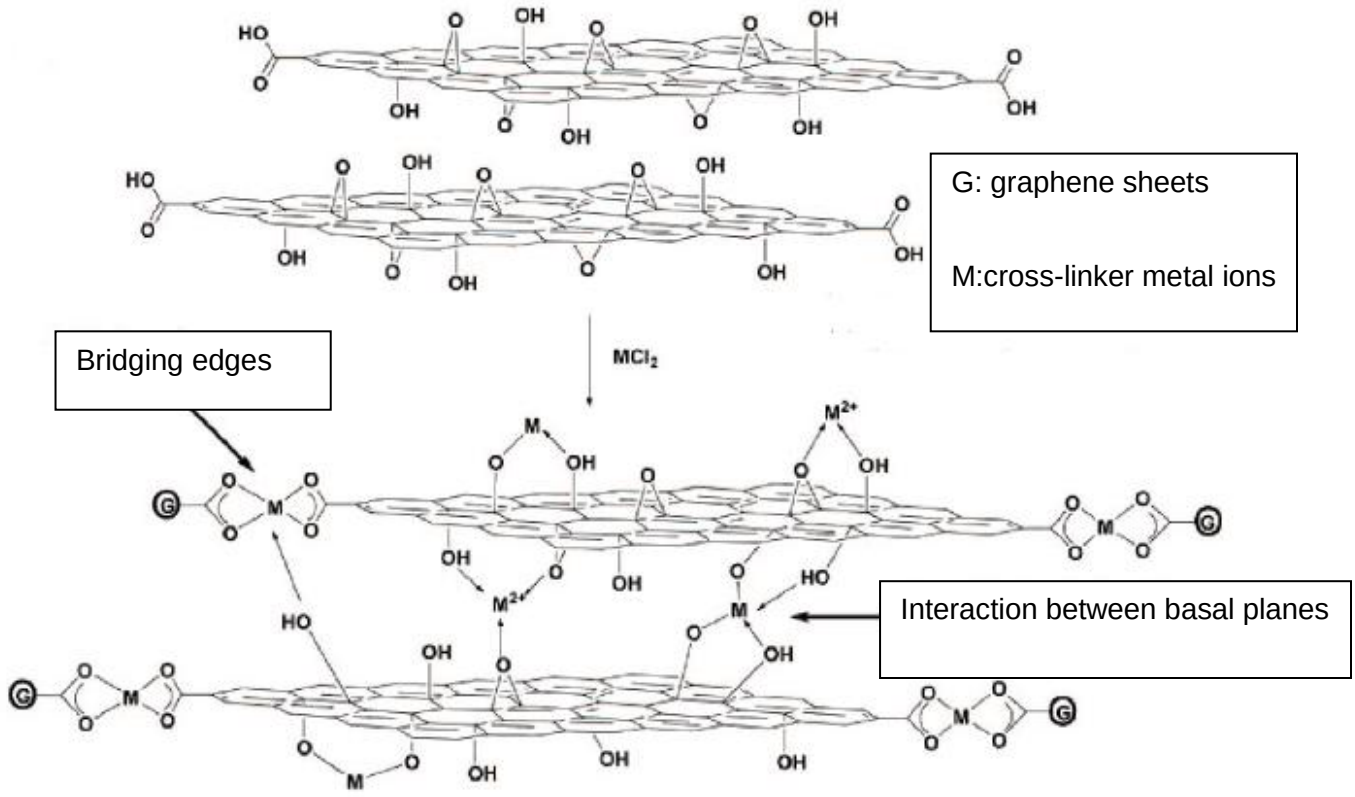

Fig. 1.8: Schematic model of the interaction between GO and metal ion cross-linkers (taken from ref.[41] with permission from American Chemical Society).

As mentioned earlier, the graphene oxide sheets interact with metal ions in two different binding modes. The stronger mode in which the metal ions bind tightly to carboxylic acid groups at the edges of the graphene oxide sheets leads to cross-linking of neighboring sheets, and improves the mechanical stiffness of the graphene oxide membrane. On the other hand, the weaker mode, in which the metal ions introduced to epoxides have the effect of opening the ring and then facilitating the interaction of additional metal ions between the graphene oxide sheets, leads to an increase in d-spacing. The first one can resist distortions between sheets; however, the second one cannot resist such deformations. As the metal ions enter between the graphene oxide sheets, they increase the d-spacing and the cross-sectional area of the modified

graphene oxide sheets, which leads to a decrease in the stress. The size of the metal ions plays a crucial role in the mechanical properties of the modified graphene oxide sheets. For instance, Mg-modified graphene oxide has E_E (maximum modulus in the linear region) = 24.6 $\pm$ 1.4 GPa. On the other hand, the Ca-modified graphene oxide has E_E = 21.5 $\pm$ 1.5 GPa. This is because calcium has a larger ionic radius than magnesium. The proposed model leading to enhanced mechanical properties of the modified graphene oxide sheets is shown in Fig. 1.9:

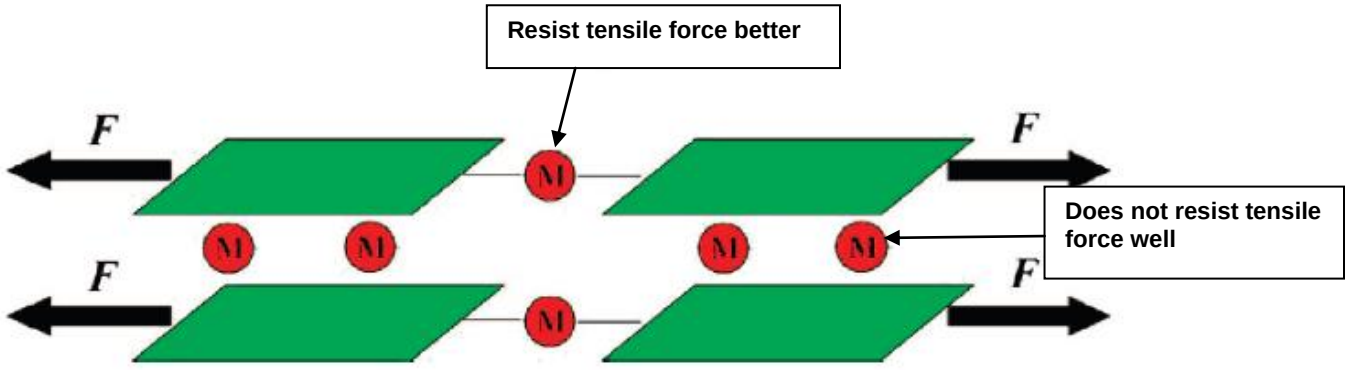

Fig. 1.9: Proposed model for the enhanced mechanical properties of graphene oxide sheets after metal ions modifications (taken from ref.[41] with permission from American Chemical Society).

Novoselov et al. have reported that the interaction between metal ions and graphene depends on the layer number of graphene. The splitting in G band decreases with increases in the number of graphene layers: single-layer $>$ bilayer $\geq$ trilayer. Since the G band was supposed to be a factor for determination the interaction between graphene and metal.[57]

1.7 Characterization Techniques of Graphene Oxide

There are various techniques that are used for characterization the properties of the reduced product and the starting material such as the measurement of the surface area [S. Brunauer, P. H. Emmett, and E. Teller surface (BET surface)]. Raman spectroscopy is another technique which can be used to differentiate between unreduced and reduced material. Each band in Raman corresponds to a specific characteristic of the material. For instance, the D band

is an indicator of the order and disorder of the system. The G band represents the stacking structure of the material. Both of these bands are the main vibrational modes in graphitic structures.[15] The number of layers in graphene and the stacking behavior can be determined by the ratio of the intensities of the two bands (D/G). High degree of exfoliation or disorder is referred to high D/G ratios.[15]

The electrical properties of the material can be characterized by measuring its resistance or conductivity, given by the following equation:[15]

$$R_{sh} = \frac{1}{\sigma t} \qquad \textbf{(1.3)}$$

Where $\left(\sigma, Sm^{-1}\right)$ is a bulk conductivity, $\left(R_{sh}, \Omega sq^{-1}\right)$ is sheet resistance, t is the thickness of the sample.

Other techniques such as Atomic force microscopy (AFM), X-ray photoelectron (XPS), scanning electron microscopy (SEM), transmission electron microscopy (TEM), and X-ray diffraction (XRD) have been used for characterization of graphene oxide. The XPS spectrum of the graphene oxide and reduced graphene oxide via hydrazine are illustrated in Fig. 1.10:

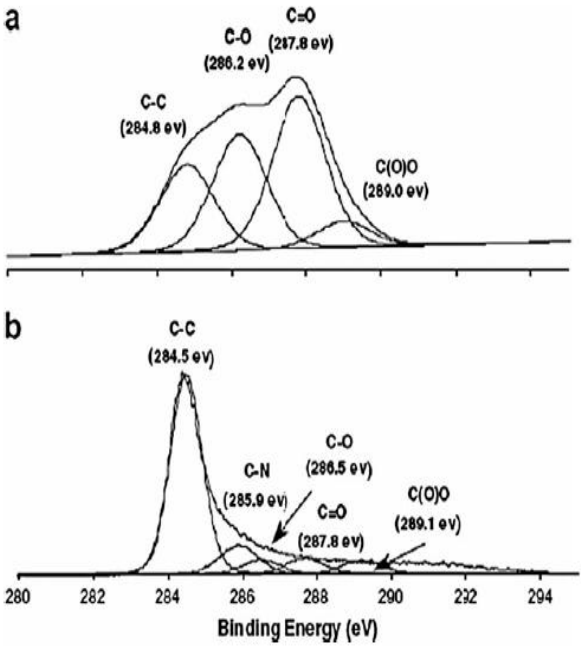

Fig. 1.10: The C-1s XPS spectra of: (a) graphene oxide, (b) hydrazine hydrate-reduced graphene oxide (taken from ref.[44] with permission from Elsevier).

It can be clearly seen that the carbonyl, epoxy, and carboxylic acid functional groups were enormously decreased in the reduced graphene oxide compared with the non-reduced one.[15]

The conductivity was also measured, the values were 2400±200 S m^{-1}, 2500±20 S m^{-1}, 0.021±0.002 S m^{-1} for the reduced, graphite, and graphite oxide respectively.[44] Since graphite oxide is an electrical insulator, its value was lower but the restoration of the π-system in the reduced graphene oxide moved the value closer to that of graphite.

1.8 Electronic Properties and Electrical Transport in Graphene

Graphene is composed of carbon atoms arranged in a hexagonal structure, which can be seen in Fig. 1.11. The structure has two basis atoms per unit cell as it is considered a triangular lattice. The lattice vectors can be written as:[11]

$$a_1 = \frac{a}{2}\left(3, \sqrt{3}\right), a_2 = \frac{a}{2}\left(3, -\sqrt{3}\right) \quad \textbf{(1.4)}$$

Where a ≈1.42 Å is the length of carbon-carbon bonds, intermediate between those of a single and double bonds with lengths r_1 ≈1.54 Å and r_2 ≈1.31 Å, respectively.

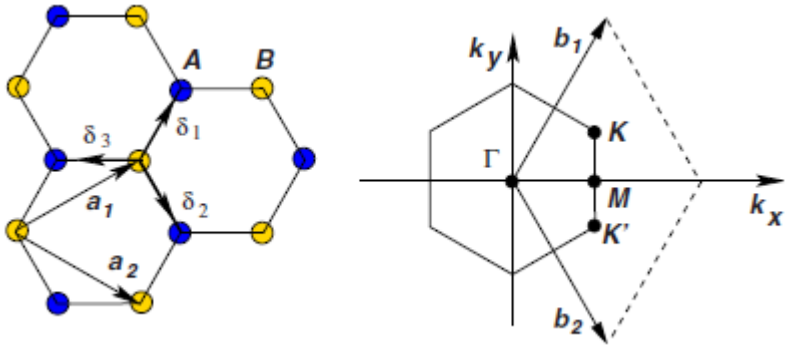

Fig. 1.11: (a) A honeycomb lattice, sublattices A and B are shown in blue and yellow color. (b) Reciprocal lattice vectors and some special points in the Brillouin zone (taken from ref.[58] with permission from American Physical Society).

Each atom is surrounded by three atoms from a different sublattice. The first Brillouin zone has two inequivalent points at the corners (named Dirac points). Their positions in momentum space are given by:[11]

$$\vec{\delta_1} = \frac{a}{2}\left(1, \sqrt{3}\right), \vec{\delta_2} = \frac{a}{2}\left(1, -\sqrt{3}\right), \vec{\delta_3} = a\left(-1, 0\right) \quad \textbf{(1.5)}$$

The reciprocal lattice vectors are given by:[11]

$$\vec{b_1} = \frac{2\pi}{3a}\left(1, \sqrt{3},\right), \vec{b_2} = \frac{2\pi}{3a}\left(1, -\sqrt{3}\right) \quad \textbf{(1.6)}$$

The wave vectors for the special high-symmetry points K, K', M are given by:[11]

$$\overrightarrow{K'}=\left(\frac{2\pi}{3a},\frac{2\pi}{3\sqrt{3a}}\right),\overrightarrow{K}=\left(\frac{2\pi}{3a},-\frac{2\pi}{3\sqrt{3a}}\right),\overrightarrow{M}=\left(\frac{2\pi}{3a},0\right) \quad \textbf{(1.7)}$$

The sp^2 hybridized states σ bonding and π bonding, the first form occupied and empty bands with a huge gap, whereas, the latter form a single band with a conical self-crossing point in K, K', and the unique electronic properties and the characteristic of extraordinary electronic structure is referred to this conical point. Wallace was the first one to get this conical point in 1947 in the idea of a simple tight-binding model. By following Wallace, there are no hopping processes within the sublattices in the nearest neighbour π bonding, hopping takes place only between A and B sublattices. The tight-binding Hamiltonian is represented by the 2*2 matrix:[11]

$$\hat{H}\left(\vec{k}\right)=\begin{pmatrix}0 & tS(\vec{k})\\ tS(\vec{k}) & 0\end{pmatrix} \quad \textbf{(1.8)}$$

Where $\vec{k}$ is the wave vector,

$$S\left(\vec{k}\right)=\sum_{\vec{\delta}}e^{i\vec{k}\vec{\delta}}=2\exp\left(\frac{ik_x a}{2}\right)\cos\left(\frac{k_y a\sqrt{3}}{2}\right)+\exp\left(-ik_x a\right) \quad \textbf{(1.9)}$$

Therefore, the energy is :

$$E\left(\vec{k}\right)=\pm t\left|S\left(\vec{k}\right)\right|=\pm t\sqrt{3+f\left(\vec{k}\right)} \quad \textbf{(1.10)}$$

Where

$$f\left(\vec{k}\right)=2\cos\left(\sqrt{3}k_y a\right)+4\cos\left(\frac{\sqrt{3}}{2}k_y a\right)\cos\left(\frac{3}{2}k_x a\right) \quad \textbf{(1.11)}$$

Band crossing occurs when:

$$S\left(\vec{k}\right)=S\left(\vec{k'}\right)=0 \quad \textbf{(1.12)}$$

The Hamiltonian near these points can be expanded as follows:[11]

$$\widehat{H}_{K'}\left(\vec{q}\right)\approx\frac{3at}{2}\begin{bmatrix}0 & \alpha(q_x+iq_y)\\ \alpha^*(q_x-iq_y) & 0\end{bmatrix}, \quad \textbf{(1.13)}$$

$$\widehat{H}_{K}\left(\vec{q}\right)\approx\frac{3at}{2}\begin{bmatrix}0 & \alpha^*(q_x-iq_y)\\ \alpha(q_x+iq_y) & 0\end{bmatrix} \quad \textbf{(1.14)}$$

Where $\alpha=e^{5i\pi/6}$, with $\vec{q}=\vec{k}-\vec{K}$ and $\vec{k}-\vec{K'}$, respectively. So, the effective Hamiltonian near the points K and K' take the form:

$$\widehat{H}_{K,K'}\left(\vec{q}\right)=\hbar v\begin{bmatrix}0 & q_x\mp iq_y\\ q_x\pm iq_y & 0\end{bmatrix}, \quad \textbf{(1.15)}$$

Where

$v=\frac{3a|t|}{2}$ the electron velocity at the conical points. By an additional phase shift by -π, the negative sign of t can be excluded.

By considering the next nearest neighbour hopping t':

$$E\left(\vec{k}\right)=\pm t\left|S\left(\vec{k}\right)\right|+t'f\left(\vec{k}\right)=\pm t\sqrt{3+f\left(\vec{k}\right)}+t'f\left(\vec{k}\right) \quad \textbf{(1.16)}$$

The electron-hole symmetry can be broken by the second term. The behaviour of the Hamiltonian near the conical points does not vary when shifting them from $E=0$ to $E=-3t'$. According to Reich et al. (2012), the first three hopping parameters are $t=-2.97eV$, $t'=-0.073eV$, and $t''=-0.33eV$. The smallest value is referred to the accurate and precise

electron hole symmetry of the spectrum throughout the whole Brillouin zone,[11] electronic dispersion in the honeycomb lattice is shown in Fig. 1.12:

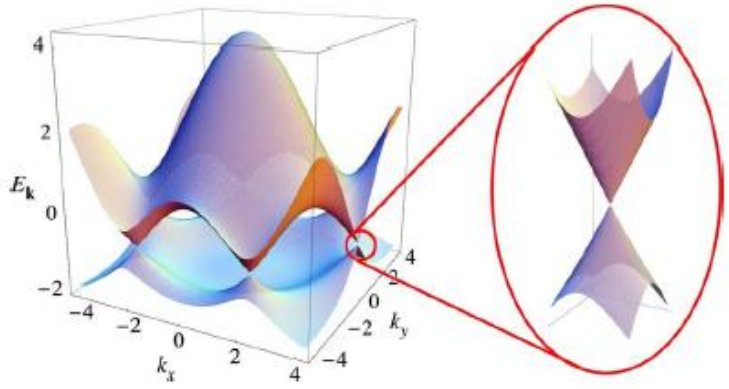

Fig. 1.12: Left, electronic dispersion in the honeycomb lattice. Right, expanded view of the energy bands close to one of the Dirac points (taken from ref.[58] with permission from American Physical Society).

Graphene is a zero gap semiconductor. The sp^2 hybridized carbon atoms are arranged in a hexagonal structure. An individual hexagonal ring consists of three strong sigma bonds in-plane which support the stable hexagonal structure, while Pz orbitals connect the graphene layers weakly. One of the most fascinating properties of graphene is the remarkable nature of its charge carriers, which act as massless relativistic particles (Dirac fermions). Near the Dirac points K and K', their electronic dispersion is similar to that of relativistic Dirac electrons. The valence and conduction bands overlap at the Dirac points, which makes graphene a zero band gap semiconductor.[9] A high quality of graphene leads to a high electrical conductivity, i.e. a low defect density in its crystal lattice. Generally, defects behave as scattering sites and prevent charge transport by limiting the electron mean free path.[9]

1.9 Diffusion Characteristics of Membranes

A membrane is a discrete, thin interface that moderates the permeation of chemical species in contact with it.[59] It can be homogeneous in terms of uniformity in composition and structure, or heterogeneous, in which case it contains holes and pores. The principal types of membranes are shown in Fig. 1.13:

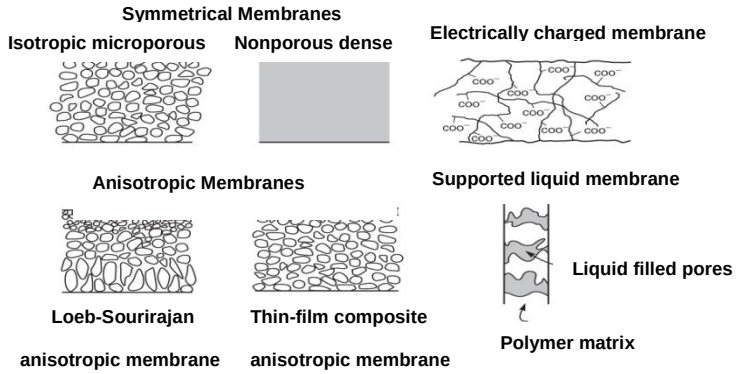

Fig. 1.13: Schematic diagrams of the principal structural types of membranes (adapted from ref.[59] with permission from Wiley).

Isotropic membranes have three types namely microporous, nonporous, and electrically charged. The first has pores in the order of 0.01–10 μm in diameter. The second does not have pores and the permeates are transported by diffusion under either pressure, concentration, or electrical potential gradient as a driving force. This type of membrane is useful for separation of species that are similar in size. The third one possesses positively or negatively charged ions. Anisotropic membranes are another type of membrane which could be ceramic, metal, or liquid. The thickness of the membrane plays a crucial role in the transport rate. The higher the thickness, the lower the transport rate, therefore, the membrane should be as thin as possible.[59] Anisotropic membranes comprise a very thin surface layer supported on a porous substructure, thicker than the thin surface layer. The permeation rate and the separation process are extremely dependent upon the surface layer. The nominal pore size and the corresponding theoretical model for the principal membrane separation processes is shown in Fig. 1.14. Membranes can be classified into three categories as shown in Fig. 1.14:[59]

1. Ultrafiltration, microfiltration, and microporous Knudsen diffusion gas separation membranes, all of which possess pores bigger than 10–15 Å in diameter, and in which the transport takes place via pore flow.

2. Non-porous membranes such as polymeric gas separation, pervaporation, and reverse osmosis ones have a dense selective polymer layer with no visible pores. Molecules in the range of 2–5 Å can exhibit transport through these membranes. Since there are no pores in these membranes, the flux of permeates are lower than those in microporous membranes. The solution-diffusion model best describes the transport through these membranes. 5–10 Å in diameter is the spacing between polymer chains which represent the free volume elements in these membranes.

3. Intermediate membranes possess pores between 5–15 Å in diameter. For example, nanofiltration membranes, some gas separation membranes, and some finely porous ceramic membranes fall into this class of membranes. If the polymers are made of stiff polymer chain in the gas separation membranes then these polymers are called polymers with intrinsic microporosity (PIM). The transport through these membranes is either via the pore flow model or the solution-diffusion model, depending on the pore size of these membranes.

1.10 Transport Theory in Membranes

The most significant characteristic of membranes is their capability to control the rate of permeation of various species. The mechanism of permeation can be divided into two models.[59] The first one is the so-called the pore-flow model, in which components are transported from one phase to another via pressure-driven force through pores. One component is filtered through the pores in the membrane based on size, and separation takes place. The second one is the solution-diffusion model, in which components species dissolve in the membrane then diffuse through it according to concentration gradients. The separation takes place due to the

difference in the solubility as well as the rate of diffusivity. Generally, the species transports through a membrane as a result of a driving force on the components in the feed part.

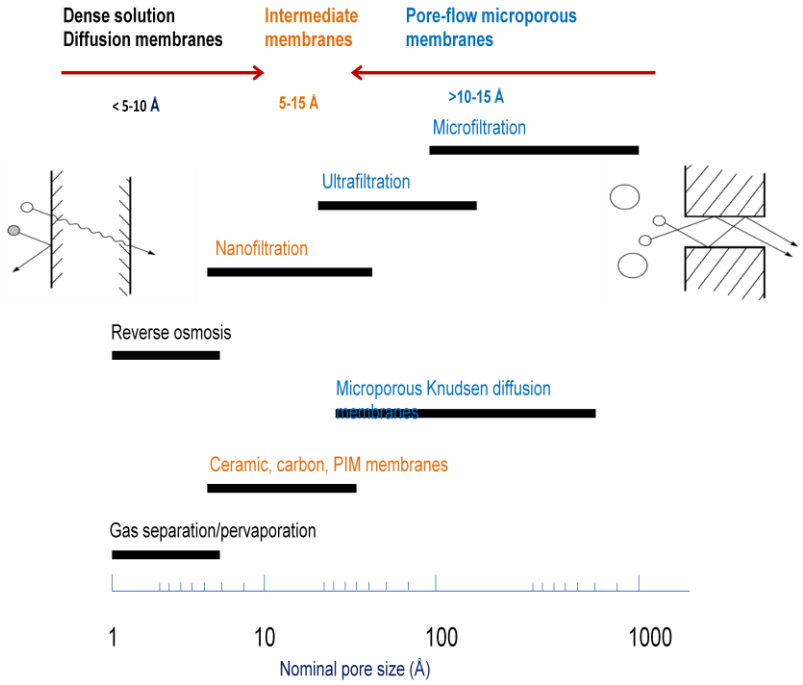

Fig. 1.14: The nominal pore size and the best theoretical model for the principal membrane separation processes (adapted from ref.[59] with permission from Wiley).

Diffusion was first studied by Fick in 1855.[59] He stated an equation called Fick`s first law of diffusion:[59]

$$J_i = -D_i \frac{dC_i}{dx} \qquad \textbf{(1.17)}$$

Where J_i is the rate of transfer of component i or flux (g/cm^2.s), $\frac{dC_i}{dx}$ is the concentration gradient of component i (g/cm^3.cm), and D_i is the diffusion coefficient (cm^2.s). The direction of diffusion is down the concentration gradient, hence the minus sign appears in the equation. The basis of the solution-diffusion model is the diffusion, whereas, pressure-driven force is the basis of the pore-flow model, and Darcy`s law is the basic equation for pore-flow model. It can be written as:[59]

$$J_i = K\, c_i^{'}\, \frac{dp}{dx} \qquad \textbf{(1.18)}$$

Where $\frac{dp}{dx}$ is the pressure gradient, c_i is the concentration of component i , and K is a coefficient reflecting the nature of the medium.

1.11 Diffusion in Graphene Membranes

As was mentioned earlier, two mechanisms can describe the permeation through membranes, either the pore flow mechanism or the solution-diffusion mechanism. The state of the art in membrane permeation relies on the latter one. Polymeric membranes can provide a great salt rejection; however, the diffusive transport of water through them is slow. To tackle this matter, researchers have focused on increasing water transport by molecular sieving in nanostructured membranes such as carbon nanotubes and zeolites.[60] Cohen-Tanugi and Grossman at the Massachusetts Institute of Technology (MIT) claimed that nanoporous graphene membranes can separate salts from water.[60] Since the membrane`s thickness is inversely proportional with flux, graphene, which is the thinnest possible membrane, and has high mechanical strength, and low pressure requirements, is promising for increasing water permeability, as can be seen in Fig. 1.15. They have claimed that nanoporous graphene membranes have better performance than polymeric reverse osmosis membranes in terms of water permeability by two to three orders of magnitude.[60] Nanotubes and zeolites membranes have low performance due to the difficulty to be produced in a scalable fashion. Moreover, the smallest carbon nanotubes used for membranes are too large to preclude salt ions and it is more of a challenge to fabricate thin and continuous zeolite layers.[60]

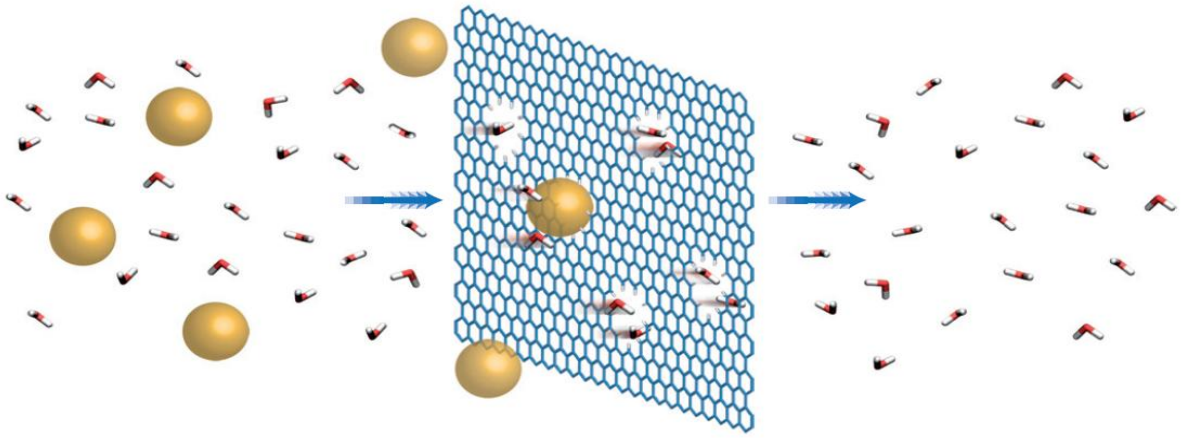

Fig. 1.15: Nanoporous graphene membranes. High pressure applied to the salt water (left) drives water molecules (red and white) across the graphene membrane (right), while salt ions (spheres) are blocked. Chemical functionalization of the pores with hydrogen (white) increases water selectively, whereas functionalization with hydroxyl groups (not shown) increases the speed of water transport (taken from ref.[60] with permission from Nature Publishing Group).

Studies have been conducted on the transport of gas molecules and ions through nanoporous graphene membranes.[56,61] Cohen-Tanugi and Grossman anticipate water transport up to 66 L per cm^2· day·MPa in nanoporous graphene membranes compared to typical reverse osmosis membranes, which provide water transport of ~ 0.01–0.05 L per cm^2·day·MPa. The fast rate of water passage was attributed to the thickness of the graphene membrane.[60] The type of the functionalization of the pores in graphene membranes plays a crucial role in the efficiency of salt ion rejection. For instance, there is greater efficiency when pores are chemically functionalized with hydrogen than with hydroxyl groups; however, the disadvantage of this is a lower flow rates because the water molecules require a particular orientation before they pass through a hydrogenated pore. The researchers also discovered that the water in the hydration shell of salt ions can be substituted by the hydroxyl groups which allows some ions to flow through, and consequently reducing the salt rejection ratio. Researchers also find that at higher pressure, graphene membranes lose the ability to repel salt ions. For a maximum water throughput,

Cohen-Tanugi and Grossman determined the ideal size for hydrogenated pores and hydroxylated pores to be 23.1 $Å^2$ and 16.3 $Å^2$, respectively. This determination was based on simulations.[62] Nanopores can be introduced into the structure of graphene by electron beam exposure, helium ion beam drilling, and chemical etching to achieve more accurate pore size distribution and higher porosity.[63,64,65,66] Hydrogenated and hydroxylated graphene pores are shown in Fig. 1.16.

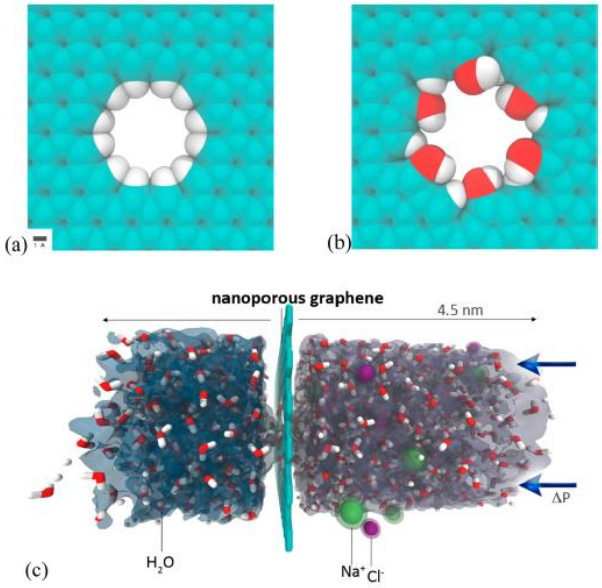

Fig. 1.16: (a) Hydrogenated, (b) hydroxylated graphene pores, and (c) side view of the pore as constructed from simulations (taken from ref.[67] with permission from American Chemical Society).

The existence of oxygen-containing functional groups on both sides of the GO sheets leads to a large inter-layer distance and vacant spaces between non-oxidized regions, which results in the formation of a network of nanocapillaries between the GO layers, and this facilitates water permeation through these nanocapillaries.[68] Nair et al, report fast permeation of water through GO membranes that are basically impermeable to other liquids and to helium.[69] Nair et al, have also found that the permeability of water is 100 times less with thermally reduced GO at 250 $^{\circ}C$ comparing with non-reduced GO membrane, and claimed that the change in the structure (i.e.

decreasing in d spacing from ≈ 10 to 4 Å) had led to the fast transport of water vapor through GO film.[68] Possible permeation through laminates is shown in Fig. 1.17:

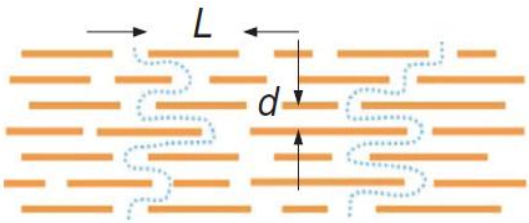

Fig. 1.17: Schematic view of possible permeation through GO laminates, L, crystal size, d, spacing between layers (taken from ref.[68] with permission from The American Association for the advancement of Science).

In 2008, Michael D. Fischbein et al. punched nanopores in graphene and claimed that porous graphene is stable.[70] K. Sint et al. show that by designing functionalized nanopores in graphene, the membranes could be utilized as ionic sieves of high selectively.[56] Fig. 1.18 shows chemically modified graphene nanopores. The passage of cations would prefer negatively charged functionalized nanopores, and the passage of anions would prefer positively charged nanopores. These nanopores could be formed in the graphene monolayers by ion etching.[71]

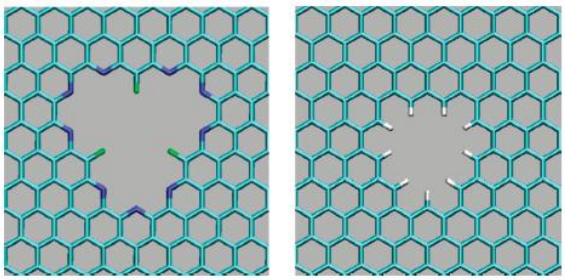

Fig. 1.18: Functionalized graphene nanopores. The functionalized nanopore (left) is terminated by negatively charged nitrogen and flourines. The H-pore (right) is terminated by positively charged hydrogen (taken from ref.[56] with permission from American Chemical Society).

J. Schrier proposed that porous graphene can separate helium from other noble gases.[72] De-en Jiang et al. separated H_2 and CH_4 by using the porous graphene.[73] Yuliang Zhao et al. used different pore sizes and shapes of porous graphene for H_2 and N_2 separation, and claimed that by adjusting the pore size and shape, both selectivity and permeability could be controlled.[74] It has been reported that a single layer graphene film is impermeable to gases and liquids in which two different phases can be separated.[75] Karan et al. have reported ultrafast permeation of organic solvents through diamond-like carbon (DLC) nanosheets that reject solute molecules larger than 1 nm as shown in Fig. 1.19.

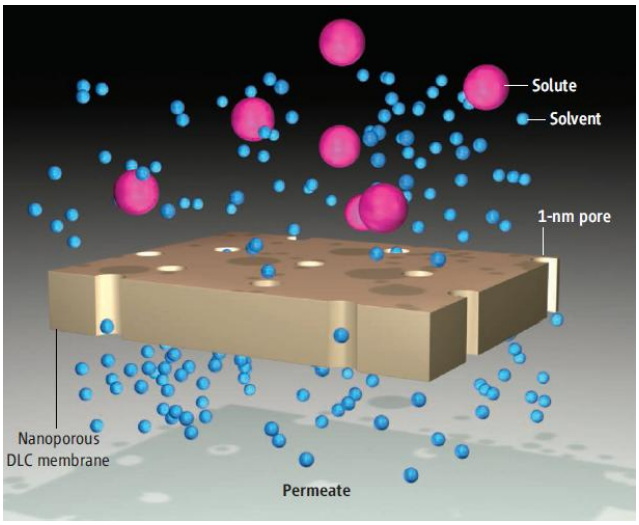

Fig. 1.19: Solvent molecules permeate through the nanopores of diamond-like carbon (DLC) membranes (taken from ref.[69] with permission from The American Association for the Advancement of Science).

According to the results of molecular dynamics simulations, graphene with nanopores can be exploited to separate NaCl from water useful for applications such as desalination and water purification.[55] Hongwei Zhu et al. have claimed that sodium salts had rapid permeation through GO membranes compared to heavy metal salts. A schematic diagram of the permeation processes of different ions through GO membranes is shown in Fig. 1.20:

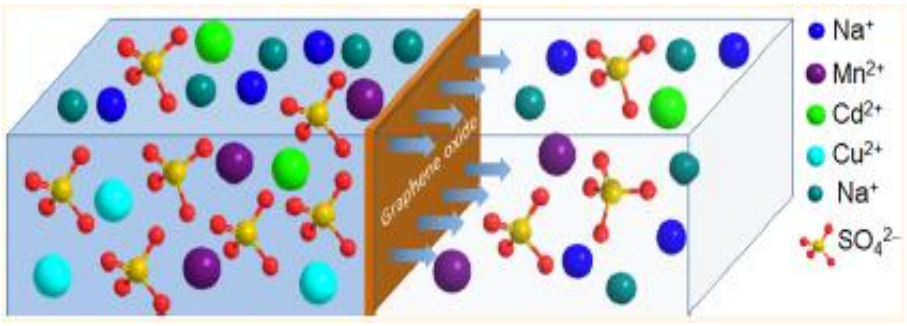

Fig. 1.20: Schematic diagram of the permeation processes of different ions through GO membranes (taken from ref.[55] with permission from American Chemical Society).

The selective permeation properties of the GO membranes rely on the nanocapillaries that formed within the structure of the GO membrane and the interaction between the oxygen functional groups and the metal ions as shown in Fig. 1.21.[55]

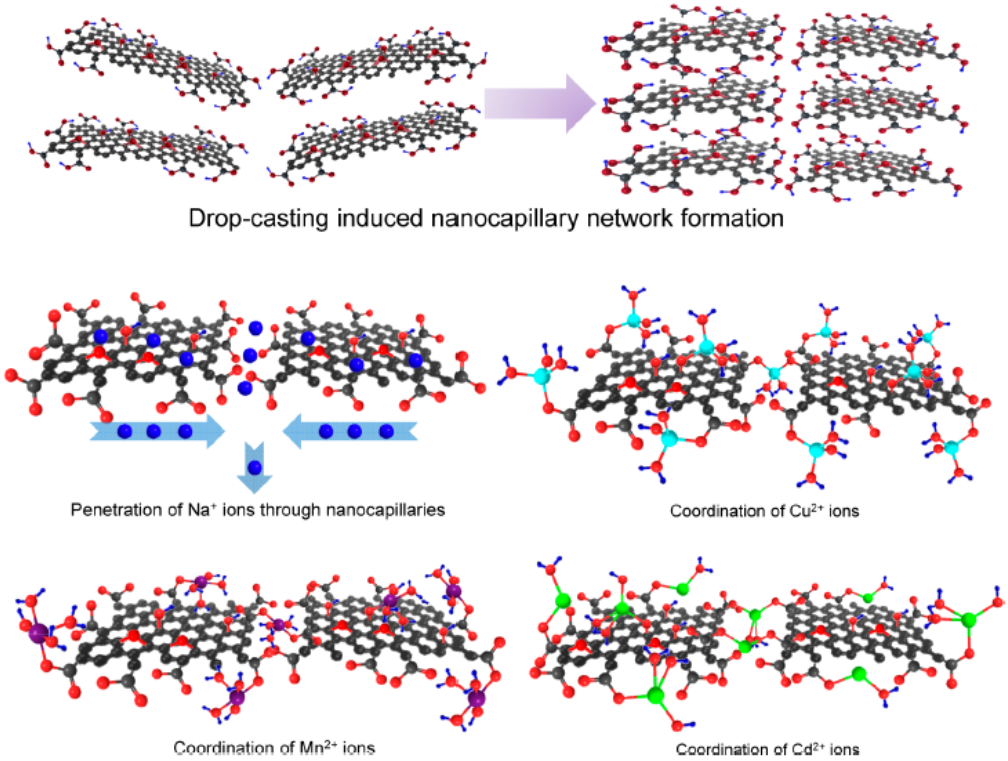

Fig. 1.21: Schematic diagrams of the GO membrane and the interaction with different ions (taken from ref.[55] with permission from American Chemical Society).

1.12 Electrical Conduction Mechanism in Graphene Oxide and Reduced GO Films

It has been proved that chemically derived graphene demonstrates an electrical conductivity on the order of a few Siemens per centimeter (roughly pristine graphene layers are three orders of magnitude higher than chemically derived graphene),[76] which is helpful for many applications such as photovoltaic or composite materials. It has been reported that residual defects exist in GO-derived graphene,[76] and the real question is how does charge transport occur in such inhomogeneous system? Charge transport occurs through the mechanisms of hopping conduction, and tunneling. Hopping is an incoherent thermally activated process in which electrons move from one position to another. The probability of hopping is an exponential in the height only of the free energy barrier between sites. The charge transport mechanism can be interpreted by either the hopping model at room temperature or the tunneling model at high electric field. The first one is given by the following equation:[76]

$$G = Y_{\circ} + G_{\circ}\, exp\,(\frac{V}{aL}) \qquad \textbf{(1.19)}$$

Where V is the applied bias, and L is the distance between the electrodes on the GO membrane in which I-V measurements are conducted.[76]

$$a = \frac{kT}{0.18er} \qquad \textbf{(1.20)}$$

Where k is the Boltzmann`s constant, T is temperature of the measurement, e is the absolute charge on electron, and r is the hopping distance. $G_{\circ}$ is the hopping parameter which depends on, N, the density of states $N(E_F)$ near the Fermi level, and L, the localization length of the electronic wave function.[76]

$$G_{\circ} = G_1 \exp\,(-\frac{B}{T^{1/3}})\ ;\ B = (\frac{3}{kN(E_F)L_l^2})^{1/3} \qquad \textbf{(1.21)}$$

The in-plane conductivity of the GO and reduced GO membranes were measured over the scale of a few millimeters in our experiments at applied bias that was limited to 20 V. Hence being in the low electric field regime the hopping model is used to fit the results from in-plane conduction measurement of these membranes.

The tunneling model becomes relevant for the out-of-plane conduction of these membranes. In this case the conduction of charge carriers which occurs over a thickness of a few microns (the thickness of the membrane) with an applied bias was limited to 20 V. Hence with field strengths in the range of 10^7 V/m, tunneling becomes the relevant conduction phenomena. Further, the sheets in the membrane will also have direct contact point with each other; therefore, a second ohmic conductivity term is also included.

The combined model is given by the equation:[77]

$$I = \frac{V}{R} + P_1 \times V^2 \times exp\left(-\frac{aE_c}{V}\right) \quad \textbf{(1.22)}$$

The first term is the ohmic resistance due to direct contact between the sheets; the second term is due to tunneling. Here E_c is the critical field for tunneling, a the length scale for the tunneling (this is considering that the term V/a is the effective electric field in the membrane), and R is the ohmic resistance of the film.

Chapter 2. Background of Instruments and Techniques

2.1 Overview of The Techniques

A significant challenge was faced in characterizing the synthesized films. In our experiments, this was primarily achieved by using X-ray diffraction (XRD), scanning Electron Microscopy (SEM), multiple spectroscopic techniques, such as Fourier Transform Infrared (FT-IR), Raman Spectroscopy, Ultraviolet Visible Spectroscopy (UV-Vis), X-ray Photoelectron Spectroscopy (XPS), and Thermal Gravimetric Analysis (TGA).

X-ray Diffraction (XRD) was used to characterize the change in the inter-layer spacing between the graphene sheets in these films. Scanning Electron Microscopy (SEM) was used to produce images in order to investigate the morphology of the films as well as to explore cross-sections within the layers of the films on selected spots in the film. Fourier Transform Infrared (FT-IR) was used to detect oxygen-containing functional groups within the films as well as to confirm that these groups have been removed through either thermal or chemical reductions. Raman Spectroscopy was also used to investigate the electronic structure of the films and characterize the extent of reduction of the films by comparing the intensity between the D band and the G band for the non-reduced film with those of various reduced films. Ultraviolet-Visible Spectroscopy (UV-VIS) was used to assess the restoration of aromaticity to form graphene films as well as to confirm chemical reduction of graphene oxide films. Thermal Gravimetric Analysis (TGA) was used to verify thermal stability of these films. X-ray Photoelectron Spectroscopy (XPS) was also used to determine the C/O ratio of the non-reduced and reduced films as an indication of the removal of oxygen-containing functional groups from the surface of graphene oxide (GO) films.

2.2 Principles of Powder X-ray Diffraction

X- rays were discovered by the German Physicist Wilhelm Röentgen in 1895, for which he was awarded the Nobel Prize in 1901.[78] X-ray diffraction was first discovered by Max von Laue when he observed the first X-ray diffraction pattern from copper sulfate crystals in 1912. A year after, William Lawrence Bragg and his father William Henry Bragg discovered the Bragg`s Law equation (1).[78]

X-rays are electromagnetic radiation of wavelength between 0.1 and 100 Å, which lie between Gamma rays and Ultraviolet radiation, and are in the region of short interatomic bonds. X-rays are usually generated by accelerating high-energy particles, e.g. electrons through 30,000 V, and these are made to strike target matter. Two constituents can be seen in the resulting X-ray spectra, white radiation, which is a wide spectrum of wavelengths and a number of fixed, or monochromatic wavelengths Fig. 2.1:

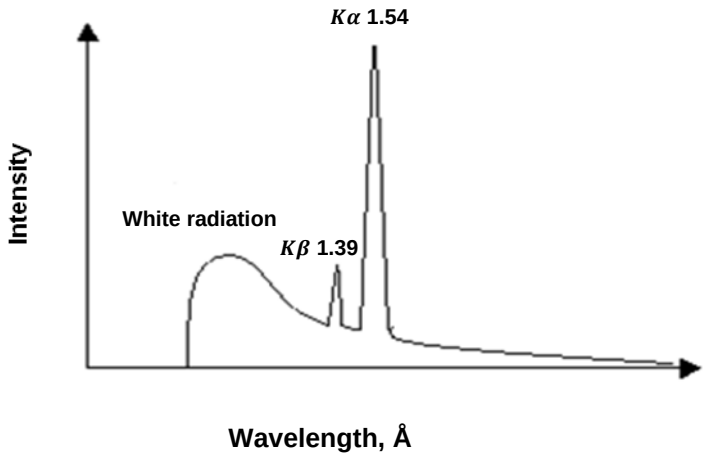

Fig. 2.1: Characteristic X-ray emission spectrum from elemental copper.[79]

When the electrons collide with matter, the electrons either are stopped or slowed down and some of their lost energy is transformed into electromagnetic radiation. This causes white radiation.[80] The greatest energy of x-ray takes place when all the kinetic energy of the incident

particles is transformed into X-rays. The high acceleration, 30 kV, of a beam of electrons permits them to collide with a metal target, often Cu. The adequate energy of the incident electrons is able to ionize some of the Cu 1s (K shell) electrons, An electron in an outer orbital (2p or 3p) instantly fall down to occupy the vacant 1s level and the energy of the transition is emitted as X-rays. Every transition is associated with fixed energy values thus an X-ray spectrum can be used as a fingerprint for different elements. For instance, Cu has two types of transitions, which are:

$2p \rightarrow 1s$ Called Kα (1.5418 Å) **(2.1)**

$3p \rightarrow 1s$ Called Kβ (1.3922 Å) **(2.2)**

Actually, the Kα transition has two peaks, $K\alpha_1$=1.54051 Å and $K\alpha_2$=1.54433 Å, because of the slightly different energy of the transition for the two possible spin states of the 2p electron which makes the transition, related to the spin of the vacant 1s orbital. Kα wavelengths of the target metal is frequently used for X-ray generation.[80] A diffraction pattern is generally produced by the scattering of X-rays from the atoms arranged in a periodic array. Some materials such as glass do not generate discrete diffraction patterns, because their structure does not possess a periodic array with long range order. The silicon and oxygen atoms of silicon dioxide (SiO_2) can be arranged in different fashions generating three different forms of SiO_2, namely, Glass, Quartz, and Cristobalite. Thus, different arrangements for the atoms leads to different diffraction patterns.

Bragg`s Law:[78] $2d_{hkl}\sin\theta_{hkl} = n\lambda$ **(2.3)**

Where d_{hkl} is the d-spacing between crystal planes hkl (Miller indices) in a crystal, θ_{hkl} is the angle of the incidence (Bragg angle), n is an integer value, λ is the wavelength of the beam.

This equation is known as Bragg`s Law (or Bragg equation), which correlates the Bragg angle (θ_{hkl}) to the spacing between the crystal planes (d_{hkl}). X-ray diffraction is shown in Fig. 2.2. Diffraction peaks are associated with planes of atoms in the crystal. During X-ray experiments, each atom within the crystal is irradiated with X-rays and the interaction between the incoming X-ray beam and the oscillating electrons within each atom produces diffraction in all directions. The scattered X-ray beams from all Miller indices provide different spots. These diffraction spots represent the diffraction pattern of the crystal.[81]

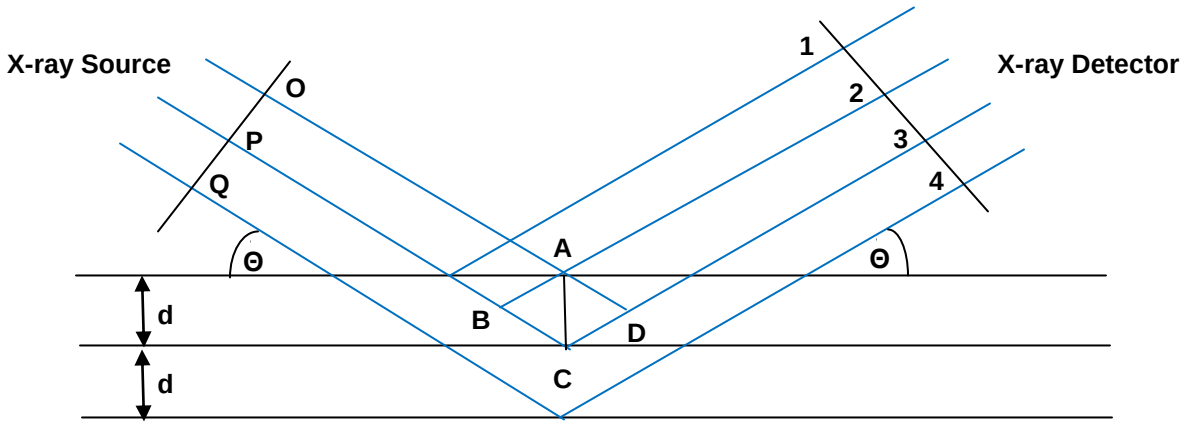

Fig. 2.2: Schematic of X-ray diffraction.[81]

The scattering factor (or form factor) is the scattering amplitude of X-rays of an atom. It is donated by the symbol (f_0). The more electrons that an atom possesses, the more strongly it will scatter incoming X-rays. As the Bragg angle increases, the scattering power is reduced.[82] The structure factor (F_{hkl}) is the sum of the atomic scattering of each atom within the crystal. It is correlated to Miller indices and atomic position (xyz) as shown in the following equation:[82]

$$F_{hkl} = \sum_j f_j e^{2\pi i(hx_j + kyj + lz_j)} \qquad \textbf{(2.4)}$$

Where f_j is the scattering factor of the j atom, and (x_j, y_j, z_j) are fractional coordinates of the scattering factor. The intensity of a reflection is proportional to the square of the structure factor as it appears in the following equation:[82]

$$I_{hkl} \propto F_{hkl}^2 \quad \textbf{(2.5)}$$

Then, the magnitude of the structure factor can be calculated:

$$|F_{hkl}| \propto \sqrt{I_{hkl}} \quad \textbf{(2.6)}$$

Either a powder or single crystal X-ray diffractometer can be used to measure the intensity of the hkl reflection (I_{hkl}) that is recorded by the detector. Powder X-ray is frequently used to identify unknown substances by matching diffraction data to known substances in databases such as the Inorganic Crystal Structure Database (ICSD) or the International Centre for Diffraction Data (ICDD). All X-ray diffraction patterns presented in this thesis were obtained from a Bruker D8 Advance powder X-ray diffractometer equipped with a Våntec-1 detector operating at 40 kV and 30 mA.

2.3 Background of Scanning Electron Microscopy

Scanning electron microscopy (SEM) is a powerful tool for the examination and analysis of the microstructure morphology of materials and for chemical composition characterization. It was invented soon after the transmission electron microscope (TEM) in the 1930s by Knoll and von Ardenne, in Germany. In 1963, the first commercial SEM was accessible at Cambridge University, England,[83] SEM is based on the ejection of secondary electrons due to the collision of incident electrons (low energy). A diversity of signals at the surface of the solid is being generated by using a focused beam of high energy electrons. These signals result from the interaction between the electrons and the sample which displays information about the

morphology of the sample, crystalline structure, chemical composition, and orientation of the materials. When the incident (primary) electrons strike the electrons present in a solid, secondary electrons are released. It is too difficult to focus these electrons into an image by electron lenses so the principle of scanning is employed. A small diameter electron probe is scanned across the surface of the sample, changing the beam direction under the influence of either electrostatic or magnetic fields by scanning coincidently in two perpendicular directions, a two-dimensional image of an area of the solid can be covered as a square or rectangular area in which secondary electrons from a selected area on the solid is being collected.[84] SEM basically consists of an electron beam generating and accelerating system (electron gun), a high vacuum system, a focusing, scanning system, a specimen stage, an electron detecting, multiplying system, amplifiers, cathode ray tubes for visual observation and photograph.[83] By using the conventional SEM techniques, area from 1 cm to 5 microns in width can be imaged. The SEM commonly comes with Energy Dispersive X-ray analysis (EDX), which is beneficial for chemical composition determination. The image brightness results from characteristics of the solid as a consequence of the response towards an electron bombardment. The accelerated electrons interact with the sample and signals are generated as a result. These signals comprise different types of emission such as secondary electrons(atomic electrons emitted from the sample as a consequence of inelastic scattering), which involves an angle less than 90°, backscattered electrons(incoming electrons scattered elastically through an angle greater than angle of 90°), photons as X-rays, and heat. Secondary electrons reflect the morphology of the sample. X-rays are used for elemental analysis. SEM analysis is regarded as a non-destructive that is X-rays produced by electron interactions do not induce volume loss of the sample, so it is feasible to analyze the sample materials repeatedly. Zeiss FESEM 1530 was used for FESEM analysis of all samples in this thesis.

2.4 Introduction of Fourier Transform Infrared Spectroscopy

Fourier Transform infrared spectroscopy (FT-IR) was developed in 1880 by Albert Abraham Michelson. In 1907, he became the first American to be awarded the Nobel Prize in Physics.[85] By using the Michelson interferometer, the wavelengths of light can be measured precisely. Michelson had to struggle in using his interferometer to obtain spectra manually. He had to carry out some calculations to convert interferometer data into a spectrum. The creation of computers made the calculation of Fourier transforms faster. J.W. Cooley and J.W. Tukey then at Bell labs, discovered the Fast Fourier Transform (FFT), or Cooley Tukey Algorithm. Using this algorithm facilitated the calculation of Fourier transforms on a computer, and is still the basis for the transformation routines used in commercial FT-IR spectrophotometers, the first of which were produced commercially by the Digilab subsidiary of Block Engineering in Cambridge Massachusetts in the late 1960s.[85]

FT-IR spectroscopy can be combined with other techniques such as Gas Chromatography (GC) so that it can be used for analyzing complex mixtures rapidly and precisely. A portable FT-IR instrument can be also used to measure, for example, the levels of pollutants coming out of an automobile. FT-IR can be connected to a High Pressure Liquid Chromatograph (HPLC) to obtain infrared spectra for biological samples. In medicine, the differences between the infrared spectra of healthy and cancerous human colon cells can be used to determine the biochemical differences between healthy and malignant cells.[85] In general, infrared spectroscopy is a great tool for determining functional groups, however, the technique itself cannot be used to explain the complete structure of unknown molecules. The usual approach to this puzzle is to use FT-IR in conjunction with other molecular spectroscopy techniques such as NMR, UV-Vis spectroscopy, Raman scattering, and mass spectrometry. All of these techniques supply information about a structure used to identify unknown molecules. How does FT-IR work? The object of an interferometer is to get a beam of light, split it into two beams, and make one of

them travel a different distance from the other. The Michelson interferometer comprises four arms. The first one includes a source of infrared light, the second one contains a fixed mirror, the third includes a moving mirror, and the fourth one is open. A beam splitter, where the fourth arm meets, is designed to transfer half of the radiation, and to reflect the other half of it. As a consequence, the light transferred by the beam splitter hits the fixed mirror, and the light reflected by the beam splitter hits the moving mirror. After reflection from the mirrors, the two light beams align at the beam splitter, then leave the interferometer to interact with the sample and hit the detector. A Michelson interferometer is shown in Fig. 2.3.

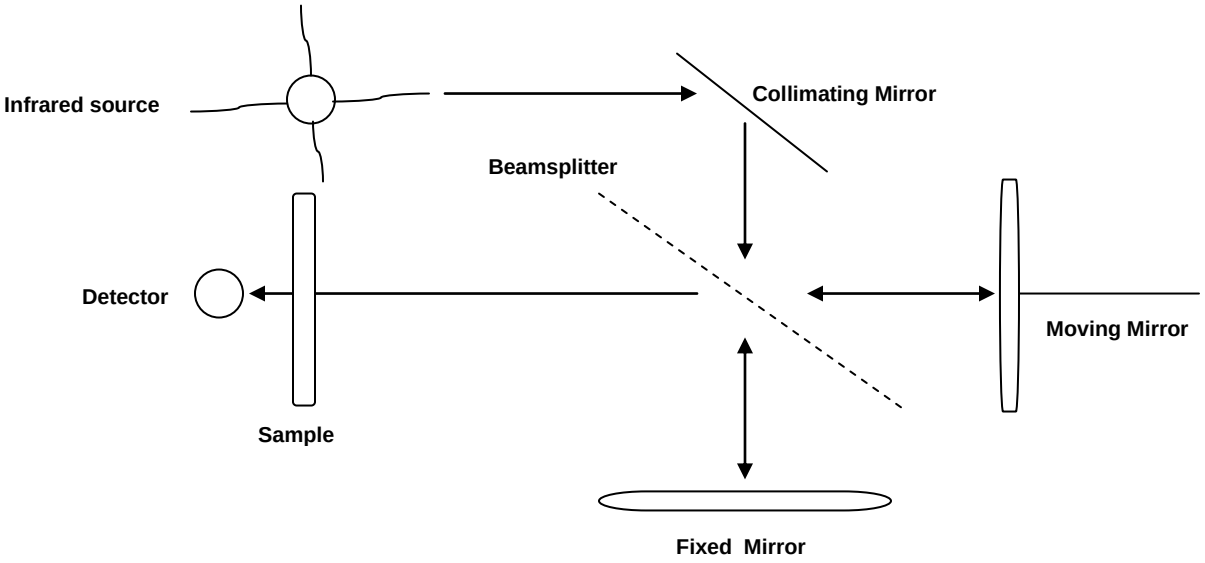

Fig. 2.3: Schematic diagram of the Michelson interferometer.[85]

FT-IR measures light intensity versus a property of light. The absorbance spectrum can be calculated from the following equation:[86]

$$A = \log(I_o / I) \qquad \textbf{(2.7)}$$

Where A is absorbance, I_o is intensity in the background spectrum, and I is intensity in the sample spectrum.

Beer`s Law shows the relationship between the absorbance and the concentration of the sample molecules as it follows:[85]

$$A = \varepsilon l C \quad \textbf{(2.8)}$$

Where A is absorbance, ε is Absorptivity, l is pathlength, and C is concentration. Beer`s law can be utilized to determine the concentration of molecules in samples. An FT-IR spectrum can be plotted as percent transmittance ($\%T$) in the y-axis, which measures the percentage of light transmitted by a sample. $\%T$ can be calculated via the following equation:[86]

$$\%T = (I / I_o) * 100 \quad \textbf{(2.9)}$$

Where $\%T$ is percent transmittance, I is intensity in the sample spectrum, I_o is intensity in the background spectrum. The peak positions in the spectrum correlate with molecular structure and can be used for identification of molecules in unknown sample.[85] All the measurements of the samples were performed using Bruker Tensor 27 FT-IR spectrometer.

2.5 Principles of Raman Spectroscopy

Raman spectroscopy detects the vibrational motions of a molecule similar to infrared spectroscopy. However, in Raman spectroscopy light scattering is being measured, while infrared spectroscopy is based on absorption of photons. Generally, when electromagnetic radiation irradiates a molecule, the energy might be absorbed, transmitted, or scattered.[87] In 1928, Chandrasekhara Venkata Raman discovered a new type of secondary radiation known as the Raman effect.[88] In 1930, C.V Raman was awarded the Nobel Prize in Physics for this discovery.[89] Raman spectroscopy became the principal means of non-destructive chemical analysis. In a Raman spectrometer, the sample is irradiated with a source of monochromatic radiation in the visible part of the spectrum. This radiation should be lower than the electronic

frequencies and higher than the vibrational frequencies. Interaction of incident radiation with the sample results in scattering which is detected by the spectrophotometer.[87] Raman spectroscopy probes the vibrational levels, and its signal is observed as inelastically scattered light. As a consequence, the vibrational energy of the molecule is altered by irradiation. Rayleigh, which is another type of scattering, can be considered as an elastic collision between the incident photon and the molecule in which the vibrational energy levels are unchanged, consequently, the energy and the frequency of the scattered photon is the same as that of the incident photon.[87] Raman scattering can be visualized by a quantum energy diagram Fig. 2.4:

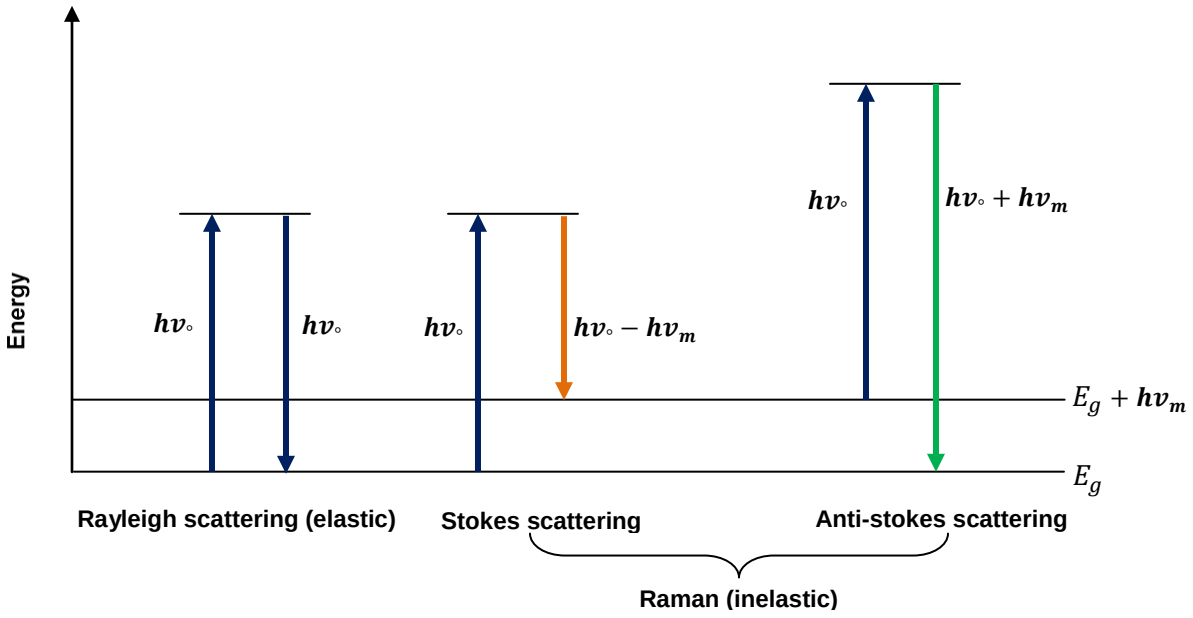

Fig. 2.4: Rayleigh and Raman Scattering.[87]

It can be seen that there are three types of scattering: Rayleigh, Stokes, Anti-stokes scattering. In Rayleigh scattering, the incident light strike a molecule, causing an electron in a ground vibrational energy level to move to an excited state after which it relaxes and returns back to the

same vibrational energy level from which it began. This is represented by ν_o in which there is no change in the frequency or energy, known as an elastic scattering. In Stokes scattering, the electron starts from the ground energy level and it is moved to the excited state then relaxes to an energy level that is higher than the starting level of the electron. In Anti-Stokes scattering, an electron starts in a vibrational energy level that is higher in energy than the ground vibrational level, is moved to an excited state then relaxes back to a ground vibrational level which has a lower energy than the initial level. Anti-stokes is represented by + ν_m, of the other two. Stokes is more frequently used for most Raman spectroscopy because at room temperature, most of the molecules exist in the ground vibrational level, consequently, Stokes lines are greater in intensities than anti-Stokes which are generated from an excited level which have a lower population.[87] Raman spectroscopy has the advantages of being non-destructive too, and requiring very little of the sample; furthermore it requires no special preparation. It can be utilized in both qualitative and quantitative analysis. Polarizability can be considered as distortion of the electron cloud of the molecule by an electric field. The molecular vibration has to be accompanied by a change in the polarizability of the molecule in order to be Raman active.[87]

$$\mu = \propto E \qquad \textbf{(2.10)}$$

Where μ the incident dipole moment, E the strength of the electric field, $\propto$ the polarizability. Molecules with isotropic polarizability are non-active in Raman spectroscopy; those with anisotropic polarizability are active in Raman spectroscopy.

The intensity of the scattered light is inversely proportional to the fourth power of the wavelength of the incident light.[89] Therefore, it is significant to consider the excitation wavelengths when carrying out Raman measurements. Since Raman spectroscopy is targeting the chemical bonds, it is used for structure identification and the determination of the properties of organic

and inorganic compounds. Raman also provides structural information in which of each spectrum of the observed bands is related to a specific vibrational energies levels. Most important is that each of the bands will always be in the same position regardless of the excitation wavelength being used.[89] Raman also can be used to track changes in frequency shift. For instance, diamond and graphite are allotropes for carbon, and different in the structure and symmetry. As a consequence, the physical and chemical properties would be different. Their Raman peaks are 1332 cm^{-1} and 1580 cm^{-1} respectively.[89] All the samples measurements were performed using Raman microscope Bruker Senterra.

2.6 Background of Ultraviolet Spectroscopy

Ultraviolet Spectroscopy (UV) has been available since 1943.[80] Many species in a solution can absorb ultraviolet (UV) and visible radiation and provides quantitative analysis.[90] It is based on Beer`s Law which states the absorption is directly proportional to the path length, L, and the concentration, C, of the absorbing species as follows:[90]

$$A = \varepsilon LC \qquad \textbf{(2.11)}$$

where ε is a constant of proportionality, called absorptivity. Various molecules absorb radiation of different wavelengths. A number of absorption bands will appear in the absorption spectrum corresponding to structural groups within the molecule. For instance, the carbonyl groups has a unique wavelength absorption in the UV region regardless of the compound. The rules of the measurements are: 1- absorbing species in a solution. 2- Selection of an appropriate wavelength in order to gain accurate measurements from the absorbing species. 3- Comparing the ratio of the intensity of the radiation which passes through a fixed thickness of the absorbing solution (Cuvette of known path length) with the intensity of the corresponding radiation beam when it passes through an appropriate blank solution. The percent transmittance, $\%T$, can be calculated by the following equation:[90]

$$\%T = 100 * \left(I / I_o \right) \qquad \textbf{(2.12)}$$

Where I is the intensity transmitted by the sample, and I_o is the intensity by the reference solution known as transmittance. The transmittance can be converted into absorbance by using the following equation:[90]

$$A = \log(I_o / I) \qquad \textbf{(2.13)}$$

here A is the absorbance. Three types of electronic transitions can be considered in the absorption of UV radiation as shown in Fig. 2.5. 1- Transitions involving σ, π, and n electrons. 2- Transitions involving charge transfer electrons. 3- Transitions involving d and f electrons. Electrons in a molecule can be transferred from their ground state to an excited state upon absorbing energy. These vibrations and rotations have distinct energy levels as can be seen in Fig. 2.6:

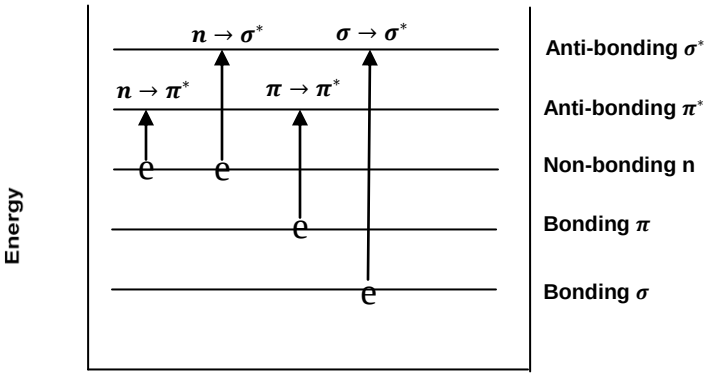

Fig. 2.5: Electronic transitions of σ, π, and n.[86]

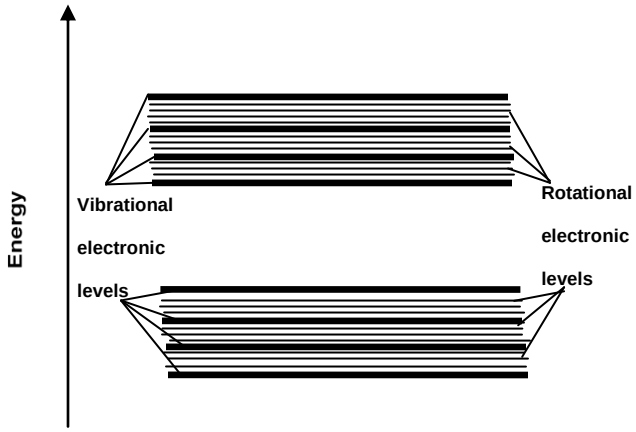

Fig. 2.6: Vibrational and Rotational Electronic Levels.[86]

$\sigma \rightarrow \sigma^*$ transitions

In this transition an electron requires a great deal of energy in order to promote it from a ground state to an excited state, and individual bond absorptions occur below 200 nm.[90] Compounds containing only σ bonds are transparent in the near UV-Visible region. The spectra are typically observed in the range of 200 to 700 nm.

$n \rightarrow \sigma^*$ transitions

Molecules containing atoms with non-bonding electrons are able to undergo this type of transition. These transitions very often require lower energy than $\sigma \rightarrow \sigma^*$ transitions. Light with a wavelength in the range 150–250 nm can initiate these transitions. Organic functional groups with this type of transitions have small peaks in the UV region.

$n \rightarrow \pi^*$ and $\pi \rightarrow \pi^*$ transitions

The absorption peaks of these transitions fall in the region of the spectrum from 200 to 700 nm. For providing the π electrons, these transitions require the presence of unsaturated groups known as chromophores in the molecule. The solvent has a crucial influence on the spectral features. By increasing solvent polarity, $n \rightarrow \pi^*$ transitions would be shifted to shorter wavelengths (blue shift), which occurs as a consequence of increasing solvation of the lone pair which would lower the energy of the n orbital. The reverse (red shift) would be seen for $\pi \rightarrow \pi^*$ transitions. The attractive polarization forces between the solvent and the absorber bring about this effect which would lower the ground energy levels and the excited energy levels. This influence has more impact for the excited state so that the energy difference between the ground state and the excited state is reduced, yielding a small red shift.

Charge-transfer absorption: Many inorganic compounds are coloured because transitions are occurring in the energy levels of the d electrons in the transition metal. Charge transfer is another type of transition which influences the colour in which an electron filling a σ or π orbital in the ligand is being promoted to an unfilled orbital of the metal, and vice-versa.[90] All the samples measurements were performed using ocean optics Inc. DT-Mini-2.

2.7 Principles of X-ray Photoelectron Spectroscopy

X-ray photoelectron spectroscopy (XPS) is also known as Electron Spectroscopy for Chemical Analysis (ESCA). It was developed by Siegbahn and his colleagues at the University of Uppsala, Sweden in 1967.[80] He was awarded the Nobel Prize in Physics in 1981.[92] The technique is based on the photoelectric effect.[93] It measures the kinetic energy of electrons that are ejected from a core level by an X-ray photon of energy $h\nu$, generally (Mg K_α,1254 eV or Al K_α, 1487 eV monochromatic radiation).The ionization radiation could be either X-ray or ultraviolet light, and thus the techniques are recognized as X-ray photoelectron spectroscopy (XPS) and ultraviolet photoelectron spectroscopy (UPS) respectively. The degree of accessibility of the ionization radiation to the electron shells is the main difference between XPS and UPS. XPS has sufficient energy to bring about ionization through ejection of inner shell electrons, whereas UPS does not have sufficient energy to emit an electron from the inner shells, freeing only electrons in the valence shell.[80] The difference between the energy, $h\nu$, of the incident radiation and the binding energy or ionization potential, E_b, of the electron provides the kinetic energy, E_k, of the ionized electron as follows:[80]

$$E_k = h\nu - E_b \qquad \textbf{(2.14)}$$

When an X-ray beam hits the sample, the energy of the X-ray is adsorbed completely by the core electron of an atom. If the photon energy, $h\nu$, is sufficient, the core electron will escape

from the atom and be ejected from the surface. The ejected, kinetically energetic electron is referred to as the photoelectron. The binding energy of the inner electron is given by the equation:[93]

$$h\nu = E_b + E_k + \omega \qquad \textbf{(2.15)}$$

where $h\nu$ is the photon energy, E_k is the kinetic energy of the photoelectron, and ω is the spectrometer work function. The process of the photoemission of electrons is shown schematically in Fig. 2.7.

XPS spectra lines are distinguished by the shell from which the electron was emitted (1s, 2s, 2p,3p, etc.).[93]

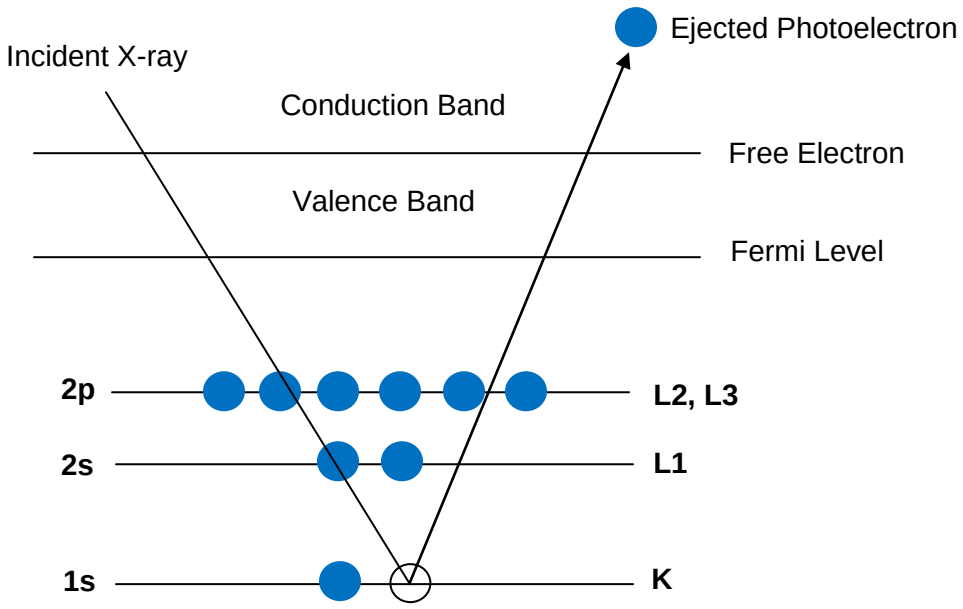

Fig. 2.7: Schematic diagram of the XPS process, showing photoionization of an atom by the ejection of a 1s electron.[93]

XPS has many advantages such as identification of the elements in which exist at the surface from the kinetic energies of the ejected photoelectrons, the ability to gain information on chemical states from the variations in binding energies, or chemical shift of the photoelectron

lines, the relative concentration of these elements from the photoelectron intensities. All the samples measurements were performed using a Thermo-VG Scientific ESCALab 250 Microprobe, which is equipped with a monochromatic $Al\ K\alpha$ X-ray source (1486.6 eV) operated at a typical energy resolution of 0.4–0.5 eV full width at half maximum.

2.8 Overview of Thermal Gravimetric Analysis

Thermal Gravimetric Analysis (TGA) is used to observe the change in the mass of a sample as a function of temperature. Typically, a small amount of weighted sample is placed in an controlled environment such as nitrogen, argon, or even air. Subsequently, the weight of the sample is observed as the temperature is changed at a fixed rate. Thermal processes that lead to changes such as decomposition, oxidation and reduction can be observed and their temperature dependence can be studied. The sample measurement was performed using Q-500 TGA (TA instrument), in a nitrogen atmosphere with temperature increase at a rate of 10 °C/min.

Chapter 3. Fabrication of Graphene Oxide Films

3.1 Objective of Chapter

This chapter details the preparation of GO films by vacuum filtration using Anodisc membrane filters (25 mm in diameter, 0.02 μm pore size). The films are then subjected to thermal reduction and chemical reduction. Simple multivalent ions such as Mg^{2+}, Ba^{2+}, Fe^{2+}, and Fe^{3+} are also used for chemical cross linking of the GO sheets. The thermal reduction is performed over a range of temperatures (60, 180, 200, 225, 250, and 300 $^{\circ}$C) to study its effect on the GO films. The objective of these treatments is to manipulate the d-spacing between the GO layers in the film and to provide a means for its control. This ability to alter the d-spacing forms the basis for controlling the electrical and diffusion characteristics of these films and is discussed in chapter 4. TGA was performed to determine the thermal stability of the GO film. X-ray diffraction was used to characterize the GO films and calculate the inter-layer spacing. FT-IR, Raman, and XPS spectroscopies were used to confirm reduction by observing a decrease in concentration for oxygen containing functional groups.

3.2 Synthesis of Colloidal Graphene Oxide

In this work, graphene oxide (GO) was synthesized according to a modified Hummer`s method.[94] It has two stages: the first step involves pre-oxidation, and the second involves full intensive oxidation, filtering and washing to remove residual chemicals and contaminates. The first stage was carried out as follows: 50 ml of sulfuric acid (H_2SO_4) was added drop wise to a mixture of graphite flakes (3 g), potassium persulfate, ($K_2S_2O_8$, 2 g), and phosphorous penta oxide (P_2O_5, 2 g) followed by stirring and heating at 90 $^{\circ}$C until the powder dissolved. The temperature was decreased to 80 $^{\circ}$C, and the mixture was stirred for four hours. After that, 500 ml of Millipore water was added very slowly (it is recommended to use a separatory funnel to slowly add the water), since the reaction is vigorously exothermic. The mixture was stirred

overnight. The solution was washed with Millipore water until the rinsed solution, which was expected to be brown, reached pH~7. The product was dried in ambient air for 18–24 h. This forms the pre-oxidized powder that is subjected to intense oxidation in the second stage. In the second stage, which involves full oxidation, the pre-oxidized graphite powder was added to 15 g potassium permanganate ($KMnO_4$) and 125 mL H_2SO_4 under continuous stirring in an ice-bath. After two hours of stirring, 130 mL Millipore water was added very slowly, which caused the temperature to rise to 90–95 $^{\circ}$C. Under continuous stirring another 400 mL of Millipore water was added. After 10 min, 15 mL of H_2O_2 was added, causing the solution to become bright yellow, which is as an indication of reduction the manganese. The solution was stirred overnight. After that, the product was washed with HCl (10%) then with Millipore until the solution reached pH 7. The brown dispersion was placed in a Spectra/Por dialysis membrane (29 mm diameter, Spectrum Laboratories, Inc.) to get rid of metal ions and acids.

3.3 Synthesis of Graphene Oxide Films

All the films in this thesis have been prepared via vacuum filtration of a GO suspensions through Whatman Anodisc membrane filters (high purity alumina matrix bonded to a polypropylene ring, 25 mm in diameter, 0.02 μm pore size). The film thickness can be controlled by either the concentration of the GO in the suspension or by the filtration volume.[95] The technique and fabrication of graphene oxide films are illustrated in Fig. 3.1:

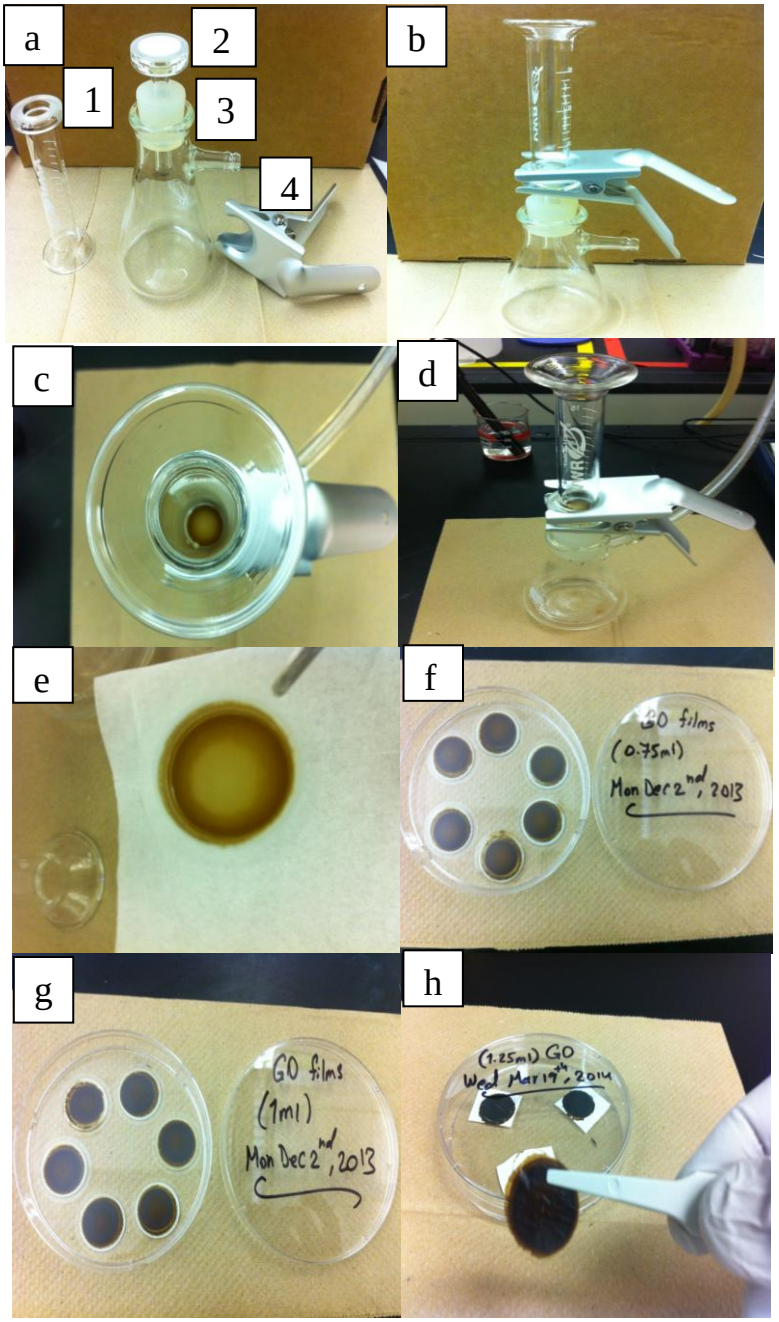

Fig. 3.1: Vacuum pump filtration set up. (a). (1) 15 ml glass funnel. (2) Fritted glass support base. (3) Silicon stopper. (4) Aluminum clamp. (b) Full assembly. (c) Top view of GO film synthesis. (d) Side view of GO film synthesis. (e) 0.25 ml filtered GO colloidal. (f) 0.75 ml filtered GO colloidal. (g) 1 ml filtered GO colloidal. (h) 1.25 ml filtered GO colloidal.

3.4 Thermal Gravimetric Analysis of Graphene Oxide Films

The particular conditions used in oxidation, exfoliation, and film formation of GO influence the response of film samples to heat. TGA is a standard analytical method used for characterization of the thermal response of graphitic materials. TGA curves relating the mass loss of the GO films with temperature show distinct stages. The stages correspond to mass loss due to certain physical or chemical changes occurring in the GO films. It is well-established in the literature that three transitions,[96] that is, temperature ranges associated with notable mass loss, are observed for GO samples. A low temperature transition is associated with removal of adsorbed water; an intermediate transition is associated with removal of oxygen functional groups; and, a third transition at high temperature is associated with decomposition of the carbon skeleton. As our objective was to control the extent of reduction, TGA was used to identify the suitable temperature range for thermal reduction of the GO films. The change in inter-layer spacing of the GO films with thermal treatment is corroborated by TGA. There is a change in the mass of the starting GO film as the temperature is increased from ambient conditions to 900 $^{\circ}$C. As seen in Fig. 3.2, three transitions that lead to weight loss are observed over the temperature range of the experiments. In the range of 60–100 $^{\circ}$C, the expected loss in weight associated with the removal of residual water molecules in the GO film is observed.[96] We observed a sharp transition centered at 200 $^{\circ}$C, which is associated with the oxygen loss and is the desired transformation for the thermal reduction of our GO films. Finally, at a temperature of ~ 545 $^{\circ}$C, pyrolysis of the film reduces the weight nearly to zero. A set of temperatures surrounding the 200 $^{\circ}$C transition were selected for thermal reduction to study their effect on the inter-layer d-spacing of the thermally reduced GO films. Following this, the effect of the d-spacing on the metal ion diffusion across these thermally reduced GO films was investigated.

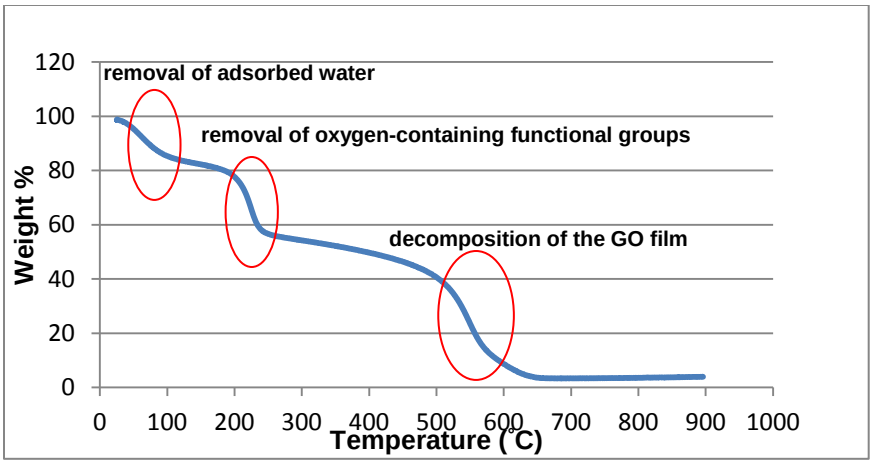

Fig. 3.2: Thermal gravimetric analysis (TGA) of graphene oxide film.

3.5 Thermal Reduction of Graphene Oxide Films

Thermal reduction leads to an evaporation of the intercalated water and evolution of gases produced by thermal pyrolysis of the oxygen-containing functional groups. GO films were reduced at six different temperatures (60, 180, 200, 225, 250, and 300 ˚C) in order to control their d-spacing and the extent of reduction. A schematic showing the ideal reduction of GO into reduced graphene oxide is shown in Fig. 3.3, where all the oxygen- containing functional groups are removed and the π network is completely restored.

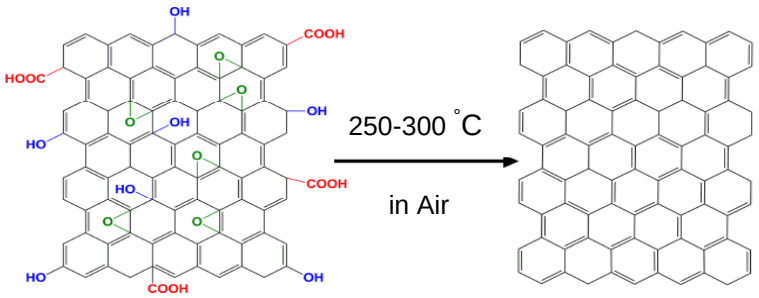

Graphene oxide ⟶ Graphene + O_2 + CO + CO_2 + H_2O

Fig. 3.3: Schematic of the reduction of graphene oxide into reduced graphene oxide by thermal treatment (taken from ref.[97] with permission from the Royal Society of Chemistry).

As thermal reduction causes the removal of intercalated water and the oxygen functional groups, it should lead to a decrease in the inter layer spacing in the GO membrane. This decrease should depend on the extent of the GO reduction. X-ray diffraction (XRD) is used to characterize the GO films, and, as described in Chapter 2, provides for the calculation of the d-spacing in layered structures from the position of the reflection peak by the use of Bragg's Law.

The X-ray diffraction for GO films reduced at different temperatures (60, 180, 200, 225, 250, and 300 °C) is illustrated in Fig. 3.4. It can be seen that a strong peak for GO film treated at 60 °C is present at $2\theta = 12^{\circ}$, which corresponds to an inter-layer spacing of 7.4 Å. The effect of thermal reduction can be seen by exposing the GO films for 30 minutes to different temperatures in air, namely, 180 °C, 200 °C, 225 °C, 250 °C, and 300 °C.

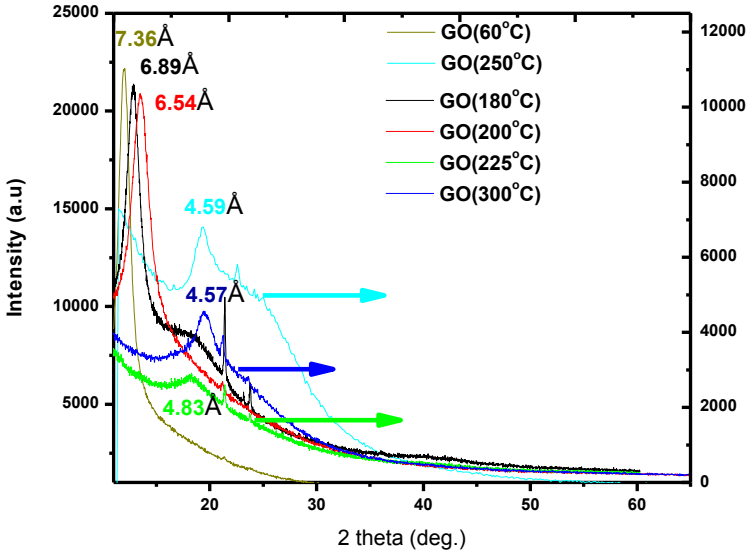

Fig. 3.4: X-ray diffraction patterns for the GO films reduced at different temperatures.

As a consequence of heat exposure, the peak corresponding to the inter-layer spacing was shifted to a larger angle signifying the reduction in the inter- layer spacing of the GO film. The spacing is observed to decrease gradually from 7.4 Å to 6.9 Å and 6.5 Å, respectively, as

the temperature of reduction is increased from 60 °C to 180 °C to 200 °C. Following this a drastic change was observed upon increasing the reduction temperature to 225 °C as the spacing reduces to 4.8 Å. Following this, little change was observed on increasing the temperature to 250 °C or 300 °C, which respectively brought about spacings of 4.6 Å and 4.57 Å. The change in going from 60 to 180 °C corresponds to the evaporation of the residual water molecules in these films. An increase in temperature to 225 °C causes the removal of the oxide functional groups on the surface of the GO films. These are primarily the defects caused by the oxidative treatment of the graphite for exfoliation to form GO sheets. Further increases in temperature only cause a slight change in the spacing leading to the conclusion that most of the defects have been removed at 225 °C. The thermal treatment of the GO film was hence limited to 250 °C for future samples. The GO films reduced at 225 °C, 250 °C, and 300 °C have broad peaks due to the distribution of d-spacing since the sheets are not aligned perfectly, there are such as waves. The effect of temperature on reducing the d-spacing of the GO films is shown in Fig. 3.5. Based on the steep decrease in the d-spacing on thermal treatment of the films at temperatures above 200 °C, and the associated loss of mass in TGA, it confirms that removal of oxygen-containing functional groups occurs in this temperature range.

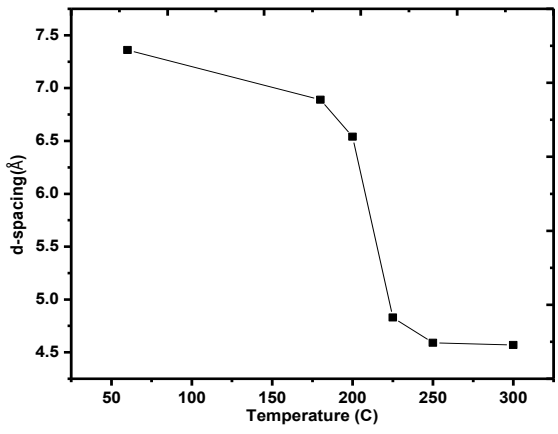

Fig. 3.5: d-spacing for the non reduced and reduced GO films versus temperature.

It can be seen from Fig. 3.6 that the color changes with increasing temperatures from dark brown to black to grey to shiny grey. The brown color in GO (60 °C) was attributed to intercalation of water molecules as well as oxygen functional groups which disrupt the π network system. GO treated at (180 °C) is almost black which is attributed to the partial removal of oxygen functional groups and reduction of the d-spacing inter-layer. The color was changed to a grey in GO (200 °C) which was attributed to the removal of more oxygen functional groups. In GO (225 °C), the color was changed to shiny grey which ascribed to elimination of most of the oxygen functional groups and partial restoration of the π network system. Finally, all the oxygen functional groups were removed in GO at 250 °C and at 300 °C.

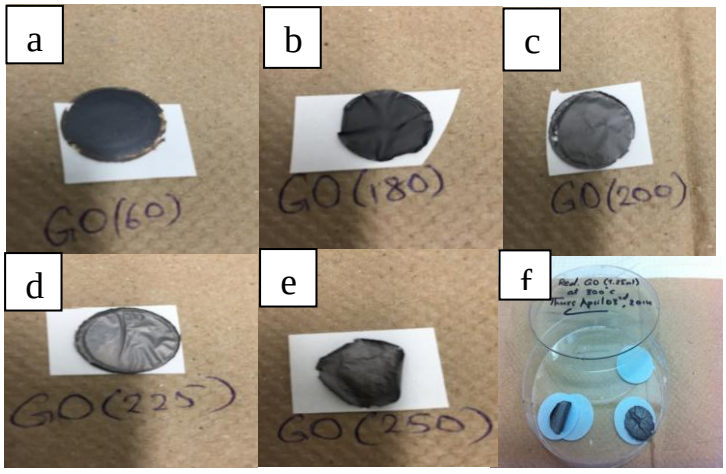

Fig. 3.6: Non-reduced and reduced GO films.(a) GO (60 °C). (b) GO (180 °C). (c) GO (200 °C). (d) GO (225 °C). (e) GO (250 °C). (f) GO (300 °C).

3.6 Chemical Reduction of Graphene Oxide Films

Graphene oxide (GO) is thermally unstable due to the presence of the oxygen functional groups. It is also electrically insulating. It has been reported that electrical conductivity and the thermal stability of the GO can be restored by chemical reduction.[98,99,100,101] The purpose of using the chemical reduction for the GO films is just to explore the reduction in the inter-layer spacing in comparison to thermal reduction without any further studies related to practical applications. Two widely used reducing agents, hydrazine vapor, and ascorbic acid were selected for this purpose.

3.6.1 Reduction of Graphene Oxide Films with Hydrazine (N_2H_4) Vapor

The chemical reduction of GO film (rGO) has been examined using the reducing agent of hydrazine hydrate vapor. A fresh GO film was placed in an empty small beaker which was placed in a large beaker containing approximately 10 mL N_2H_4. The large beaker was covered with aluminum foil and placed on a hot plate at 80 $^{\circ}$C for 40 minutes, during which the colour of the film changed from brown to grey, indicated the reduction of the GO film. Fig. 3.7 depicts the reduction of the GO film via $N_2H_4 \cdot H_2O$.

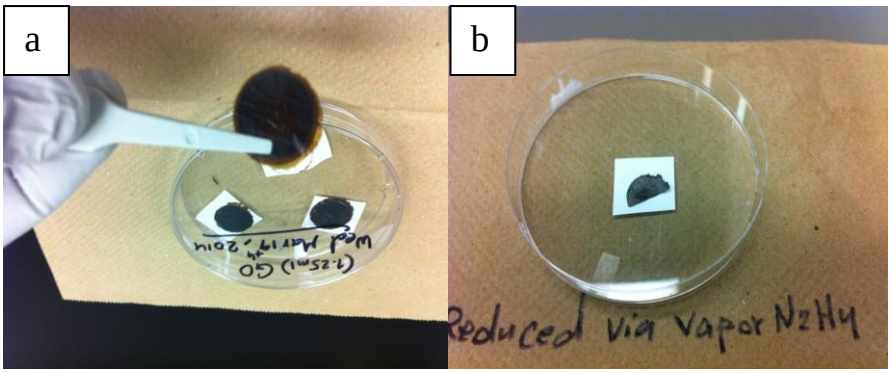

Fig. 3.7: (a) Non-reduced GO film. (b) rGO film via N_2H_4 vapor.

3.6.2 Reduction of Graphene Oxide Films with Ascorbic Acid ($C_6H_8O_6$)

Approximately 10 mg of GO was dispersed into Millipore water by sonication for an hour then the pH of the dispersion was adjusted to ~ 9–10 with a very small amount of sodium hydroxide (NaOH)[50]. After which an appropriate amount of ascorbic acid ($C_6H_8O_6$) was added while the suspension was maintained in a silicon oil bath at 90 °C until the colour changed to black. A portion of the reduced solution was filtered through the Anodisc membrane filter to obtain rGO film. The non-reduced, reduced solution and the reduced film are shown in Fig. 3.8.

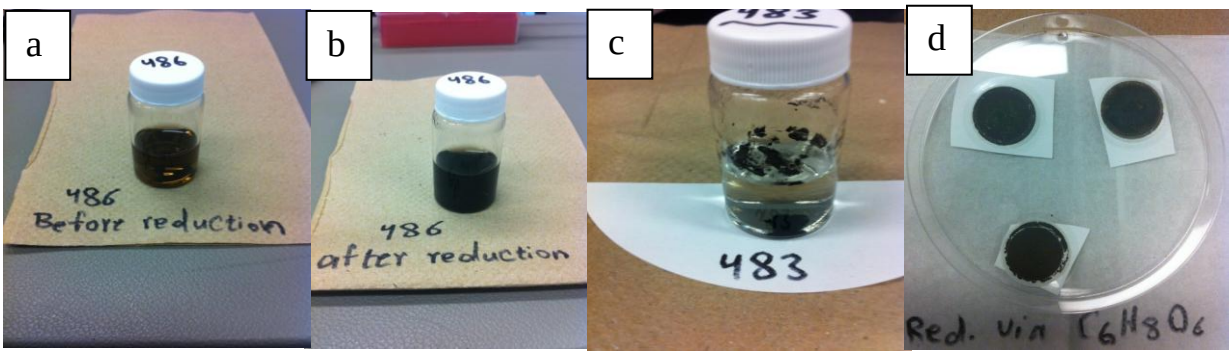

Fig. 3.8: Non-reduced and rGO by $C_6H_8O_6$.(a) GO before reduction. (b) right after reduction. (c) agglomeration. (d) rGO films.

The change in the color of the graphene oxide dispersion from brown to black is an indication of the removal of oxygen containing functional groups. This also causes the reduced graphene oxide sheets to become hydrophobic and leads to their agglomeration and precipitation. Likewise, when the hydrazine hydrate vapor was used as a reducing agent for the GO film, the color of the film was changed from brown to dark grey as an indication of elimination of the oxygen functional groups and partial restoration of the π network.

X-ray diffraction was used to characterize the inter-layer spacing in the non-reduced, thermally reduced, and chemically reduced GO films. X-ray diffraction of non-reduced GO film, GO film reduced at 250 °C, GO film reduced by hydrazine hydrate vapor, and GO film reduced by ascorbic acid is illustrated in Fig. 3.9.

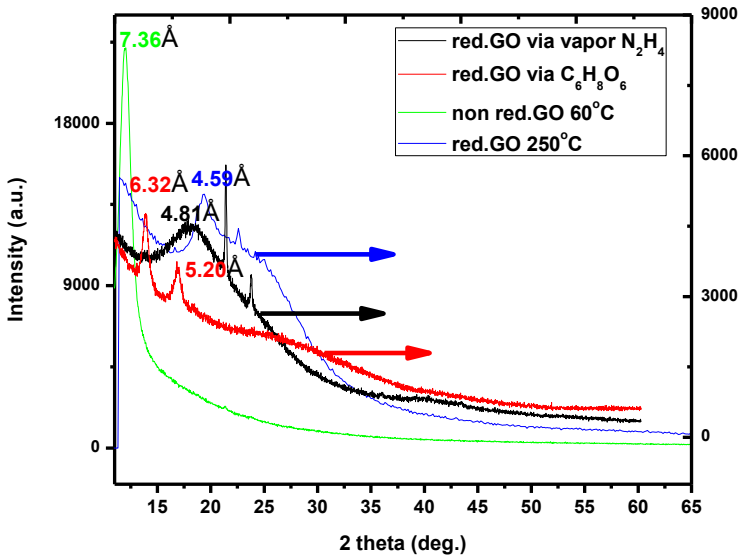

Fig. 3.9: X-ray diffraction of non-reduced GO film, thermally reduced GO film at 250 °C, and chemically reduced GO film via vapor N_2H_4 and $C_6H_8O_6$.

It can be seen that the non-reduced GO film has a sharp peak located at the lowest angle for this set of observations, whereas the variously reduced films exhibit peaks shifted to higher angles indicating smaller d-spacing. The presence of oxygen functional groups as well as water molecules leads to a larger inter-layer in the non-reduced GO film compared to either thermally or chemically reduced GO.[102] Non-reduced GO has a strong peak at $2\theta = 12^{\circ}$ corresponding to an inter-layer spacing of 7.4 Å, however, the thermally reduced GO (at 250 °C) has a peak at $2\theta = 19^{\circ}$ corresponding to an inter-layer spacing of 4.59 Å. Chemically reduced GO (with $C_6H_8O_6$) has two peaks at $2\theta = 14^{\circ}$ and $2\theta = 17^{\circ}$, corresponding to the inter-layer spacing of 6.32 Å and 5.20 Å, respectively. The chemically reduced GO with hydrazine has a broad peak at $2\theta = 18.5^{\circ}$ corresponding to an inter-layer spacing of 4.81 Å. For hydrazine vapor reduction a solid film is used to avoid agglomeration and precipitation. The inter-layer spacing of 4.81 Å is much smaller than non-reduced GO, which has inter-layer spacing 7.4 Å. However, the GO reduced by $C_6H_8O_6$ has two peaks, probably resulting from a bimodal or multimodal

distribution in the inter-layer spacing. This can arise due to partial agglomeration of the GO sheets in the solution on reduction prior to their filtration for the formation of the films.[96,103]

3.7 Chemical Cross-linking of Graphene Oxide Films

The purpose of using the chemical cross-linking for the GO films is just to explore the reduction in the inter-layer spacing without any further studies related to practical applications. Five cross-linker ions were selected for study: Na^{+}, Ba^{2+}, Fe^{2+}, Fe^{3+}, and Mg^{2+}.

An appropriate amount of GO was dispersed into Millipore water by sonication for an hour, then an appropriate amount of barium chloride dihydrate ($BaCl_2 \cdot 2H_2O$), iron(II) chloride tetrahydrate ($FeCl_2 \cdot 4H_2O$), magnesium chloride hexahydrate ($MgCl_2 \cdot 6H_2O$), iron(III) chloride hexahydrate ($FeCl_3 \cdot 6H_2O$), and sodium chloride (NaCl) were added into different sample vials of GO solution, a summary of sample designation and associated cross-linkers is given in table 3.1. The solution was stirred briefly, then the mixture was filtered via Anodisc membrane filter (25 mm in diameter, 0.02 µm pore size, Whatman), to obtain a uniform film, and finally the obtained different films were annealed at 250 $^{\circ}$C in air, after which X-ray diffraction experiments were performed on all the films for characterization. The X-ray diffractions results are shown in Fig. 3.10:

Table 3.1: The sample ID and the different used cross-linker.

Sample ID	Cross-linker	Ionic radius	d-spacing
Non-reduced GO	None	----------	7.40 Å
Reduced GO	None	----------	4.58 Å
GO:Na^{+}	Na^{+}	0.95 Å	4.65 Å
GO:Mg^{2+}	Mg^{2+}	0.65 Å	4.41 Å
GO:Fe^{2+}	Fe^{2+}	0.75 Å	4.65 Å
GO:Ba^{2+}	Ba^{2+}	1.35 Å	4.73 Å
GO:Fe^{3+}	Fe^{3+}	0.60 Å	4.69 Å

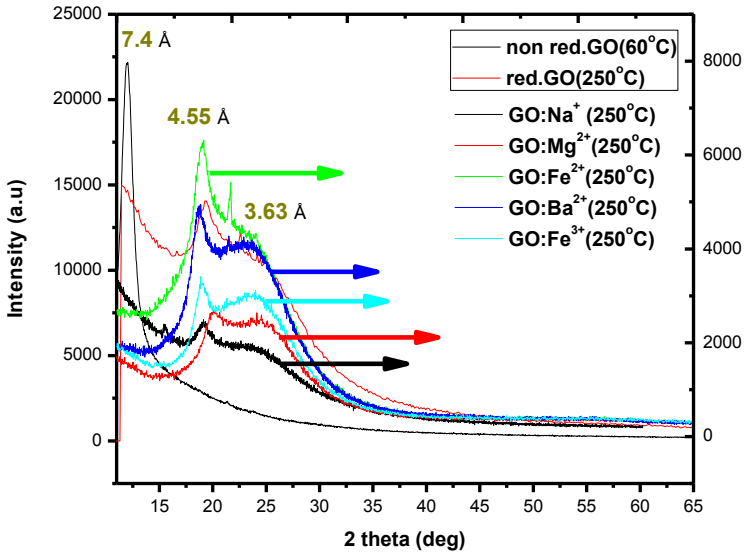

Fig. 3.10: X-ray diffraction patterns for different chemical cross-linkers in GO film.

From the above Fig. 3.10. It can be seen that no significant difference in the d-spacing between the thermally reduced film at 250 °C and the chemically cross-linked films, which were also reduced at 250 °C, was observed. One interpretation of this finding is that, under the

preparation conditions, and at the relative reagent proportions, no appreciable metal ion intercalation was achieved; therefore, the agreement of the two theta values among these samples is ascribed to their d-spacing being governed solely by thermal reduction. Further studies need to be done in order to manipulate the molar ratios between the GO and the cross-linkers so that we could observe reduction in the d-spacing.

3.8 FT-IR Spectroscopy of Graphene Oxide Films

FT-IR spectroscopy has been done for the following films (GO-RT, GO 60 °C, GO 180 °C, GO 200 °C, GO 225 °C, and GO 250 °C) to confirm that oxygen functional groups were completely removed at 225 °C and 250 °C, which is an indication that thermal reduction has occurred. FT-IR spectra of thermally reduced films at different temperatures is shown in Fig. 3.11. The peak located at ~ 3400 cm^{-1} belongs to stretching vibrations of hydroxyl groups on the plane, which is attributed to the absorbed water between graphene layers.[104] The peaks located at 2400, 1730, 1623, 1410, 1228, 1059 cm^{-1} are attributed to carbon dioxide, carbonyl groups located at the edges of the sheets, aromatic C=C bonds, bending hydroxyl groups, epoxy, and the stretching vibration of alkoxy R-O, respectively.[102] During the oxidation of graphite powder, oxygen functional groups are introduced in the graphite structure partially destroying the conjugated π network. The carbonyl groups and the residual sp^2 structure and lead to the bands at 1623 cm^{-1} and 1730 cm^{-1}. After thermal reduction particularly at 225 °C and above, the peaks located at 3400, 2400, 1730, 1228, and 1059 cm^{-1} almost disappear as a consequence of the removal oxygen functional groups, however, thermal annealing at lower than 225 °C only results in a slight decrease in these peaks, indicating the persistence of oxygen functional groups in the GO films.

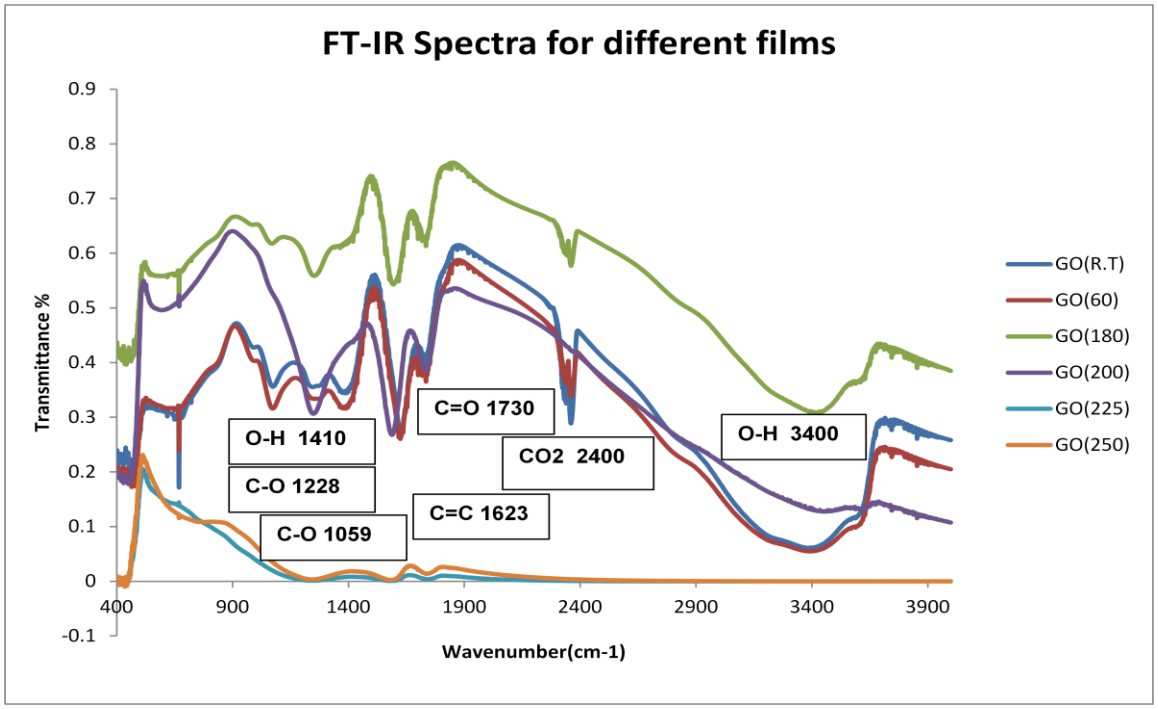

Fig. 3.11: FT-IR spectra of non-reduced GO film (RT) and those thermally annealed at a series of elevated temperatures.

3.9 Raman Spectroscopy of Graphene Oxide Films

The electronic structure and the degree of reduction of GO films can be investigated and characterized via Raman spectroscopy. Raman spectroscopy of the non-reduced GO films (GO-RT, GO 60 $^{\circ}$C) and those progressively reduced at different annealing temperatures (GO 180 $^{\circ}$C, GO 200 $^{\circ}$C, GO 225 $^{\circ}$C, and GO 250 $^{\circ}$C) are shown in Fig. 3.12. For comparison, the Raman spectrum of graphite is also presented. Graphite represents two Raman peaks, the first one being a strong band at 1574 cm^{-1} (G band) which corresponds to the vibration of the carbon atoms in the graphitic carbon layers,[104] and the second a weak band at 1350 cm^{-1} corresponding to the presence of disordered carbon atoms.[102] By comparing the G band of graphite with the rest of the films, it can be seen clearly that as the annealing temperature increases for the films, the G band is shifted to lower frequencies, approaching the G band of graphite. For instance, the G bands for the non-reduced GO film and GO 180 $^{\circ}$C are at 1593

and 1594.5 cm^{-1}, respectively, however, as the annealing temperature increases up to 220 °C, 225 °C, and 250 °C, the G band is shifted to 1583.7, 1584.7, and 1585.7 cm^{-1}, respectively, which is strong evidence for the restoration of the graphitic sp^2 network.[104] These results are consistent with our XRD data for all the films.

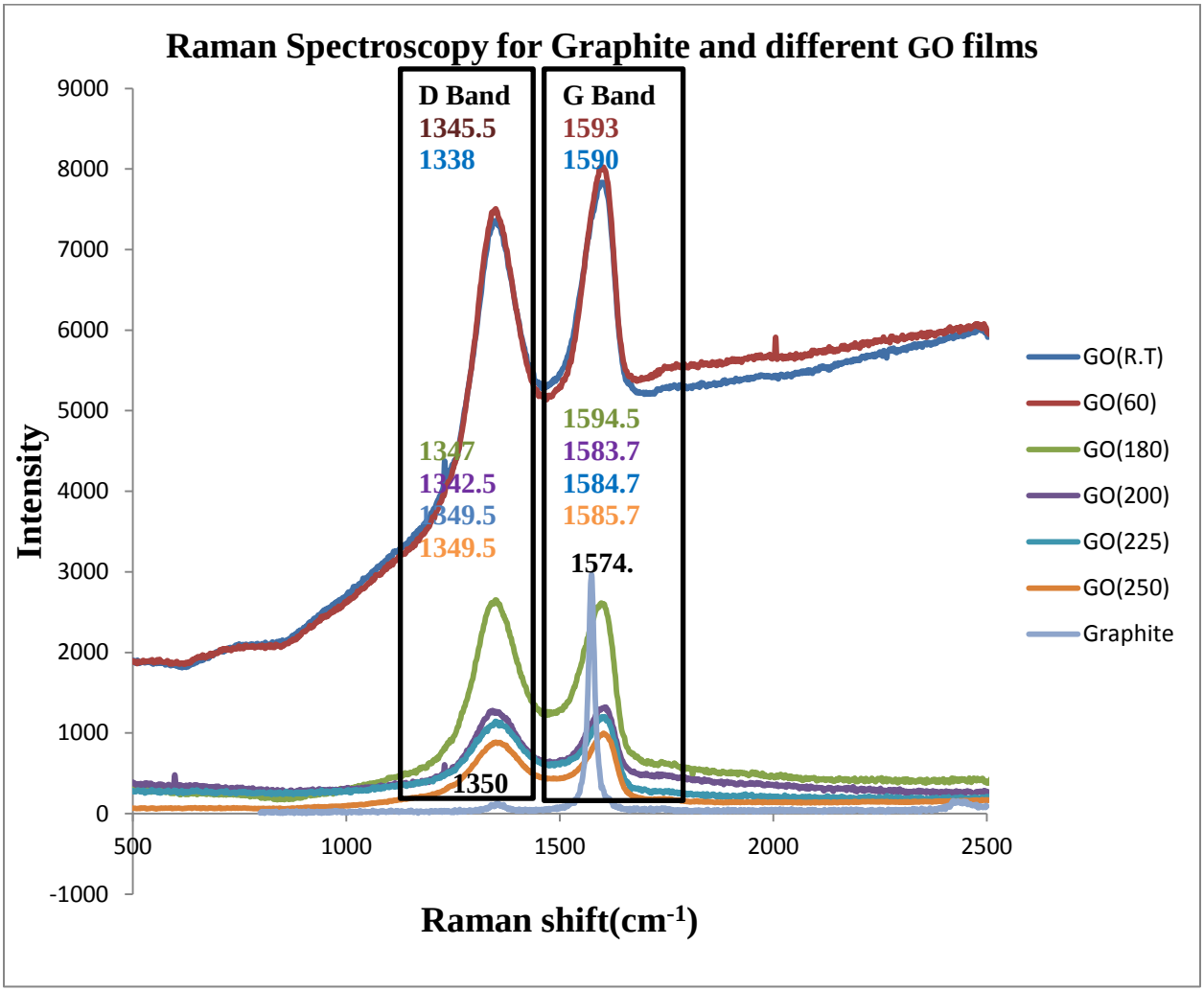

Fig. 3.12: Raman spectroscopy of graphite and GO films reduced at several annealing temperatures.

3.10 XPS of Non-Reduced and Reduced Graphene Oxide Films

The removal of the oxygen-containing functional groups has also been confirmed via XPS. XPS spectra of GO 60 °C, GO 250 °C, and GO chemically reduced by N_2H_4, and ascorbic acid ($C_6H_8O_6$) are shown in Figs. (3.13 –3.20). Two strong peaks are located at 284.4 eV and 531.9 eV. They are attributed to the elemental carbon C 1s of sp^2 and the elemental oxygen O 1s respectively.[105] It can be seen clearly that the C/O ratio increases markedly after thermal reduction at 250 °C as well as after chemical reduction of GO via both hydrazine and ascorbic acid. It was increases from 0.52 to 2.55, 1.94, and 0.86 after thermal reduction at 250 °C, chemical reduction by vapor hydrazine, and by ascorbic acid respectively. This is an indication that most of the epoxide and hydroxyl functional groups were successfully eliminated.[96] The XPS data is consistent with our TGA data in terms of the mass loss observed as well as with our FT-IR spectroscopy in terms of the removal of oxygen-containing functional groups.

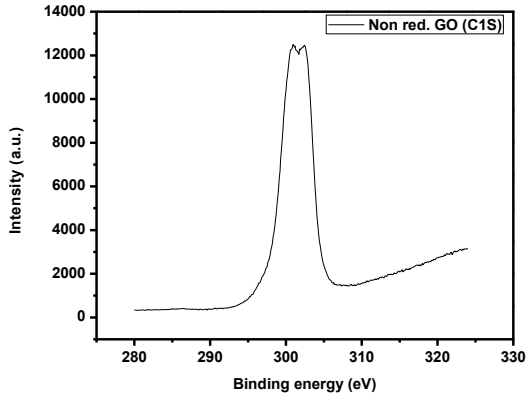

Fig. 3.13: C1s XPS spectrum of GO 60 °C.

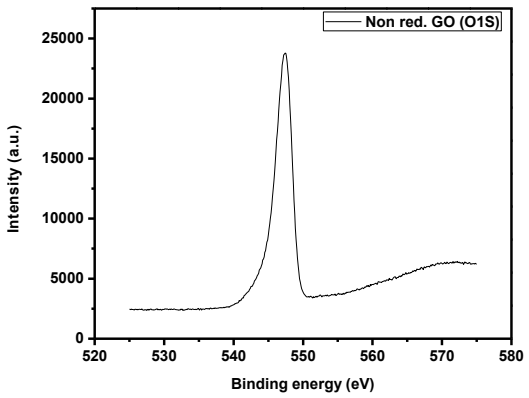

Fig. 3.14: O1s XPS spectrum of GO 60 °C

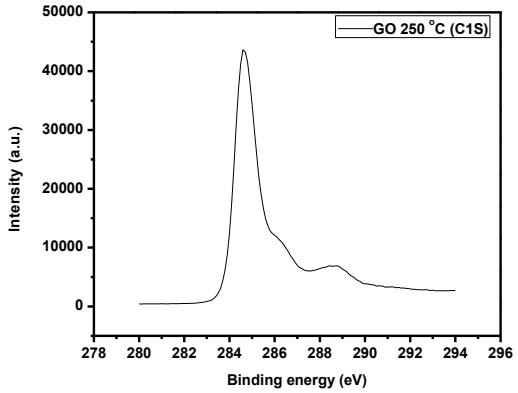

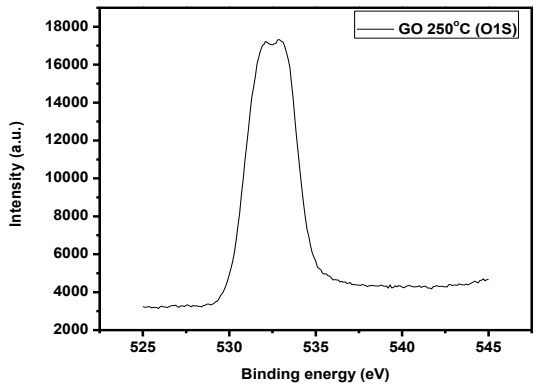

Fig. 3.15: C1s XPS spectrum of GO 250 °C.

Fig. 3.16: O1s XPS spectrum of GO 250 °C.

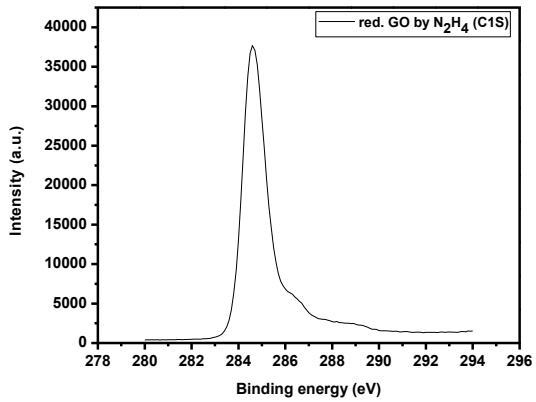

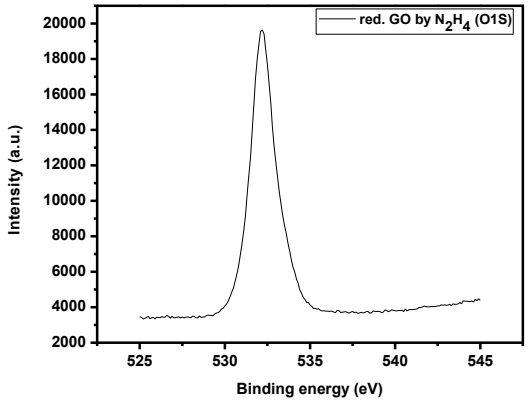

Fig. 3.17: C1s XPS spectrum of GO reduced by N_2H_4.

Fig. 3.18: O1s XPS spectrum of GO reduced by N_2H_4.

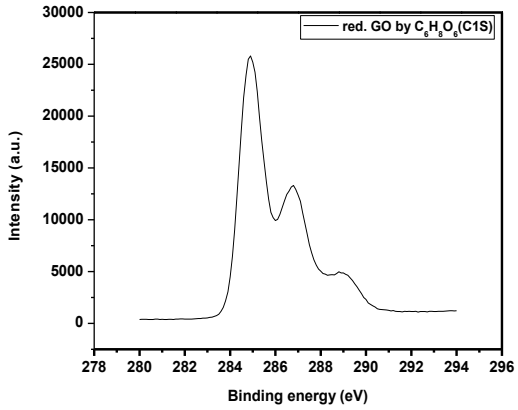

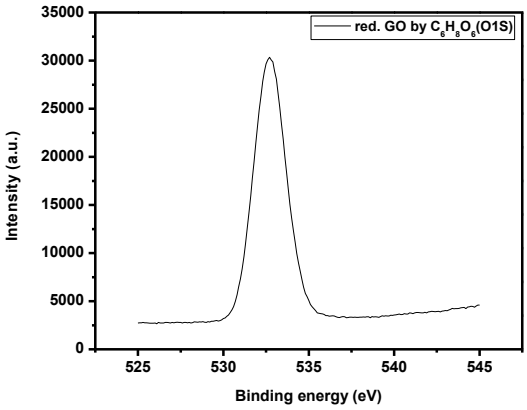

Fig. 3.19: C1s XPS spectrum of GO reduced by $C_6H_8O_6$. Fig. 3.20: O1s XPS spectrum of GO reduced by $C_6H_8O_6$.

3.11 Mechanical Test of Graphene Oxide Films

Heat treatment is able to change the properties and behavior of GO films. For instance, after different extents of thermal annealing (180 °C, 200 °C, 225 °C, 250 °C, and 300 °C), the films become electrically more conductive due to partial restoration of the π network system; however, their mechanical properties deteriorate. Tensile tests have been done for the following films (GO film at room temperature (GO RT), GO 180 °C, GO 200 °C, GO 225 °C, GO 250 °C, and GO 300 °C). All the films were cut with scissors into rectangular strips of approximately 7 mm × 10 mm for mechanical tests. The film before and after the test are shown in Fig. 3.21. All the sample measurements were performed using dynamic mechanical thermal analyzer (DMTA V), Rheometric Scientific.

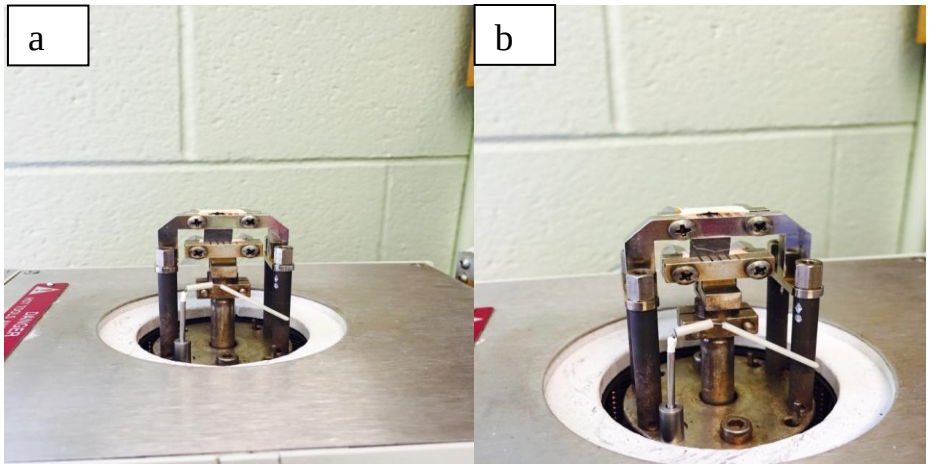

Fig. 3.21: (a) GO film before mechanical test. (b) GO film after mechanical test.

The results for tensile test of all the GO films are shown in Figs. (3.22–3.25).

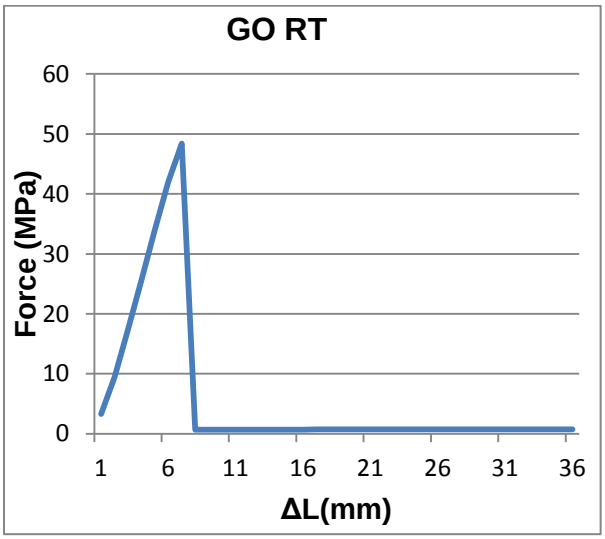

Fig. 3.22: Tensile strength of GO RT.

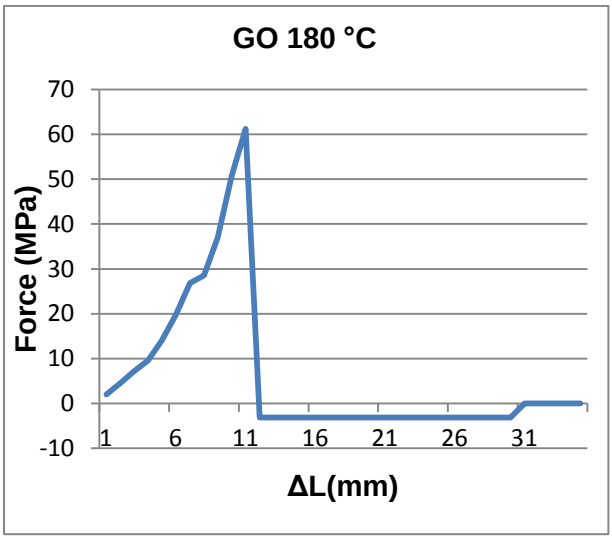

Fig. 3.23: Tensile strength of GO 180 °C.

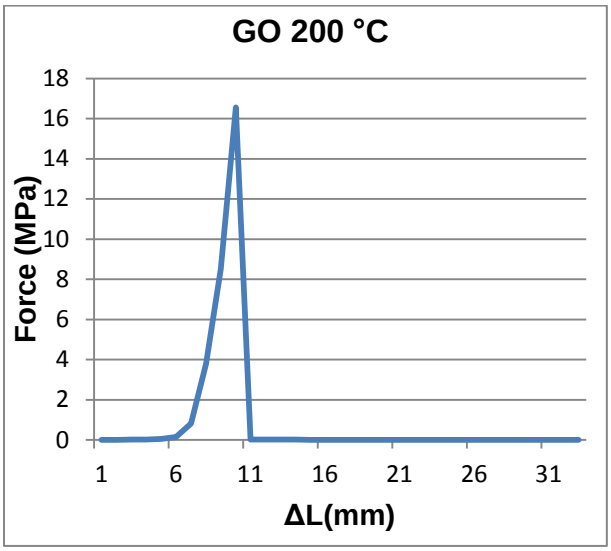

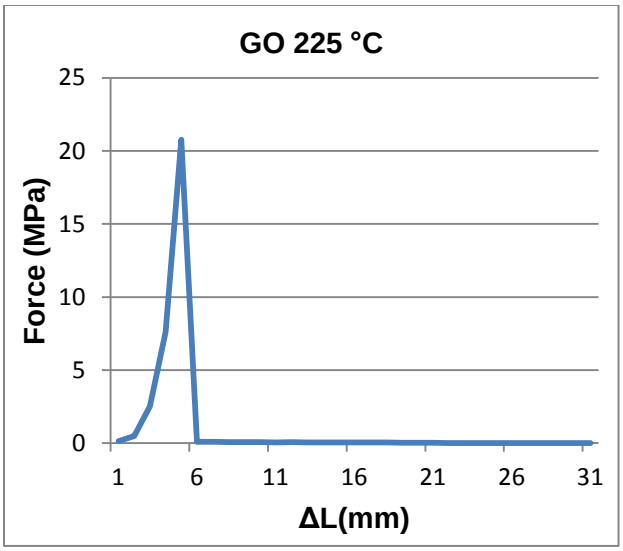

Fig. 3.24: Tensile strength of GO 200 °C.

Fig. 3.25: Tensile strength of GO 225 °C.

The GO RT film which is processed only at room temperature possesses a tensile strength of ~ 49 MPa. It possess residual water as well as oxygen functional groups. However, when the temperature was increased to 180 °C, all the residual water was removed, while the oxygen functional groups were still present. The resulting tensile strength was ~ 61 MPa. When the temperature reached 200 °C and 225 °C, there was large reduction in the tensile strengths, which respectively declined to ~ 17 MPa and ~ 21 MPa. The reduced graphene oxide film appears to be more brittle since all the oxygen functional groups have been eliminated.[106] Further evidence is that the GO 250 °C and GO 300 °C films were extremely brittle and tore immediately at the beginning of the tensile strength test, which is why at the highest temperatures, tensile values are unavailable. As the functional groups on the film are removed, the inter-layer bonding between the sheets decreases and this leads to their brittle behavior. These results are consistent with our TGA and XRD measurements.

3.12 Conclusions for Chapter Three

GO films were prepared by vacuum filtration of a GO suspension through Anodisc membrane filters. The prepared films were thermally reduced at six different temperatures (60 $^{\circ}$C, 180 $^{\circ}$C, 200 $^{\circ}$C, 225 $^{\circ}$C, 250 $^{\circ}$C, and 300 $^{\circ}$C). Thermal reduction leads to the removal of the residual water in the film and also the oxygen-containing functional groups. These transformations of the GO films were characterized by using XRD, TGA, FT-IR, Raman spectroscopy, and XPS.

Our primary interest was in the observed transition of the inter-layer spacing which reduced from 7.4 Å to 4.57 Å as a function of the temperature of thermal reduction. This change in spacing was observed by XRD and it occurred primarily between the temperatures of 200–250 $^{\circ}$C.

The effect of thermal reduction was also observed by weight loss in TGA. Here a weight loss associated with the removal of water is observed in the temperature range of 60–100 $^{\circ}$C. Another weight loss transition is observed from 200–250 $^{\circ}$C corresponding to the removal of oxygen-containing functional groups. This matches with the reduction in the inter-layer spacing of these films as observed in the XRD results noted above.

The results from FT-IR and Raman spectroscopy also confirmed the removal of the oxygen-containing functional groups on thermal reduction. In FT-IR, the peak located at ~ 3400 cm^{-1} belongs to stretching vibrations of hydroxyl groups on the plane, which is attributed to the absorbed water between graphene layers. The peaks located at 1730, 1623, 1410, 1228, 1059 cm^{-1} are attributed to carbonyl groups located at the edges of the sheets, aromatic C=C bonds, bending hydroxyl groups, epoxy, and the stretching vibration of alkoxy R-O, respectively. After thermal reduction particularly at 225 $^{\circ}$C and above, the peaks located at 3400, 1730, 1228, and 1059 cm^{-1} almost disappear as a consequence of the removal oxygen functional groups. The

results from Raman spectroscopy also show that the G band shifts to lower frequency approaching that of graphite as a function of reduction temperature. Further, the oxygen-containing functional groups leads to inter-layer bonding in these films and their removal by thermal reduction is also manifested in the mechanical properties of the films. Consistent with previous observations thermal reduction at 225 $^{\circ}$C and higher temperatures significantly reduces their tensile strength and make them brittle.

Chemical reduction of GO was performed by using hydrazine vapor (on GO film) and ascorbic acid (GO in colloidal form). The chemical reduction was used as a parallel method of reduction to contrast with thermal reduction in my research. The results from XRD characterization show that thermal reduction provides a smaller inter-layer spacing with better consistency compared to chemical reduction methods. The XPS data also show that C/O ratio increases in all the three reduction methods but the thermal reduction provides the highest value of 2.55 compared 1.94 with hydrazine vapors and 0.86 with ascorbic acid.

Chemical cross-linking using cations was performed in the GO films which were then thermally reduced. This was to investigate the effect of cations on inter-layer spacing in these films. Based on the XRD results, the cations had a limited effect in altering the inter-layer spacing in these films.

Chapter 4. Electrical Conductivity and Diffusion in Graphene Oxide Films

4.1 Objective of Chapter

Graphene, graphene oxide (GO) and reduced graphene oxide (rGO) membranes are being actively investigated for their diffusion properties. The research is driven by the potential for using these membranes in applications for desalination,[67] water purification,[60] and gas separation[74], and in a broader sense for diffusion control over different species. Typically these membranes consist of multilayer stacks of the graphene (or GO or rGO) sheets. The transport of molecular/ionic species in an aqueous medium across such a graphene membrane has been actively examined. [107,73,56,108,109,74] A defect-free single graphene sheet is impermeable to such ionic species. The transport of species across the graphene sheets is then accomplished by inducing pores in the sheets that are large enough to accommodate the ions.[73,67,56,108] Diffusion selectivity is based on the relative size of the pores and the solvated species, and their interactions.[74] Another means of controlling the permeation of the species is based on the inter-layer spacing between the graphene sheets in such a membrane.[69,68] Typically if the inter-sheet spacing is large enough, ionic species can easily diffuse across the membrane. The control over the inter-sheet spacing is hence a crucial parameter for modulating the diffusion characteristics of the graphene membranes. Here we have determined that membranes made with GO have a large inter-layer spacing due to the functional groups present on its surface. The inter-layer spacing can be modulated by reduction of these membranes. This is accomplished by a simple thermal treatment. The thermal reduction causes the removal of the functional groups and hence also decreases the inter-layer spacing.[110,111] The extent of reduction and the inter-layer spacing of the membranes depend on the temperature at which thermal reduction is performed. Further corresponding to the removal of the functional groups (or defects), the change in the

inter-layer spacing is also reflected in the electrical conductivity of these membranes. In this chapter the results from in-plane and out-of-plane electrical conductivity measurements of the films reduced at different temperatures are reported. Similarly, the ion diffusion characteristics of these films across aqueous medium is also presented. The effect of inter- layer spacing in these films which is modulated by the thermal reduction temperature, is correlated to the observed conductivity and diffusion behavior.

4.2 Current-Voltage Measurements of Graphene Oxide Films

In-plane (horizontal) and out-of-plane (vertical) conductivity tests on different thermal reduced membranes were performed by making silver contacts in the form of strips on the membranes using conductive silver paste (Electron Microscopy Sciences). Following this copper leads were connected from the silver strips on the film to the power supply and the multi-meter. In case of in-plane testing the spacing between the silver strips was maintained at 5 mm.

4.3 Results and Discussion on Electrical Conductivity

Graphene sheets with no defects have very high electrical conductivity due to their high electron mobility and zero band gap.[9] Graphene oxide on the other hand is an electrical insulator due to the high density of functional groups which act as defects and break the sp^2 hybridization of the carbon atoms in the lattice structure.[15] As GO is reduced, the removal of the functional groups leads to an increase in the electrical conductivity (though it never reaches the values observed for defect-free graphene).[76,112] In the case of the thermal treatment as observed above we should see a similar trend in the electrical conductivity of these membranes. In-plane and out-of-plane conductivity of the GO membranes were measured after thermal treatment at temperatures of 60 $^{\circ}$C, 180 $^{\circ}$C, 225 $^{\circ}$C and 250 $^{\circ}$C. The out-of-plane conductivity provides a direct measure of the change in the inter-layer spacing, whereas the in-plane conductivity depends on both the inherent conductivity of the GO and TrGO (Thermally reduced

graphene oxide) sheets and the overlap between the sheets. This occurs as the in-plane conductivity measurements are taken over a length scale of 3–10 mm and hence it requires the charge carriers to conduct both within the sheets and also between them to transverse across the two electrodes, as single GO sheets are ~ 0.5 microns thickness. Typically for such membranes the in-plane conductivity measurements are dominated by the charge transport characteristics of the graphene (or TrGO) sheets. Based on this, the in-plane conductivity of the GO and TrGO membranes thermally reduced at 60 °C, 180 °C, 225 °C and 250 °C is measured. As seen in Fig. 4.1, the in-plane conductivity increases by over 7 orders of magnitude between 60 °C and 250 °C. The in-plane conductivity in reduced GO sheets is based on the charge hopping model given by equation (4.1).[76] This is used to fit the current-voltage data (the solid line in Fig. 4.1) at the different temperatures used for thermal reduction.[76]

$$G = Y_o + G_o exp\left(\frac{V}{aL}\right) \quad \textbf{(4.1)}$$

Here V is the applied bias, L is the distance between the electrodes on the GO (TrGO) membrane over which the I-V measurements are conducted.[76]

$$a = \frac{kT}{0.18er} \quad \textbf{(4.2)}$$

k is the Boltzmann's constant; T is the temperature of the measurement; e is the absolute charge on electron and r is the hopping distance.[76]

The other critical parameter here is the G_o which depends on, N, the density of states near the Fermi level and L_l, the localization length of the electronic wave functions.[76]

$$G_o = G_1 exp\left(-\frac{B}{T^{1/3}}\right); B = \left(\frac{3}{KNL_l^2}\right)^{1/3} \quad \textbf{(4.3)}$$

As the temperature for thermal reduction is increased, the increase in conductivity can be illustrated from the reduction in the hopping distance, r, and the increase in the localization length of the electronic wave function. From the fitting of eq. (4.1), as seen in Fig. 4.2, the hopping distance reduces from ~ 4.5 nm at 60 °C to 1.6 nm at 250 °C. A steep reduction is observed between 180 °C and 225 °C, consistent with observations in the XRD and FT-IR results. Similarly, a significant increase in G_o is observed in going from 60 °C to 250 °C. The increase can be the combined effect of increase in the localization length, L_l, and the density of states, N.

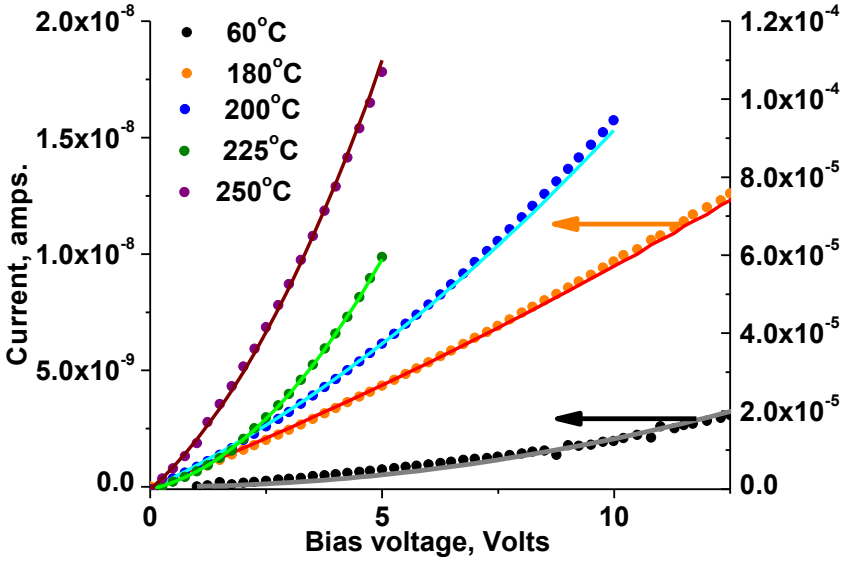

Fig. 4.1: I-V in-plane measurements of the electrical conductivity for the films. The points are the actual data and the solid line is the fit from equation (4.1).

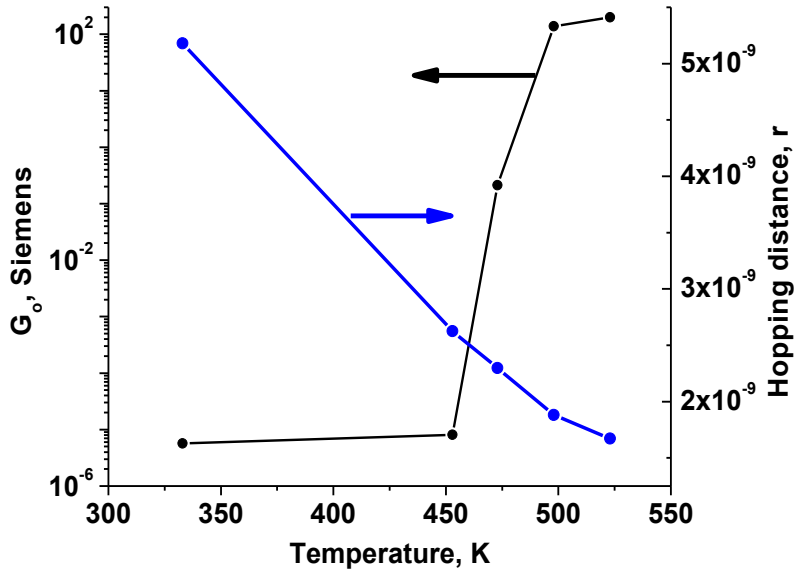

Fig. 4.2: I-V in-plane parameters.

The out-of-plane conduction in these membranes is over much shorter length scales, on the order of a few microns. This conduction, as can be seen in Fig. 4.3 shows a drastic increase as the thermal reduction temperature is increased from 60 °C to 250 °C. The charge conduction here can be considered as being governed by two aspects:[76,112] (a) the sheets have spacing between them and, given the high electric field strength tunneling is expected for the transport of the charge carriers across the sheets. (b) direct contact between the sheets also occurs as they are stacked into layers. This direct contact can be modelled as an ohmic resistance for charge transport. The combined equation fit to this model is:[77]

$$I = \frac{V}{R} + P_1 \times V^2 \times exp\left(-\frac{aE_c}{V}\right) \quad \textbf{(4.4)}$$

Here E_c is the critical field for tunneling, a can be considered as the length scale for the tunneling (this is considering that the term V/a is the effective electric field in the membrane), R is the ohmic resistance of the film due to contact between the TrGO sheets in the membrane.

The fit from eq. (4.4) to the data (the solid line in Fig. 4.3) is used to calculate the values of these parameters at the different thermal reduction temperatures, as seen in Fig. 4.4. We observe that R effectively reduces by over 6 orders of magnitude. The ohmic resistance can be considered to be dependent on the density of direct contacts between the TrGO sheets across the membrane thickness and on the ordered regions in the TrGO sheets that make up the membrane, since these will be the primary pathways for conduction. As the thermal reduction temperature is increased the removal of the functional groups will lead to an increase in the ordered regions in the sheets. Similarly, increased temperatures that lead to a reduction in the inter-layer spacing in these membranes will increase the density of the contact points between the sheets. The ~ 40% reduction in the inter-layer spacing will also decrease the path length for conduction of the charge carriers. But this will be a minor effect, as the ohmic resistance decreases linearly with the path length and hence cannot account for the 6 order decrease in this resistance. The decrease is therefore attributed to the increased inter-layer contact due to reduced inter-layer spacing and an increase in the ordered region (due to removal of the functional groups) on the TrGO sheets.

The factor aE_c combines the effective distance for tunneling (a) and the critical field for tunneling (E_c) and the effective dielectric of the material. E_c also depends on the effective Fermi level of the material. The increasing thermal reduction temperatures which lead to removal of the surface groups in the GO sheets and also decrease the inter-layer spacing in the TrGO membrane should cause a decrease in 'a'. This can be observed in Fig. 4.4. The decrease in

aE_c, which is around 16 times, is much greater than the decrease in the inter-layer spacing as quantified by XRD. The initial drastic decrease in the aE_c between 60 °C and 180 °C is the result of the removal of water which alters the effective dielectric constant of the membrane. Following this the gradual decrease from 180 °C to 250 °C is the result of the reducing interlayer spacing and the effective increase in the Fermi level of the GO sheets on reduction that leads to a decrease in E_c.

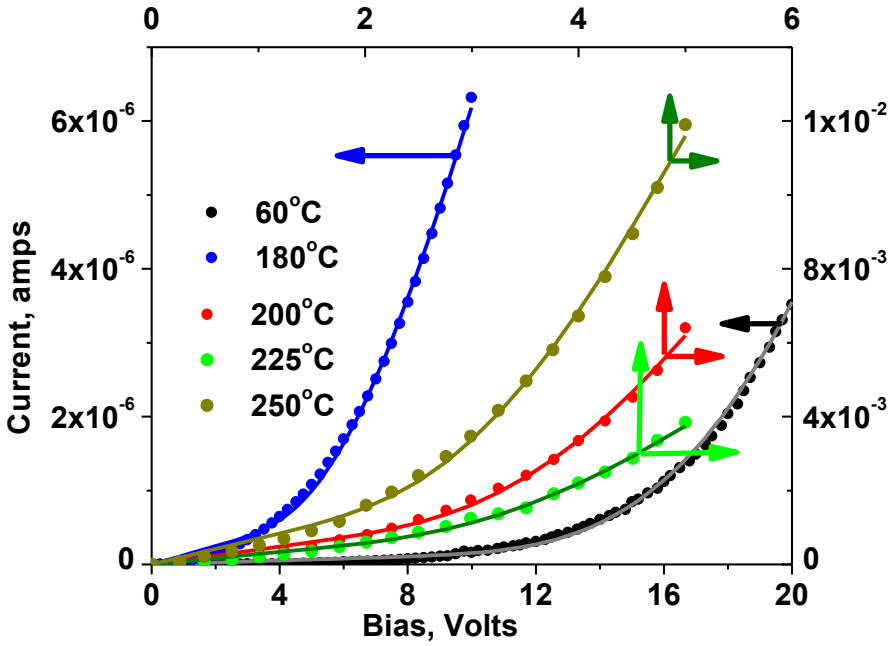

Fig. 4.3: I-V out-of-plane measurements of the electrical conductivity for the films. The points are the actual data and the solid line is the fit from equation (4.4).

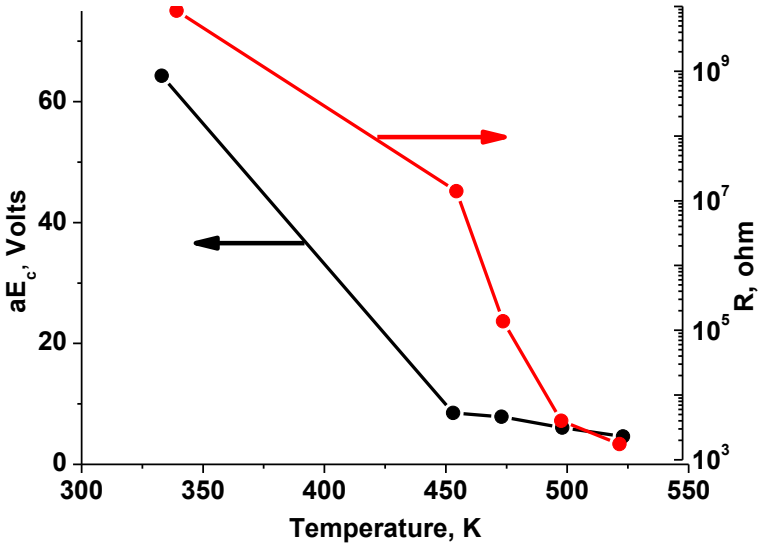

Fig. 4.4: I-V out-of-plane parameters.

4.4 Diffusion Test in Graphene Oxide Films

Diffusion characteristics of the TrGO membranes were tested in a home build set-up. It consisted of two reservoirs that were separated by placing the TrGO membrane in between. One of the reservoirs was filled with Millipore water (Ultrapure water > 18MΩ) and the other with appropriate salt solution. The conductivity of the MilliQ water was tested periodically to measure the increase in its salt concentration due to diffusion across the TrGO membrane.

4.5 Diffusion Model for Graphene Oxide Films

The diffusion across the membrane separating two stationary reservoirs of fluids can be modelled as shown in Fig. 4.5.

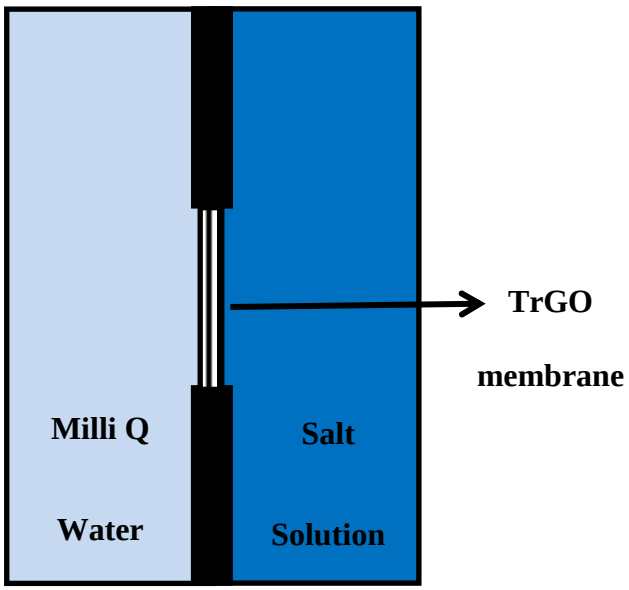

Fig. 4.5: Schematic diffusion cell.

The diffusional problem can be solved in 1-D using Fick's second law:[113]

$$\frac{\partial C}{\partial t} = P\frac{\partial^2 C}{\partial x^2} \qquad \textbf{(4.5)}$$

Where P is the effective diffusional resistance that includes the characteristics of the TrGO membrane and the ion characteristics.

The solution to this differential equation is given by:

$$C = \frac{1}{2}C_o erfc\left(\frac{x}{2\sqrt{Pt}}\right) \qquad \textbf{(4.6)}$$

Where C_o is the initial concentration of the salt solution.

The model assumes both the reservoirs to be of identical volume. Hence the final concentration is $C_o\ /2$.

The salt concentration of the Millipore water can be calculated as a function of time from the net amount of salt transfer across the TrGO film.

$$S_t = \int_0^t J_o . A . dt \quad \textbf{(4.7)}$$

Here J_o is the instantaneous diffusional flux across the membrane and A is the cross-sectional area of the membrane.

J_o is given by:

$$J_o = -P \frac{\partial C}{\partial x}\Big|_{x=0} \quad \textbf{(4.8)}$$

Solving this it is established that the net amount of salt transferred S_t is:

$$S_t \propto t^{1/2} \quad \textbf{(4.9)}$$

Where the proportionality constant will be dependent on the exact experimental conditions and the resistance of the membrane. For identical experimental set-up if only the membrane is changed then the changes in the proportionality constant should reflect the changes in the characteristics of the membrane.

Typical fits for diffusion of 100 mM NaCl across a TrGO membrane processed at 60 °C (Fig.4.6) and at 180 °C (Fig. 4.7), show that the basic evolution of the diffusion is captured by this equation.

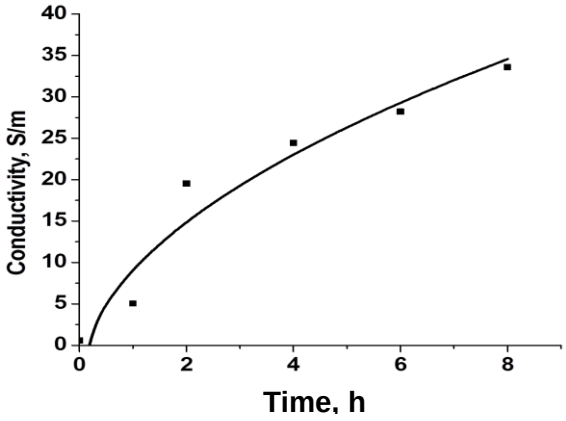

Fig. 4.6: Diffusion of 100 mM NaCl through GO film reduced at 60 °C, and the fit based on theoretical model.

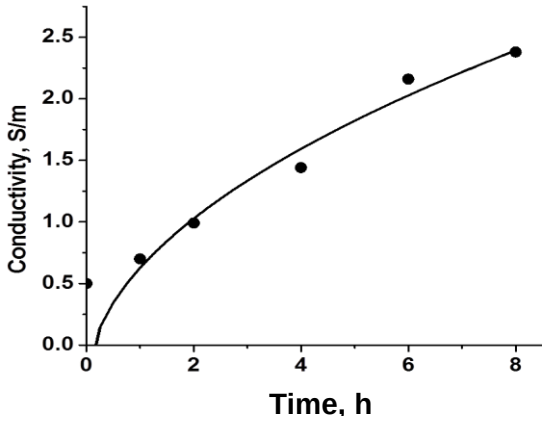

Fig. 4.7: Diffusion of 100 mM NaCl through GO film reduced at 180 °C, and the fit based on theoretical model.

Similarly the fits for diffusion of 100 mM $CaCl_2$ across the TrGO membrane processed at 60 °C and 180 °C are shown in Fig. 4.8 and Fig. 4.9.

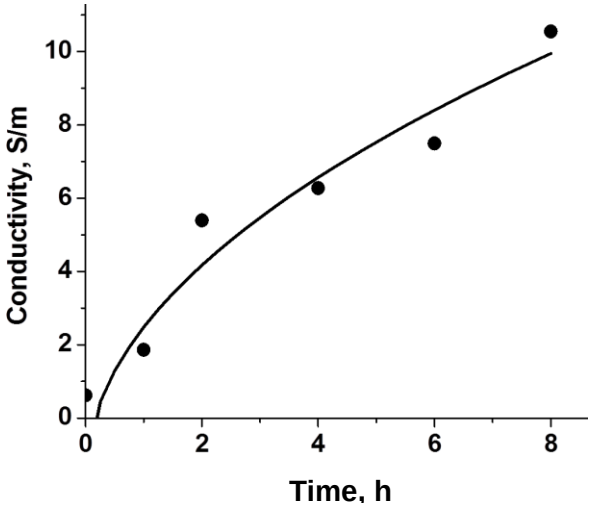

Fig. 4.8: Diffusion of 100 mM $CaCl_2$ through GO film reduced at 60 °C, and the fit based on theoretical model.

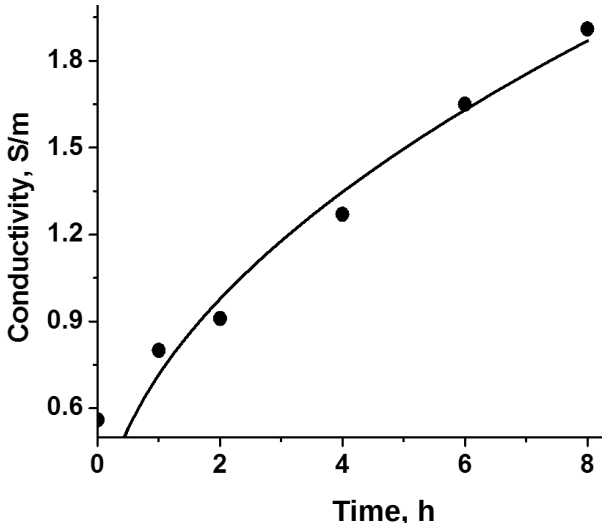

Fig. 4.9: Diffusion of 100 mM $CaCl_2$ through GO film reduced at 180 °C, and the fit based on theoretical model.

From these fits, the proportionality constant can be calculated and the diffusional characteristics of the different TrGO membranes can be compared. Effectively we are able to observe that with increasing thermal reduction temperatures the diffusional resistance of the TrGO films increases significantly.

4.6 Results and Discussion on Diffusion:

The diffusion of ions in a salt solution through graphene membranes is an actively researched topic. The ability of the ions to diffuse across the graphene membrane is affected both by the free volume in the membrane and the presence of functional groups.[56,74,73,56,110] The free volume that will depend on the inter-layer spacing, similar to the filtration and osmosis membranes determines the ability of the ions to permeate across these membranes. At the same time, the functional groups that lead to hydrophilic characteristics in the membrane also affect the ability of these ions to diffuse across it, since water is the fluid medium and the ions

are charged.[55] Based on the change in the inter-layer spacing and the functionalization of these membranes upon thermal treatment, we expect that this method can be used to control their ion diffusion characteristics. The diffusional characteristics of these membranes were studied by using them as separators between two chambers. One of the chambers was filled with a salt solution (100 mM $CaCl_2$ or 100 mM NaCl), and the other chamber contained Millipore water (18 MΩ.Cm resistivity). The increase in the conductivity of the Millipore water resulting from diffusion of the ions across the GO and TrGO membranes was monitored. The increase in conductivity is directly proportional to the net amount of ions that cross into the Millipore water. The increase can be modelled (see Fig. 4.11) to be proportional to $t^{1/2}$ (the elapsed time) and to the diffusional resistance of the membrane. Fig. 4.10 represents the observed increase in the conductivity of the Millipore water (for 100 mM NaCl). From the fit shown with the solid line in Fig. 4.10, the effective diffusional resistance of the different TrGO membranes processed at different temperatures was calculated, and the plot is shown in Fig. 4.11. We observe that the diffusional resistance increases rapidly above 180 $^{\circ}$C, in agreement with the rapid reduction in the inter-layer spacing and the removal of functional groups above those temperatures. The trend in the case of 100 mM $CaCl_2$ was identical, that a difference in the relative change in the membrane resistance was observed. For NaCl, the change was more dramatic than for $CaCl_2$. This is due to the higher initial diffusion rate for the monovalent ion Na^+, which is consistent with its smaller size compared to Ca^{2+}.[114] From these results, it can be seen that GO films treated at 60 $^{\circ}$C have better selectivity towards the Na^+ and Ca^{2+} ions and this selectivity decreases due to loss of permeation of the Na^+ ions predominately. The treatment at 180 $^{\circ}$C leads to a decrease in the diffusion rate of Na^+ more than one order magnitude, while the diffusion rate of Ca^{2+} is roughly halved. The exposure area for both the GO film and the filtration paper (Whatman quantitative filter paper, Grade 40, diameter 125 mm, pore size 8 µm, thickness 210 µm) was 6 mm. Because of the greater thickness of the filtration paper (210 µm) compared to the GO film (3.74 µm), the diffusion through the filtration paper still takes a longer time. The GO film reduced

at 250 °C has the lowest ionic conductivity due to the fact that most of the oxygen functional groups have been eliminated; hence no interaction takes place between the functional groups and the ions. The ability to control the diffusional characteristics of the GO membrane by thermal treatment and the temperature of exposure illustrate a simple method to tailor the properties of these membranes. Further, this can also be expanded to include the effect on diffusion of small organic molecules and also selective permeation of gases.

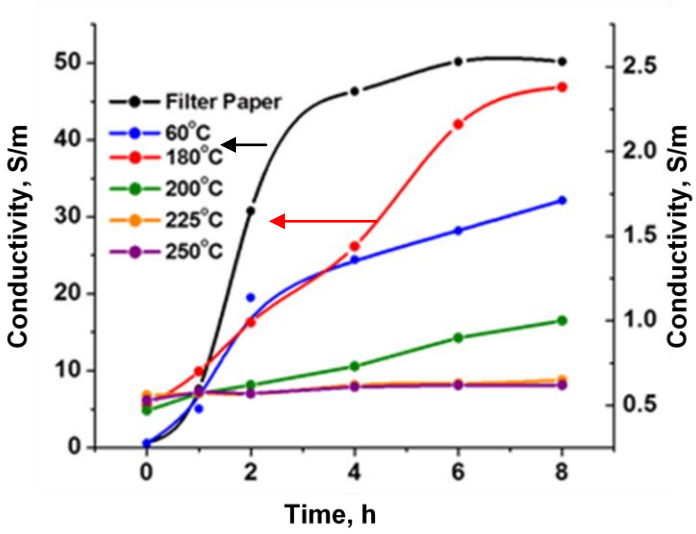

Fig. 4.10: Diffusion of 100 mM NaCl through GO films reduced at different temperatures.

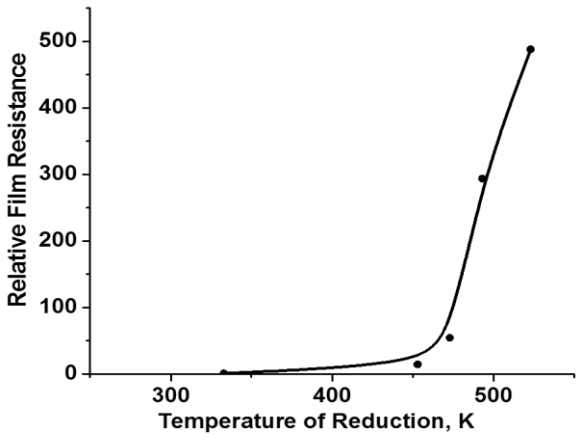

Fig. 4.11: Diffusional resistance of GO films reduced at different temperatures relative to GO film reduced at 60 °C for NaCl.

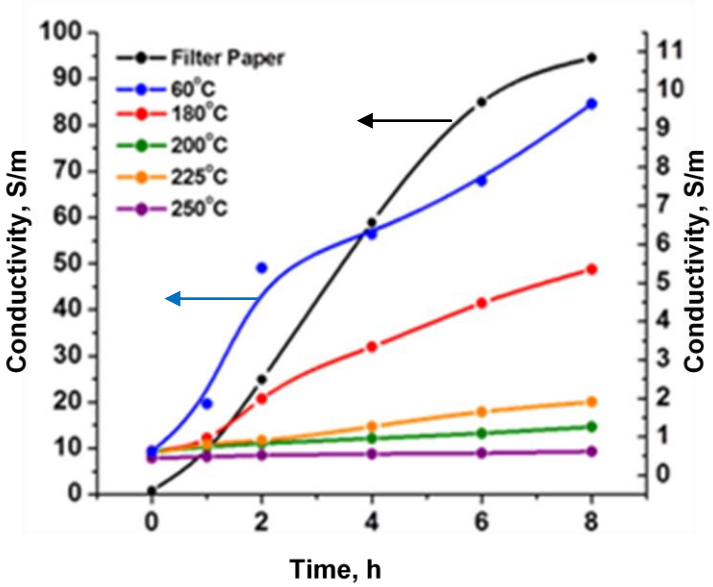

Fig. 4.12: Diffusion of 100 mM $CaCl_2$ through GO films reduced at different temperatures.

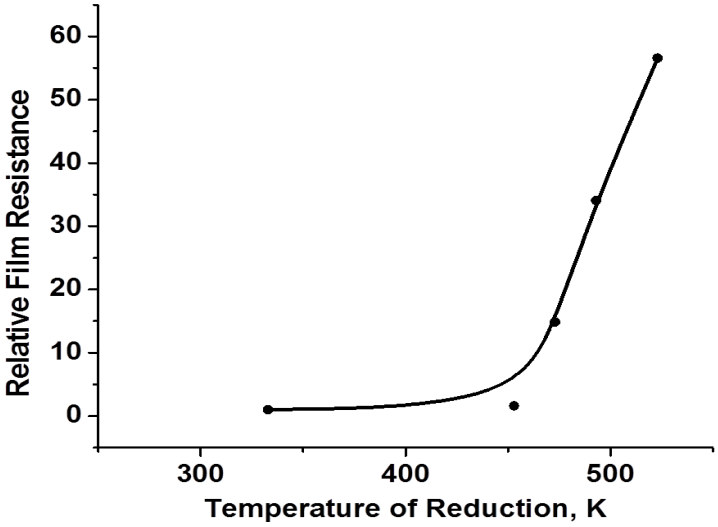

Fig. 4.13: Diffusional resistance of GO films reduced at different temperatures relative to GO film reduced at 60 °C for $CaCl_2$.

4.7 Conclusions for Chapter Four

In-plane and out-of-plane electrical conductivity measurements of the GO films reduced at different temperatures are reported. Similarly, the ion diffusion characteristics of these films across aqueous medium is also presented. The effect of inter- layer spacing in these films which is modulated by temperature of thermal reduction temperature, is correlated to the observed conductivity and diffusion behavior. The out-of-plane conductivity provides a direct measure of the change in the inter-layer spacing, whereas the in-plane conductivity depends on both the inherent conductivity of the GO (and TrGO) sheets and the overlap between the sheets. The in-plane conductivity increases by over 7 orders of magnitude on increasing the reduction temperature from 60 $^{\circ}$C to 250 $^{\circ}$C. The in-plane conductivity in reduced GO sheets is based on the charge hopping model. The increase in the conductivity signifies that the structural defects are reduced and more sp^2 regions are introduced in these films on thermal reduction due to removal of the oxygen-containing functional groups. The out-of-plane conduction in these membranes is over much shorter length scales. This conduction shows a drastic increase as the thermal reduction temperature is increased from 60 $^{\circ}$C to 250 $^{\circ}$C. The charge conduction can be considered as being governed by two aspects (1) the sheets have spacing between them and, given the high electric field strength tunneling is expected for the transport of the charge carriers across the sheets. (2) direct contact between the sheets also occurs as they are stacked into layers. This direct contact can be modelled as an ohmic resistance for charge transport. The increase in conductivity results from the reduced inter-layer spacing which increases both direct contact between the sheets and the density of ordered regions in the films and also reduces the distance for tunneling.

The diffusional characteristics of these membranes were studied by using them as separators between two chambers, one filled with salt solution and the other with Millipore water. The ability of the ions to diffuse across the graphene membrane is affected both by the

free volume in the membrane and the presence of functional groups. Thermal reduction affects both these parameters as its reduces the inter-layer spacing and removes the oxygen-containing functional groups. The temperature of reduction is again crucial as the diffusional resistance of the films increases drastically above temperatures of 200 $^{\circ}$C, consistent with the observation made with XRD and TGA. Further the extent of increase in diffusional resistance also depends on the size of ion that has to diffuse across these films. Larger ions show a more drastic change as they require a larger free volume in the films to diffuse.

Chapter 5. Future Work for Thermally Treated Graphene Oxide Films

In the course of our work with rGO films, promising preliminary results in other areas of applications were also obtained. These results lay the ground for future research for more in depth analysis. These initial studies didn't necessitate expansive treatment in main chapters of this thesis, and are collectively treated as future work. This chapter provides an account of our entry into these areas, and points to the logical outgrowths of our findings as the basis for work by future researchers. This future work will entail basic research, but in each case is directed toward practical applications. The topics covered in this chapter include: NaCl filtration through TrGO films under vacuum; the influence of applied voltage on the diffusion of $CaCl_2$ across TrGO films; TrGO-supported photocatalytic degradation of a model organic pollutant; and, TrGO-based electrochemical capacitors. The first two subjects have a strong introductory basis in the earlier chapters of this work, but the latter two—photocatalysis and electrochemical capacitors—will require detailed introduction in their respective sections.

5.1 Ionic Conductivities Measurements Through Vacuum Filtration

5.1.1 Experimental Method, Results and Discussion

In this experiment 5 mL of 100 mM NaCl was filtered through the various GO membranes and the ionic conductivity of the filtrate was measured. The purpose of this measurement is to investigate if there is a difference in the ionic conductivities between the 100 mM NaCl (13.76 mS/cm) and the filtrate solution through different GO films which would show the potential of GO film in desalination process as another approach for water purification. Our results are shown in the schematic diagram Fig. 5.1, and they can be illustrated based on two different effects.

1. Effect of the thickness of the GO film which can be represented in the following samples red. 1.25GO, red. 1.5GO, and red. 2GO films, all of which were reduced at 250 °C. The measurements of the ionic conductivities are 12.5, 11.9, and 11.3 mS/cm, respectively. It can be clearly seen that the lowest thicknesses, 1.25GO, has the higher ionic conductivity, 12.5 mS/cm, compared to the rest.

2. Effect of the thermal treatment which can be shown in the following samples non-reduced 1.25GO, red. 1.25GO at 250 °C and red. 1.25GO at 300 °C; their respective ionic conductivities are 13.76 mS/cm, 12.5, and 11.2 mS/cm; their respective d-spacings are 7.36 Å, 4.59 Å, and 4.57 Å . The difference in the d-spacing which results from the heat treatment would hinder the passage of salts ions leading to their rejection during filtration.

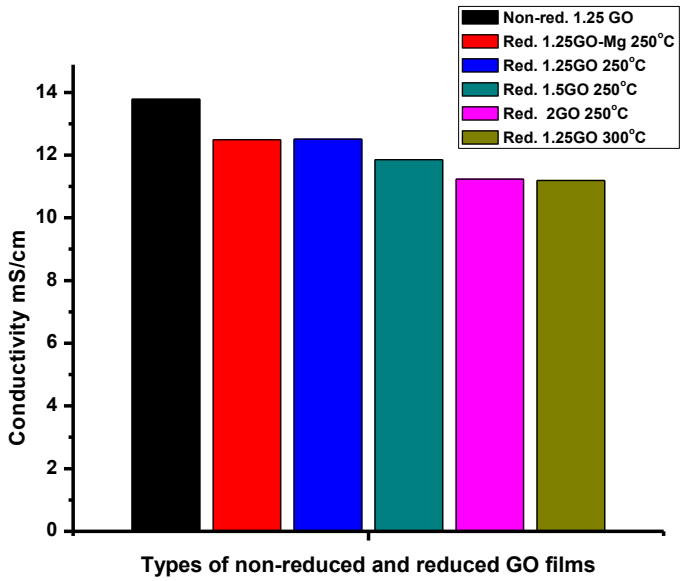

Fig. 5.1: Ionic conductivities measurements of 100 mM NaCl through vacuum filtration of different GO films.

5.1.2 Conclusion and Future Work

Our results indicate that the GO films have the ability to hinder the ions of salt solutions filtered under applied force. This could have implications for the suitability of these materials in industrial or other practically-scaled desalination processes. Our results indicate that reduced d-spacing and increased film thickness lead to a greater salt rejection. Development of this experiment-scaled technology toward practically deployed desalination will require achieving maximal solute retention. Future work will have to focus on further optimization in this area; moreover, commercialization or industrialization requires scale and durability. Future work will have to determine means of depositing larger films. At the laboratory scale, later researchers could test new porous support media that would remain attached to deposited GO films, and are able to survive both the conditions of reduction to rGO and prolonged use, increasing the strength and durability of the graphitic material. In addition, this modification could be coupled to metal ion cross-linking within the film, which would be examined for its possible further influence on film strength, as well as its influence on ion passage.

5.2 Applying Surface Potential on GO Membranes During Diffusion Process

Surface potential was applied to non-reduced GO film (60 $^{\circ}$C) and reduced GO film (180 $^{\circ}$C). The objective of this study is to investigate the influence of the applied voltage to the films on the diffusion of 100 mM $CaCl_2$. The diffusion cell as well as the set up for applying surface potential on the reduced films are depicted in Fig. 5.2. The results are shown in table 5.1. Two different films were used before and after applying potential for each of the non-reduced GO film (60 $^{\circ}$C) and reduced GO film (180 $^{\circ}$C).

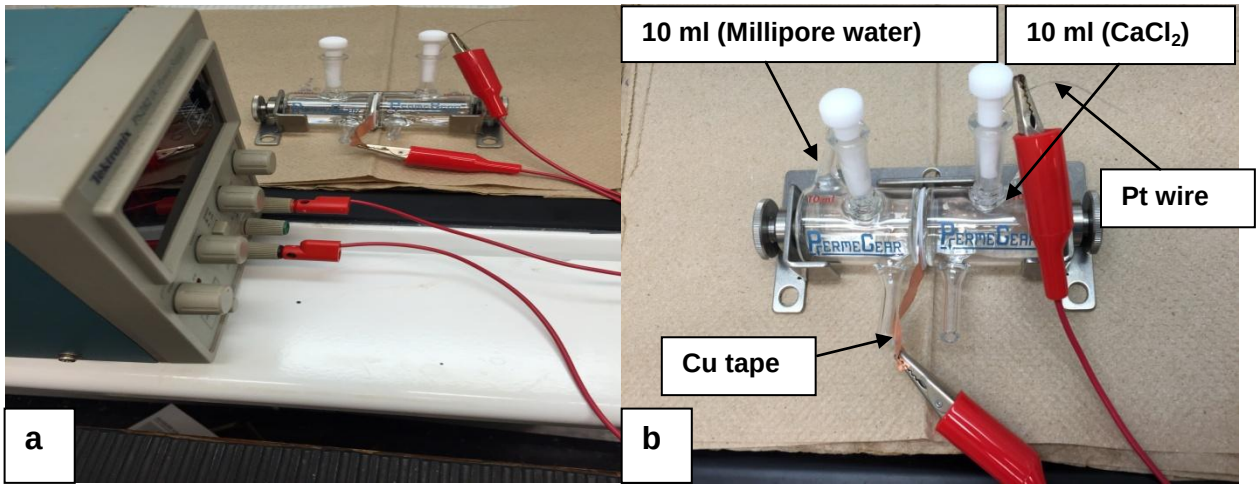

Fig. 5.2: (a) Applying surface potential on the GO film. (b) Diffusion cell.

The first trend is without applying voltage: The ionic conductivity of Millipore water when using the non-reduced GO 60 °C increased from 6.31 µS/cm (after one hour) to 41.1 µS/cm overnight, which is an indication that of diffusion occurring across the film. In contrast, when a potential is applied to the surface of the GO film, the increase in ionic conductivity overnight was limited to 5.57 µS/cm. The ionic conductivity of the reduced GO 180 °C without applying voltage was 5.12 µS/cm and showed little variation even after three hours (7.67 µS/cm), which indicates that very limited diffusion takes place due to the effect of smaller d-spacing of the reduced GO film compared to the non-reduced GO. However, on applying a surface potential to this film, the ionic conductivity decreased from 4.76 to 0.62 µS/cm in three hours. More experiments are required to ascertain the cause of this effect and we believe it may be due to the accumulation of compensating ions on the film surface in response to the applied potential, which may stop the normal diffusion process. The reversal of the diffusion process will need to be thoroughly investigated in terms of the surface concentration of the ions on the film.

Table 5.1: Measurements of filtrate conductivities over different reduced GO films with and without application of surface potential.

Type of GO film	Time	Conductivity (µS/cm) Without applying voltage	Conductivity (µS/cm) With applying voltage
GO 60 °C	After 1 h	6.31	10.95
	After 2 h	8.75	6.60
	After 3 h	7.93	7.25
	After 5 h	9.65	7.79
	Overnight	41.1	5.57
GO 180 °C	After 1 h	5.12	4.76
	After 2 h	5.86	4.65
	After 3 h	7.67	0.62

5.2.1 Conclusion and Future Work

Our results show the crucial role of applying voltage on the surface of the GO films, in which ions can accumulate on the surface of the GO films and hinder the diffusion, and this can be used in desalination to obtain pure water. For instance, if the voltage was positive, the negative ions would accumulate on the film surface thus hindering the diffusion and vice versa. Research focused on the optimization of the applied voltage, and its variation with time, needs to be performed to further understand its effect on ion diffusion across these membranes. As a future work, we would utilize the reduced GO films at 200 °C, 225 °C, 250 °C. Since these films reduced at higher thermal reduction temperatures have smaller inter-layer spacing, the combination of this feature with the applied voltage on their surface might be anticipated to further hinder ion passage. Moreover, the GO cross-linkers via metal ions could also be utilized in these experiments, to determine the combined influence of cross-linkers and applied voltage on ion passage.

5.3 Photocatalysis with Metal Oxide Nanostructures on GO Membranes

5.3.1 Introduction of Photocatalysis with Semiconductor Metal Oxides

Semiconductors are used and researched for their application as photocatalysts for solving environmental problems such as waste water purification. Studies on heterogeneous photocatalysis began prior to the 1970s;[115] however, a particular interest in the field took place right after the milestone by Fujishima and Honda in 1972 on the discovery that water could be split into hydrogen and oxygen over single crystal TiO_2 (rutile) in a photoelectrochemical (PEC) cell.[116] This observation had opened an alternative approach on the production of hydrogen as a combustible fuel.[115] The mechanism of heterogeneous photocatalysis is well-understood. In brief, upon absorption of photons whose energy is equal or higher than the band gap of a photocatalyst (e.g. TiO_2, ZnO), electrons will be promoted from the valence band to the conduction band, leaving holes behind.[117] Electron-hole (e^--h^+) pairs are generated. These surface holes and electrons can oxidize and reduce surface-adsorbed molecules respectively.[115] The photocatalytic reactions involve radicals or highly reactive species such as $^{\cdot}OH, ^{\cdot}O^{2-}$. The organic molecules that exist around the surface of the photocatalysts can be attacked by these reactive species since they are powerful oxidizing agents.[118] Fig. 5.3 depicts photoexcitation of a semiconductor.

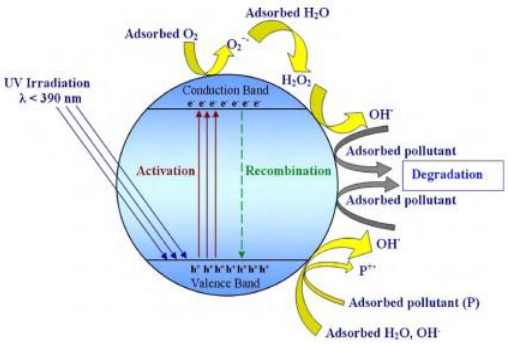

Fig. 5.3: Photoexcitation of a semiconductor (taken from ref.[118] with permission from Elsevier).

Due to the significant properties of TiO_2 such as high removal efficiency, cost-effectiveness, chemical stability, and low toxicity,[119,120,121] it is the most commonly used as a photocatalyst in water purification. It has the ability to decompose organic pollutants such as organic dyes into carbon dioxide and water.[120,121] TiO_2 has relatively high band-gap energy (3.2 eV), and the photocatalysis can be ascribed to the electron-hole pairs which can be activated via UV light.[122] In fact, TiO_2 possess three different phases, namely anatase, rutile, and brookite.[123] Anatase and rutile are the most studied phases.[124,125,126] The difference in the crystal structure is shown in Fig. 5.4:

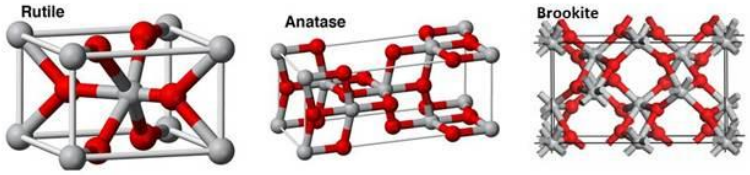

Fig. 5.4: The three different phases of TiO_2 (taken from ref.[127] with permission from Elsevier).

Zinc oxide (ZnO) is another semiconductor that has been used as a photocatalyst. It has a wide band gap (3.37 eV), and is abundant, nontoxic, inexpensive, and environmental friendly.[128] ZnO exists either in cubic rocksalt, cubic zinc blende or hexagonal wurtzite crystal structures.[129] Its crystal structures are shown in Fig. 5.5:

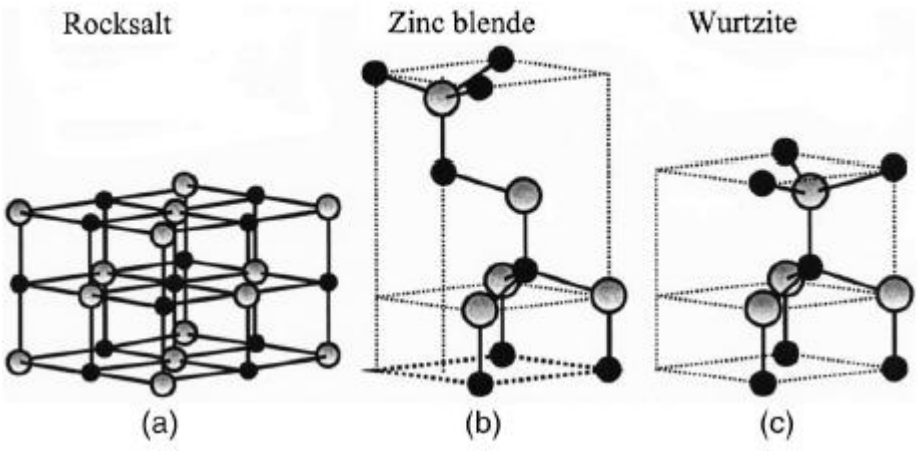

Fig. 5.5: Stick and ball representation of ZnO crystal structures: (a) Cubic rocksalt, (b) Cubic zinc blende, and (c) hexagonal wurtzite. The shaded grey and black spheres denote Zn and O atoms, respectively (taken from ref.[129] with permission from Journal of Applied Physics).

Despite the intense research that has been conducted on graphene-TiO_2, GO-TiO_2, and GO-ZnO composites, it is still a challenge to further enhance their photoactivity under UV irradiation. To gain a better understanding of the effect of the morphology of the ZnO and graphene composite, we have investigated comparison between ZnO nanorods, GO-ZnO composite, and GO-ZnO film on the performance of the photocatalytic degradation of MB.

5.3.2 Hydrothermal Synthesis of ZnO Nanorods on GO Films

Zinc oxide (ZnO) nanorods were synthesized on GO films in two steps, the first one is a seed layer deposition on GO films, and this is followed by hydrothermal growth of ZnO nanorods on the GO film.[130] Firstly, seed layer deposition is achieved by a solution of 7 mM of zinc acetate [$Zn(CH_3COO)_2.2H_2O$] in ethanol was dropped on GO film several times and allowed to dry, then the film was heated at 350 $^{\circ}$C for 30 minutes. Second, hydrothermal growth, a mixture of 15mM equi-molar solution of zinc nitrate hexahydrate [$Zn(NO_3)_2{\cdot}6H_2O$] and hexamethylenetetramine (HMT, $C_6H_{12}N_4$), were placed in a silicon oil bath. Once the temperature of the solution reached to 85–90 $^{\circ}$C, the GO film was placed upside-down in the

solution for two hours. [131] Hydrothermal growth of ZnO nanorods is shown in Fig. 5.6. FESEM image of growth of ZnO nanorods on GO film is shown in Fig. 5.7.

Fig. 5.6: Hydrothermal growth of ZnO nanorods.

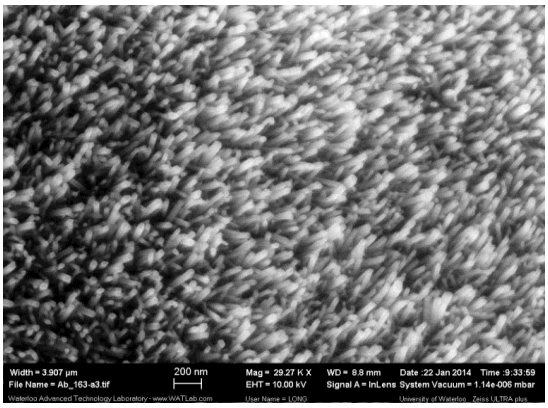

Fig. 5.7: SEM growth of ZnO nanorods on GO film.

A proposed growth mechanism

Thermodynamically, at ambient conditions, wurtzite crystal structure is the most stable form for ZnO. Among the growth mechanisms, which have been proposed for deposition in aqueous chemical solution, is the Ostwald ripening process.[132] It relies on both kinetic and thermodynamic influence. Nucleation would first start with tiny crystallites, after which the large particles would grow. In the solution, the reaction between zinc nitrate and hexamethylenetetramine (HMT, $C_6H_{12}N_4$) will produce the following chemical reactions:[131]

$$Zn(NO_3)_2 \rightarrow Zn^{2+} + 2NO_3^- \quad \textbf{5.1}$$

$$(CH_2)_6N_4 + 6H_2O \rightarrow 6HCHO + 4NH_3 \quad \textbf{5.2}$$

$$NH_4OH \leftrightarrow NH_3 + H_2O \quad \textbf{5.3}$$

$$Zn^{2+} + 4NH_3 \rightarrow Zn[(NH_3)_4]^{2+} \quad \textbf{5.4}$$

$$2H_2O \leftrightarrow H_3O^+ + OH^- \quad \textbf{5.5}$$

$$Zn^{2+} + 2OH^- \leftrightarrow Zn(OH)_2 \quad \textbf{5.6}$$

$$Zn(OH)_2 \rightarrow ZnO + H_2O \quad \textbf{5.7}$$

Equations (1) and (2) show just the hydrolysis of zinc nitrate hexahydrate and HMT respectively. Equation (6) is of significance in which the colloidal $Zn(OH)_2$ would play a crucial part for the growth of ZnO nanorods. As the temperature increases, the $Zn(OH)_2$ will dissolve more during the hydrothermal growth process. Nucleation starts when the solution is supersaturated in which the critical value is reached between the concentration of Zn^{2+} and OH^-.[131] The growth will be along the +c-axis (0001) direction since the higher symmetry (C_{6v}) exists in the (001) face.[129]

5.3.3 Synthesis of GO-ZnO Composite

An appropriate amount of GO was dissolved in Millipore water under sonication for an hour. Then an appropriate amount of ZnO nanoparticles colloidal was added into GO solution and the mixture was further sonicated for 70 minutes. After that the solution was stirred for 2 hours, then it was washed, and centrifuged several times with ethanol, and finally dried.

5.3.4 Comparison between ZnO Nanorods, GO-ZnO Film, and GO-ZnO Composite

Three samples listed in table 5.2 were prepared for comparing their ability to degrade methylene blue (MB). For each experiment, an appropriate amount of sample was placed in a 50 mL beaker and added in 14 mL of aqueous 10 ppm methylene blue (MB) and the mixture was stirred magnetically in the dark for 30 minutes to allow for adsorption equilibration. The mixture was then illuminated with UV light and 2 mL aliquots were periodically removed, centrifuged, and the supernatant was subjected to UV spectroscopy to monitor MB degradation.

Table 5.2: The prepared samples for degradation of methylene blue (MB).

Type of sample
ZnO nanorods dispersed in C_2H_5OH (ZnO/ C_2H_5OH)
GO-ZnO film
GO-ZnO composite

5.3.5 Results and Discussion

The best efficiency for the degradation of aqueous MB is obtained when the material exists in a colloidal phase and in presence of an assisting material whose energy band position is higher than the valence band of the semiconductor metal oxide, so that the charge recombination between electrons and holes would be hampered, which would lead to the enhancement of the degradation.

Our results show that the highest efficiency is achieved with sample GO-ZnO composite, where in 9 hours complete degradation of MB was observed. The rGO played an important role in hindering the fast recombination between electrons and holes which leads to increased efficiency in the degradation of MB as shown in the schematic diagram Fig. 5.9. There may also be a contribution to the reduction of MB by just rGO, which requires further investigation.[133] The environment around the ZnO nanorods also plays a significant role towards the performance of the photocatalytic degradation of the organic pollutants. Since ZnO nanorods were dispersed in ethanol, it showed a reasonable degradation.

The nature of the material has a crucial significance in the efficient activity of the photocatalytic activity of the metal oxide. For instance, GO-ZnO film was growth of ZnO nanorods on graphene oxide that was reduced at 250 $^{\circ}$C. Fig. 5.8 represents the degradation percentage of the samples ZnO/ C_2H_5OH, GO-ZnO film, and GO-ZnO composite. The sample GO-ZnO composite degraded 85% of the dye solution in 6 hours, in contrast to the sample GO-ZnO film, which degraded 19% in the same period of the time. The ZnO/ C_2H_5OH degraded 47% of the dye solution. As mentioned earlier, GO has a potential role in enhancing the performance of the photocatalytic degradation of organic pollutants. The degradation percentage is calculated as follows:

$$[\text{Degradation \%} = (1 - \frac{A}{A_\circ}) * 100]^{134} \quad \textbf{(5.8)}$$

where $A_\circ$ and A are the absorbance maxima of MB before and after an irradiation time, respectively.

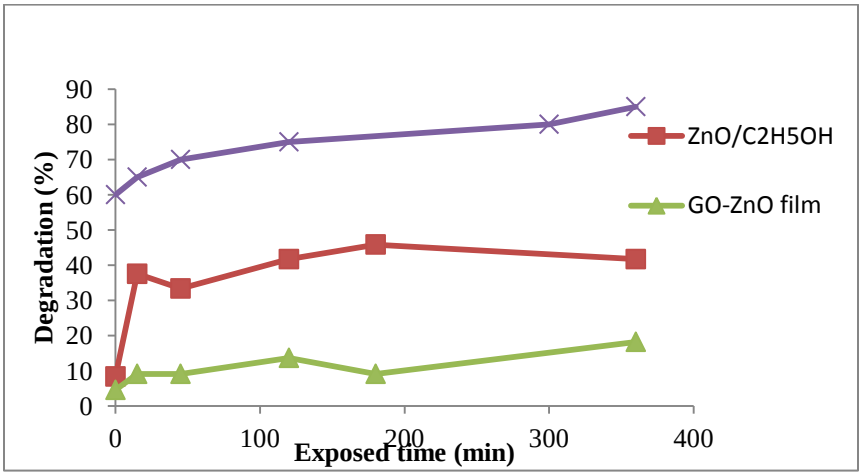

Fig. 5.8: Degradation percentage of the samples ZnO/ C_2H_5OH, GO-ZnO film, and GO-ZnO composite

A proposed series of reactions in the degradation of MB as follows:[135]

$$ZnO + h\nu(UV) \rightarrow ZnO(h_{vb}^{+}) + ZnO(e_{cb}^{-}) \quad \textbf{5.9}$$

$$ZnO(h_{vb}^{+}) + H_2O \rightarrow H^{+} + ZnO(^{\cdot}OH) \quad \textbf{5.10}$$

$$ZnO(e_{cb}^{-}) + O_2 \rightarrow ZnO(O_2^{-\cdot}) \quad \textbf{5.11}$$

$$ZnO(O_2^{-\cdot}) + H^{+} \rightarrow HO_2 \quad \textbf{5.12}$$

$$2HO_2 \rightarrow H_2O_2 + O_2 \quad \textbf{5.13}$$

$$H_2O_2 + ZnO(e_{cb}^{-}) \rightarrow ZnO(^{\cdot}OH) + OH^{-} \quad \textbf{5.14}$$

$$ZnO(^{\cdot}OH) + MB \rightarrow \text{deg}\,radation + ZnO \quad \textbf{5.15}$$

$$ZnO(O_2^{-\cdot}) + MB \rightarrow \text{deg}\,radation + ZnO \quad \textbf{5.16}$$

The photocatalytic activity of ZnO commences upon irradiation with UV light, which creates electron-hole pairs (eq.1) by the excitation of electrons from the valence band to the conduction band, leaving holes behind (h_{vb}^{+}). These holes react with water to form hydroxyl radical $(\cdot OH)$ (eq.2), while superoxide radicals $(O_2^{-\cdot})$ are produced by oxygen molecules on accepting the excited electrons (eq.3). Most important is the enhancement of the photocatalytic activity of the ZnO by hampering the recombination of electrons with their holes via transferring electrons from ZnO to graphene oxide as it can be seen in the energy band positions Fig. 5.9, which creates more superoxide and hydroxyl radicals. These hydroxyl and superoxide radicals react with the MB to form degradation products as in the following equation:[135]

$$ZnO + MB \xrightarrow{h\nu(UV)} CO_2 + H_2O + NO_3 + NH_4^{+} + SO_4^{2-} + ZnO \qquad \textbf{(5.17)}$$

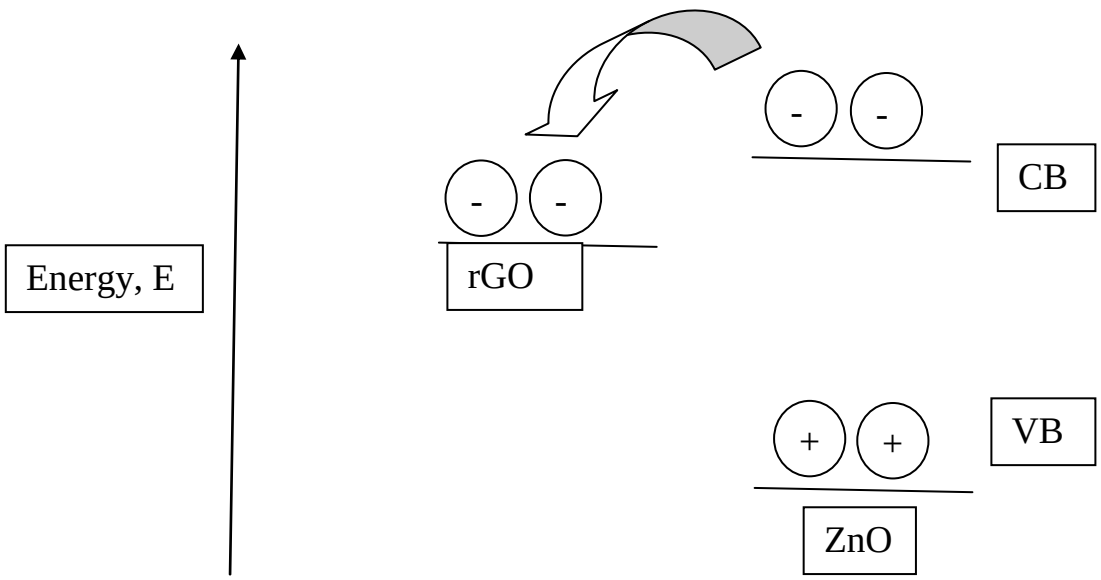

Fig. 5.9: Schematic diagram of energy levels in GO-ZnO composite.[136]

5.3.6 Conclusion and Future Work

Our results indicate that the colloidal sample GO-ZnO composite has better performance in degradation of MB than the GO-ZnO film and just ZnO colloidal in ethanol. In the sample of GO-ZnO film, the ZnO nanorods grew perpendicular on the GO film. Despite the fact that the GO-ZnO film showed the lowest degradation percentage of MB, it could be used several times in a succession of pollutant solutions by simply taking it out and transferring it to the next solution. In contrast, for colloidal solutions, at every stage there has to be a purification and separation step.

We have previously established that ZnO nanorods can be grown in a horizontal orientation in which they are parallel to the surface of GO film. We have not yet investigated the efficiency of these preparations in degradation of MB, and this represents obvious future work. ZnO nanorods grown parallel to the GO film is shown in the following Fig. 5.10. In addition, later workers should systematically examine varying relative concentrations of GO and ZnO with respect to MB degradation. It also may be beneficial to explore hybrid composite preparations in which GO-ZnO is combined with GO-TiO_2, as titanium dioxide has precedent as a photocatalyst for organic pollutant degradation.

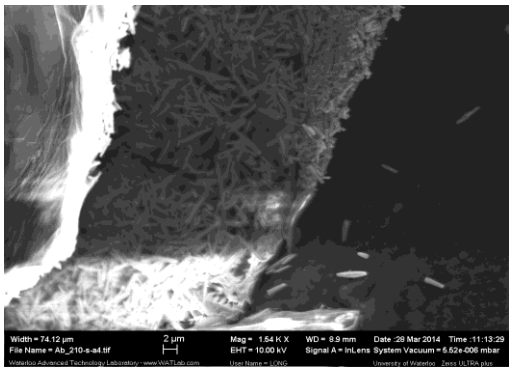

Fig. 5.10: SEM of ZnO nanorods in parallel way on the GO film.

5.4 Overview of Electrochemical Capacitors

5.4.1 Introduction to Electrochemical Capacitors

Sustainable and renewable sources of energy are growing enormously due to the environmental concerns over utilizing fossil fuels. Electrochemical capacitors (ECs) known as supercapacitors or ultracapacitors,[137] store electrical energy either in an electrochemical double layer (EDLCs), the so-called Helmholtz layer formed at the interface of the solid electrode and the electrolyte, or by rapid surface redox reactions (pseudo-capacitors).[138] ECs fill the gap between conventional capacitors and batteries as shown in Fig. 5.11.[139] This plot is called a Ragone plot,[140] which represents power versus energy density. It can be seen that ECs store energy in seconds compared to batteries due to their high surface area (1000–2000 m^2g^{-1}); however, the energy density is lower than batteries and this restrains the discharge time to be less than a minute while many applications demand much more.[139] Fig. 5.12 depicts a typical cyclic voltammogram of a two-electrode EDLC.[138]

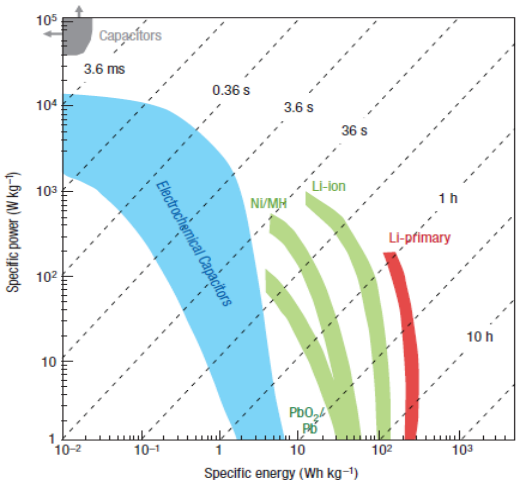

Fig. 5.11: A Ragone plot (power vs specific energy) for various electrical energy storage devices (taken from ref.[138] with permission from Nature Publishing Group).

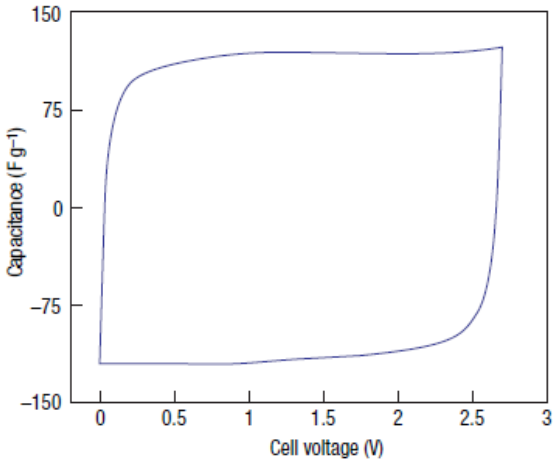

Fig. 5.12: Cyclic voltammetry of a two-electrode laboratory EDLC cell (taken from ref.[138] with permission from Nature Publishing Group).

5.4.2 Synthesis of Films for Capacitors

A variety of films have been prepared by mixing appropriate amounts of colloidal GO with zinc oxide nanorods and manganese dichloride followed by filtration through anodisc filter to obtain uniform films. Afterwards, these films have been reduced at 250 $^{\circ}$C and then tested for capacitance. The following table 5.3 summarizes the molar ratio of selected raw materials:

Table 5.3: The composition of samples used for capacitance testing.

Molar ratio
1 GO : 0.3 ZnO nanorods
GO film (250 $^{\circ}$C)
1 GO : 0.25 ZnO
1 GO : 0.5 ZnO
1 GO : 0.75 ZnO
1 GO : 1 ZnO
1 GO : 0.5 ZnO : 0.025 Mn^{2+}
1 GO : 0.5 ZnO : 0.08 Mn^{2+}
1 GO : 0.5 ZnO : 0.12 Mn^{2+}

5.4.3 Results and Discussion

The aforementioned samples can be divided into two groups. The first one is 1 GO : 0.3 ZnO nanorods, 1 GO : 0.25 ZnO, 1 GO : 0.5 ZnO, 1 GO : 0.75 ZnO, 1 GO : 1 ZnO, and GO film (250 $^{\circ}$C), and the second one is 1 GO : 0.5 ZnO : 0.025 Mn^{2+}, 1 GO : 0.5ZnO : 0.08Mn^{2+}, 1GO : 0.5ZnO : 0.12Mn^{2+}, and GO film (250 $^{\circ}$C). The objective of this classification was to investigate the influence of the concentration of ZnO nanorods on the capacitance in the first group and to take the optimal concentration of ZnO nanorods to be incorporated with different concentration of Mn^{2+} in the second group. The ZnO rods would act as electrically conducting spacers between the GO layers, preventing their stacking and hence increase their surface. Manganese ions are added with the purpose of forming MnO_2 at a later stage. MnO_2 ,being a redox active material, would allow the storage of charge by the acting as pseudo capacitive material, while the GO layer would store charge by the formation of EDL. Fig. 5.13 shows the effect of the concentration of ZnO nanorods on the capacitance at a scan rate of 50 mV/s. The relatively symmetrical rectangular shape of the CV plots indicates that the samples have an ideal EC behavior; however, the best shape was observed for the sample (molar ratio of 1 GO : 0.5 ZnO), which has an ideal rectangular shape. The capacitance for the standard sample, GO film (250 $^{\circ}$C), was 5.58×10^{-6} mF, and for the highest sample, 1 GO : 0.5 ZnO, is 2.54×10^{-5} mF, which is 4.55 higher than the standard. Based on these results, this ratio was chosen to be incorporated with different molar ratios of Mn^{2+}, so that the capacitance would be improved.

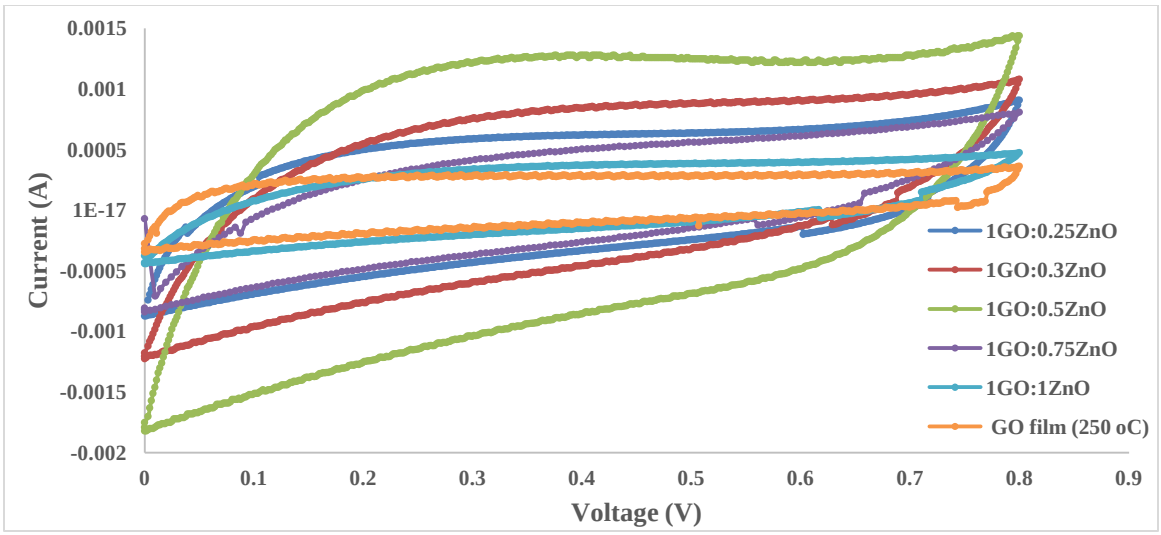

Fig. 5.13 Cyclic voltammograms of different molar ratios of ZnO nanorods (at50mV/s).

Three different concentrations of Mn^{2+} (0.025, 0.08, and 0.12) were incorporated with the sample (1 GO: 0. 5 ZnO). Fig. 5.14 shows the effect of adding these amounts of Mn^{2+} at a scan rate of (50 mV/s). The capacitance for the standard sample, GO film (250 $^{\circ}$C), was 5.58×10^{-6} mF and for the highest sample, 1 GO : 0.5 ZnO : 0.08 Mn^{2+}, was 2.25×10^{-5} mF, which is four times higher than the standard. It can be seen that the optimum ratio was 0.08 Mn^{2+}, which has an ideal rectangular shape which indicates that they could store higher charge density and improve the capacitance.

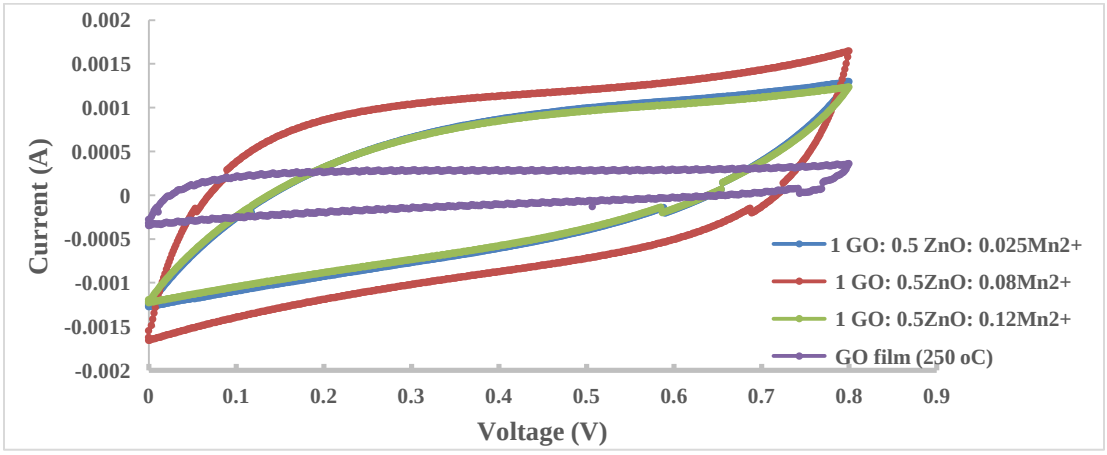

Fig. 5.14: Cyclic voltammograms of adding different molar ratios of Mn^{2+} (at 50 mV/s).

5.4.4 Conclusion and Future Work

The optimum molar ratio was for the sample 1 GO: 0.5 ZnO: 0.08 Mn^{2+}, and based on it, it would be beneficial for future researchers to use manganese nanostructures instead of just ions due to the huge surface area to the volume which in turn would store more charges, thus increasing the density of the capacitance. We already synthesized manganese oxide nanostructures according to the hydrothermal method that was used in this thesis to prepare ZnO nanorods. The starting materials were manganese nitrate and HMT. The SEM image for the product is shown in Figs. 5.15 and 5.16. Therefore, manganese oxide nanostructures should be incorporated with GO and ZnO nanorods so that more charges can be stored in them thus increasing the density of the capacitance and the performance.

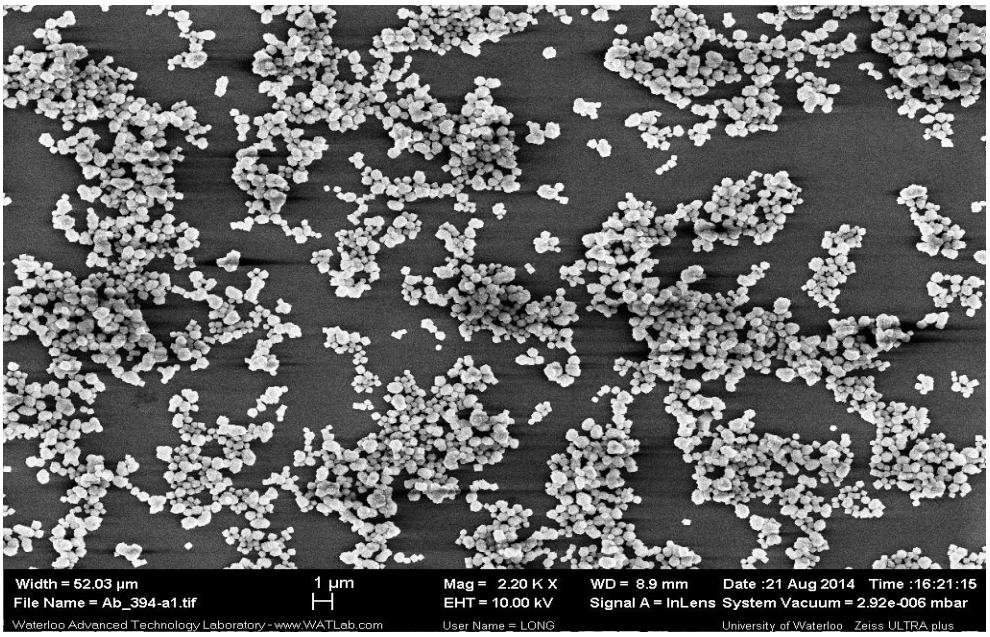

Fig. 5.15 SEM of hydrothermal growth of manganese oxide nanostructure.

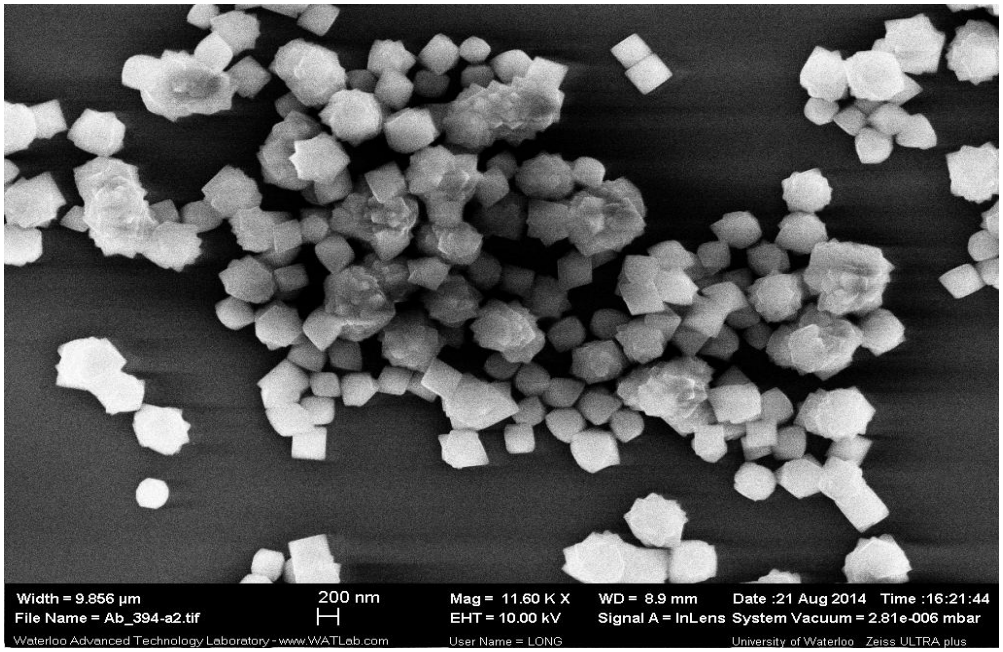

Fig. 5.16 SEM of the manganese dioxide nanostructures made by the hydrothermal method.

Chapter 6. Conclusion of Thesis

The objective of this thesis was to fabricate GO films by vacuum filtration of GO colloidal solution. Then thermal and chemical reductions were performed to control the d-spacing. This was used to study the diffusion of sodium, chloride, and calcium ions.

GO films were successfully synthesized then thermally reduced by exposing them for 30 minutes to a wide range of temperatures in air (60, 180, 200, 225, 250, 300 $^{\circ}$C). A gradual decrease in d-spacing from 7.4 Å to 6.9 Å to 6.5 Å is observed on increasing the temperature of reduction from 60 $^{\circ}$C to 180 $^{\circ}$C to 200 $^{\circ}$C, respectively. Then a drastic change was observed upon increasing the reduction temperature to 225 $^{\circ}$C as the spacing reduces to 4.8 Å. After that, little change was observed on increasing the temperature to 250 $^{\circ}$C or 300 $^{\circ}$C, which respectively brought about spacings of 4.6 Å and 4.57 Å. The change in going from 60 to 180 $^{\circ}$C corresponds to the evaporation of the residual water molecules in these films. An increase in temperature to 225 $^{\circ}$C causes the removal of the oxide functional groups on the surface of the GO films. These are primarily the defects caused by the oxidative treatment of the graphite for exfoliation to form GO sheets. Further increases in temperature only cause a slight change in the spacing leading to the conclusion that most of the defects have been removed at 225 $^{\circ}$C. The thermal treatment of the GO film was hence limited to 250 $^{\circ}$C in this work.

The tensile strength test was conducted for the GO films and found to be 69 MPa (GO-RT), 61 MPa (GO 180 $^{\circ}$C), 17 MPa (GO 200 $^{\circ}$C), and 21 MPa (225 $^{\circ}$C). The tensile strength reduces with temperature. At temperatures above 200 $^{\circ}$C, removal of oxygen containing functional groups occurs, and this reduced graphene oxide is more brittle than graphene oxide. The defects hence play a role in it; however, the GO 250 $^{\circ}$C and GO 300 $^{\circ}$C films were extremely brittle and tore immediately at the beginning of the tensile strength, which is why at the highest temperatures, tensile values are unavailable.

TGA confirmed the change in the mass of the starting GO film as the temperature is increased from ambient conditions to 900 $^{\circ}$C. Three transitions that lead to weight loss are observed over the temperature range. Primarily between 60–100 $^{\circ}$C, the loss in weight is associated with the removal of water molecules in the GO film. Following this, the weight is relatively constant until ~ 200 $^{\circ}$C, when a further reduction in mass of the GO film is observed. This corresponds to the sharp transition observed in the XRD data due to the reduction of the inter-layer spacing in the GO film. The combined TGA and XRD data lead to a conclusion that the phenomenon at 200 $^{\circ}$C is associated with the removal of the surface functional groups on the GO sheets. Finally, at a temperature of ~ 545 $^{\circ}$C, pyrolysis of the film reduced the weight to zero nearly.

FT-IR spectroscopy confirmed the existence of oxygen-containing functional groups such as hydroxyl, epoxy, and carboxyl groups in the GO films. It also confirmed that the oxygen functional groups were gradually removed with increasing annealing temperature, which is an indication for thermal reduction.

Raman spectroscopy confirmed the electronic structure and the degree of reduction of the GO films. All these films were compared to the Raman spectrum of graphite, which has two Raman peaks, the first one a strong band at 1574 cm^{-1} (G band), and the second a weak band at 1350 cm^{-1}. By comparing the G band of graphite with the rest of the films, it can be seen clearly that as the annealing temperature increases for the films, the G band is shifted to lower frequencies, approaching the G band of graphite. For instance, the G bands for the non-reduced GO film and GO reduced is at 180 $^{\circ}$C were at 1593 and 1594.5 cm^{-1}, respectively. However, as the annealing temperature was increased to 220, 225, and 250 $^{\circ}$C, the G band is shifted to 1583.7, 1584.7, and 1585.7 cm^{-1} , respectively, which is strong evidence for the restoration of the graphitic sp^2 network. These results are consistent with our XRD data for all the films.

XPS analysis also confirmed the removal of the oxygen-containing functional groups. Two strong peaks are located at 284.4 eV and 531.9 eV. They are attributed to the elemental carbon C 1s of sp^2 and the elemental oxygen O 1s respectively. It was found that the O/C ratio decreased markedly after thermal reduction at 250 $^{\circ}$C, as well as after chemical reduction of the GO via both hydrazine and ascorbic acid. This is an indication that most of the epoxide and hydroxyl functional groups were successfully eliminated. The XPS data is consistent with our TGA data in terms of the mass loss observed, as well as with our FT-IR spectroscopy results in terms of the removal of oxygen-containing functional groups.

Chemical reduction was successfully performed on GO films and on the GO colloids by hydrazine hydrate vapor as well as by ascorbic acid. The color of the GO film and the GO colloid changed from brown to grey and black, respectively, as indication for the reduction. The d-spacing was reduced from 7.4 Å for the non-reduced GO to 4.81 Å for GO chemically reduced by hydrazine hydrate vapor, and to 5.20 Å for GO reduced by ascorbic acid. It can be clearly seen that the chemical reduction yielded broad peaks as compared to thermal reduction, which yielded sharp peaks, indicating better performance for the latter.

Chemical cross-linking (Na^{+}, Mg^{2+}, Ba^{2+}, Fe^{2+}, Fe^{3+}) was performed in the GO films to explore the reduction in the d-spacing between rGO layers. No significance difference between the thermally reduced film at 250 $^{\circ}$C and the chemically cross-linked films, which were also reduced at 250 $^{\circ}$C, was observed.

Controlling the permeation of the species is based on the inter-layer spacing between the graphene sheets in GO membrane. The control over the inter-sheet spacing is hence a crucial parameter for modulating the diffusion characteristics of the graphene membranes. The non-reduced GO membranes have a large inter-layer spacing due to the functional groups present on its surface. The inter-layer spacing can be modulated by reduction of these membranes. This

is accomplished by a simple ambient thermal treatment. The thermal reduction causes the removal of the functional groups and hence also decreases the inter-layer spacing. The ability of the ions to diffuse across the graphene membrane is affected both by the free volume in the membrane and the presence of functional groups. The free volume that will depend on the inter-layer spacing and the functional groups that lead to hydrophilic characteristics in the membrane also affect the ability of these ions to diffuse across it, since water is still the fluid medium and the ions are charged. Based on the change in the inter-layer spacing and the functionalization of these membranes on thermal treatment, we expect that it can be used to control their ion diffusion characteristics. The increase in the conductivity of the de-ionized water resulting from the diffusion of the ions across the GO and TrGO membrane is monitored. The increase in the conductivity is directly proportional to the net amount of ions that cross into the de-ionized water. The increase can be modelled to be proportional to $t^{1/2}$ (the elapsed time) and diffusional resistance of the membrane. The effective diffusional resistance for the different Tr-GO membranes processed at different temperatures is calculated. We observe the diffusional resistance increases rapidly above 180 $^{\circ}$C, in line with the rapid reduction in the inter-layer spacing and the removal of functional groups above those temperatures. The trend in the case of 100 mM $CaCl_2$ is also identical. However, between the two ions differences in the relative change in the membrane resistance can be observed. For NaCl, the change is significantly more drastic than $CaCl_2$. This is due to the higher initial diffusion rate for the monovalent ion Na^+, which is consistent with its smaller size compared to Ca^{2+}. From the results, it can be illustrated that GO films treated at 60 $^{\circ}$C have better selectivity towards the Na^+ and Ca^{2+} ions and this selectivity decreases due to loss of permeation of the Na^+ ions predominantly. The treatment at 180 $^{\circ}$C leads to more than an order of magnitude decrease in the diffusion rate of Na^+, while the Ca^{2+} is roughly halved. The ability to control the diffusional characteristics of the GO membrane by thermal treatment and the temperature of exposure illustrate a simple method

to tailor the properties of these membranes. Further, this can also be expanded to include the effect on diffusion of small organic molecules and also gas permeation.

The inter-layer spacing is also reflected in the electrical conductivity of these membranes. In-plane and out-of-plane conductivity of the GO membranes were measured after thermal treatment at temperatures of 60 °C, 180 °C, 225 °C and 250 °C. The out-of-plane conductivity provides a direct measure of the change in the inter-layer spacing, whereas the in-plane conductivity depends on both the inherent conductivity of the GO (and TrGO) sheets and the overlap between the sheets. Typically for such membranes the in-plane conductivity measurements are dominated by the charge transport characteristics of the graphene (or TrGO) sheets. Based on this, the in-plane conductivity of the GO and TrGO membranes thermally reduced at 60 °C, 180 °C, 225 °C and 250 °C is measured. The in-plane conductivity increases by over 7 orders of magnitude between 60 °C and 250 °C. The in-plane conductivity in reduced GO sheets is based on the charge hopping model. The out-of-plane conduction in these membranes is over much shorter length scales, on the order of a few microns. This conduction shows a drastic increase as the thermal reduction temperature is increased from 60 °C to 250 °C. The out-of-plane conductivity increases by over 6 orders of magnitude. The charge conduction here can be considered as being governed by two aspects: (1) the sheets have spacing between them and, given the high electric field strength tunneling is expected for the transport of the charge carriers across the sheets. (2) direct contact between the sheets also occurs as they are stacked into layers. This direct contact can be modelled as an ohmic resistance for charge transport.

ZnO nanorods were grown on GO films via hydrothermal method to be used in photodegradation of organic pollutants. ZnO nanorods on GO film, colloidal of ZnO, and GO-ZnO composite were prepared and then used in photodegradation of MB. It was indicated that the GO-ZnO composite was the best in photodegradation of MB; however, the GO-ZnO film was

less efficient in photodegradation, it can be used several times by taking it from the pollutant solution to another one, which cannot be done by either ZnO nanorods or GO-ZnO composite.

ZnO nanorods were incorporated between reduced GO layers so that they could segregate the reduced GO layers and provide a large surface area. Divalent manganese ions were also used to form manganese dioxide so that it can be store more charges and hence increase the energy density. The optimum molar ratio for the highest efficiency of capacitance was 1GO: 0.5ZnO film, which has capacitance 2.54×10^{-5} mF. After incorporation of divalent manganese ions, the optimum molar ratio was 1GO:0.5ZnO:0.08Mn^{2+}, which has capacitance 2.25×10^{-5} mF. The two values are four to five times higher than the standard GO sample, whose capacitance is 5.58×10^{-6} mF.

Applying a surface potential to the GO membranes is another avenue that needs to be explored for further modulating the transport of the ion across these membranes. The preliminary results show promising trends with this approach.

References

1. Toda, K.; Furue, R.; Hayami, S., Recent progress in applications of graphene oxide for gas sensing: A review. *Analytica chimica acta* **2015,** *878*, 43-53.

2. Gupta, A.; Sakthivel, T.; Seal, S., Recent development in 2D materials beyond graphene. *Progress in Materials Science* **2015,** *73*, 44-126.

3. Abdelkader, A.; Cooper, A.; Dryfe, R.; Kinloch, I., How to get between the sheets: a review of recent works on the electrochemical exfoliation of graphene materials from bulk graphite. *Nanoscale* **2015,** *7* (16), 6944-6956.

4. Geim, A. K.; Novoselov, K. S., The rise of graphene. *Nature Materials* **2007,** *6* (3), 183-191.

5. Novoselov, K. S.; Fal, V.; Colombo, L.; Gellert, P.; Schwab, M.; Kim, K., A roadmap for graphene. *Nature* **2012,** *490* (7419), 192-200.

6. Georgakilas, V.; Otyepka, M.; Bourlinos, A. B.; Chandra, V.; Kim, N.; Kemp, K. C.; Hobza, P.; Zboril, R.; Kim, K. S., Functionalization of graphene: covalent and non-covalent approaches, derivatives and applications. *Chemical reviews* **2012,** *112* (11), 6156-6214.

7. Dikin, D. A.; Stankovich, S.; Zimney, E. J.; Piner, R. D.; Dommett, G. H.; Evmenenko, G.; Nguyen, S. T.; Ruoff, R. S., Preparation and characterization of graphene oxide paper. *Nature* **2007,** *448* (7152), 457-460.

8. Sun, Y.; Wu, Q.; Shi, G., Graphene based new energy materials. *Energy & Environmental Science* **2011,** *4* (4), 1113-1132.

9. Singh, V.; Joung, D.; Zhai, L.; Das, S.; Khondaker, S. I.; Seal, S., Graphene based materials: past, present and future. *Progress in Materials Science* **2011,** *56* (8), 1178-1271.

10. Stankovich, S.; Dikin, D. A.; Dommett, G. H.; Kohlhaas, K. M.; Zimney, E. J.; Stach, E. A.; Piner, R. D.; Nguyen, S. T.; Ruoff, R. S., Graphene-based composite materials. *Nature* **2006,** *442* (7100), 282-286.

11. Katsnelson, M. I.; Katsnel'son, M. I., *Graphene: carbon in two dimensions*. Cambridge University Press: 2012.

12. Brodie, B. C., On the atomic weight of graphite. *Philosophical Transactions of the Royal Society of London* **1859**, 249-259.

13. Staudenmaier, L., Verfahren zur darstellung der graphitsäure. *Berichte der deutschen chemischen Gesellschaft* **1898,** *31* (2), 1481-1487.

14. Hummers Jr, W. S.; Offeman, R. E., Preparation of graphitic oxide. *Journal of the American Chemical Society* **1958,** *80* (6), 1339-1339.

15. Dreyer, D. R.; Park, S.; Bielawski, C. W.; Ruoff, R. S., The chemistry of graphene oxide. *Chemical Society Reviews* **2010,** *39* (1), 228-240.

16. Wissler, M., Graphite and carbon powders for electrochemical applications. *Journal of Power Sources* **2006,** *156* (2), 142-150.

17. Scholz, W.; Boehm, H., Untersuchungen am graphitoxid. VI. Betrachtungen zur struktur des graphitoxids. *Zeitschrift für anorganische und allgemeine Chemie* **1969,** *369* (3-6), 327-340.

18. Nakajima, T.; Mabuchi, A.; Hagiwara, R., A new structure model of graphite oxide. *Carbon* **1988,** *26* (3), 357-361.

19. Szabó, T.; Berkesi, O.; Forgó, P.; Josepovits, K.; Sanakis, Y.; Petridis, D.; Dékány, I., Evolution of surface functional groups in a series of progressively oxidized graphite oxides. *Chemistry of Materials* **2006,** *18* (11), 2740-2749.

20. Lerf, A.; He, H.; Forster, M.; Klinowski, J., Structure of graphite oxide revisited. *The Journal of Physical Chemistry B* **1998,** *102* (23), 4477-4482.

21. He, H.; Klinowski, J.; Forster, M.; Lerf, A., A new structural model for graphite oxide. *Chemical Physics Letters* **1998,** *287* (1), 53-56.

22. Park, S.; Ruoff, R. S., Chemical methods for the production of graphenes. *Nature nanotechnology* **2009,** *4* (4), 217-224.

23. Zhu, Y.; Murali, S.; Cai, W.; Li, X.; Suk, J. W.; Potts, J. R.; Ruoff, R. S., Graphene and graphene oxide: synthesis, properties, and applications. *Advanced materials* **2010,** *22* (35), 3906-3924.

24. Liu, C.; Hao, F.; Zhao, X.; Zhao, Q.; Luo, S.; Lin, H., Low temperature reduction of free-standing graphene oxide papers with metal iodides for ultrahigh bulk conductivity. *Scientific reports* **2014,** *4*.

25. Novoselov, K. S.; Geim, A. K.; Morozov, S.; Jiang, D.; Zhang, Y.; Dubonos, S.; Grigorieva, I.; Firsov, A., Electric field effect in atomically thin carbon films. *science* **2004,** *306* (5696), 666-669.

26. Kavan, L.; Yum, J. H.; Grätzel, M., Optically transparent cathode for dye-sensitized solar cells based on graphene nanoplatelets. *ACS Nano* **2010,** *5* (1), 165-172.

27. Zhao, X.; Tian, H.; Zhu, M.; Tian, K.; Wang, J.; Kang, F.; Outlaw, R., Carbon nanosheets as the electrode material in supercapacitors. *Journal of Power Sources* **2009,** *194* (2), 1208-1212.

28. Dimitrakakis, G. K.; Tylianakis, E.; Froudakis, G. E., Pillared graphene: a new 3-D network nanostructure for enhanced hydrogen storage. *Nano letters* **2008,** *8* (10), 3166-3170.

29. Dreyer, D.; Jia, H.; Bielawski, C., Graphene oxide: a convenient carbocatalyst for facilitating oxidation and hydration reactions. *Angewandte Chemie (International ed. in English)* **2010,** *49* (38), 6813-6816.

30. Liao, L.; Bai, J.; Cheng, R.; Lin, Y.-C.; Jiang, S.; Huang, Y.; Duan, X., Top-gated graphene nanoribbon transistors with ultrathin high-k dielectrics. *Nano letters* **2010,** *10* (5), 1917-1921.

31. Blake, P.; Brimicombe, P. D.; Nair, R. R.; Booth, T. J.; Jiang, D.; Schedin, F.; Ponomarenko, L. A.; Morozov, S. V.; Gleeson, H. F.; Hill, E. W., Graphene-based liquid crystal device. *Nano letters* **2008,** *8* (6), 1704-1708.

32. Bunch, J. S.; Van Der Zande, A. M.; Verbridge, S. S.; Frank, I. W.; Tanenbaum, D. M.; Parpia, J. M.; Craighead, H. G.; McEuen, P. L., Electromechanical resonators from graphene sheets. *science* **2007,** *315* (5811), 490-493.

33. Lu, X.; Yu, M.; Huang, H.; Ruoff, R. S., Tailoring graphite with the goal of achieving single sheets. *Nanotechnology* **1999,** *10* (3), 269.

34. Lee, S.; Lee, K.; Zhong, Z., Wafer scale homogeneous bilayer graphene films by chemical vapor deposition. *Nano letters* **2010,** *10* (11), 4702-4707.

35. Berger, C.; Song, Z.; Li, X.; Wu, X.; Brown, N.; Naud, C.; Mayou, D.; Li, T.; Hass, J.; Marchenkov, A. N., Electronic confinement and coherence in patterned epitaxial graphene. *science* **2006,** *312* (5777), 1191-1196.

36. Dong, X.; Su, C.-Y.; Zhang, W.; Zhao, J.; Ling, Q.; Huang, W.; Chen, P.; Li, L.-J., Ultra-large single-layer graphene obtained from solution chemical reduction and its electrical properties. *Physical Chemistry Chemical Physics* **2010,** *12* (9), 2164-2169.

37. Zhou, X.; Huang, X.; Qi, X.; Wu, S.; Xue, C.; Boey, F. Y.; Yan, Q.; Chen, P.; Zhang, H., In situ synthesis of metal nanoparticles on single-layer graphene oxide and reduced graphene oxide surfaces. *The Journal of Physical Chemistry C* **2009,** *113* (25), 10842-10846.

38. Li, J.; Lin, H.; Yang, Z.; Li, J., A method for the catalytic reduction of graphene oxide at temperatures below 150° C. *Carbon* **2011,** *49* (9), 3024-3030.

39. Li, D.; Mueller, M. B.; Gilje, S.; Kaner, R. B.; Wallace, G. G., Processable aqueous dispersions of graphene nanosheets. *Nature nanotechnology* **2008,** *3* (2), 101-105.

40. Stankovich, S.; Piner, R. D.; Chen, X.; Wu, N.; Nguyen, S. T.; Ruoff, R. S., Stable aqueous dispersions of graphitic nanoplatelets via the reduction of exfoliated graphite oxide in the presence of poly (sodium 4-styrenesulfonate). *Journal of Materials Chemistry* **2006,** *16* (2), 155-158.

41. Park, S.; Lee, K.-S.; Bozoklu, G.; Cai, W.; Nguyen, S. T.; Ruoff, R. S., Graphene oxide papers modified by divalent ions—enhancing mechanical properties via chemical cross-linking. *ACS nano* **2008,** *2* (3), 572-578.

42. Stankovich, S.; Piner, R. D.; Nguyen, S. T.; Ruoff, R. S., Synthesis and exfoliation of isocyanate-treated graphene oxide nanoplatelets. *Carbon* **2006,** *44* (15), 3342-3347.

43. Paredes, J.; Villar-Rodil, S.; Martinez-Alonso, A.; Tascon, J., Graphene oxide dispersions in organic solvents. *Langmuir* **2008,** *24* (19), 10560-10564.

44. Stankovich, S.; Dikin, D. A.; Piner, R. D.; Kohlhaas, K. A.; Kleinhammes, A.; Jia, Y.; Wu, Y.; Nguyen, S. T.; Ruoff, R. S., Synthesis of graphene-based nanosheets via chemical reduction of exfoliated graphite oxide. *Carbon* **2007,** *45* (7), 1558-1565.

45. Peng, H.; Meng, L.; Niu, L.; Lu, Q., Simultaneous reduction and surface functionalization of graphene oxide by natural cellulose with the assistance of the ionic liquid. *The Journal of Physical Chemistry C* **2012,** *116* (30), 16294-16299.

46. He, F.; Fan, J.; Ma, D.; Zhang, L.; Leung, C.; Chan, H. L., The attachment of Fe 3 O 4 nanoparticles to graphene oxide by covalent bonding. *Carbon* **2010,** *48* (11), 3139-3144.

47. Pei, S.; Zhao, J.; Du, J.; Ren, W.; Cheng, H.-M., Direct reduction of graphene oxide films into highly conductive and flexible graphene films by hydrohalic acids. *Carbon* **2010,** *48* (15), 4466-4474.

48. Zhao, J.; Pei, S.; Ren, W.; Gao, L.; Cheng, H.-M., Efficient preparation of large-area graphene oxide sheets for transparent conductive films. *ACS Nano* **2010,** *4* (9), 5245-5252.

49. Wang, G.; Yang, J.; Park, J.; Gou, X.; Wang, B.; Liu, H.; Yao, J., Facile synthesis and characterization of graphene nanosheets. *The Journal of Physical Chemistry C* **2008,** *112* (22), 8192-8195.

50. Fernandez-Merino, M.; Guardia, L.; Paredes, J.; Villar-Rodil, S.; Solis-Fernandez, P.; Martinez-Alonso, A.; Tascon, J., Vitamin C is an ideal substitute for hydrazine in the reduction of graphene oxide suspensions. *The Journal of Physical Chemistry C* **2010,** *114* (14), 6426-6432.

51. Fan, X.; Peng, W.; Li, Y.; Li, X.; Wang, S.; Zhang, G.; Zhang, F., Deoxygenation of exfoliated graphite oxide under alkaline conditions: a green route to graphene preparation. *Advanced Materials* **2008,** *20* (23), 4490-4493.

52. Schniepp, H. C.; Li, J.-L.; McAllister, M. J.; Sai, H.; Herrera-Alonso, M.; Adamson, D. H.; Prud'homme, R. K.; Car, R.; Saville, D. A.; Aksay, I. A., Functionalized single graphene sheets derived from splitting graphite oxide. *The Journal of Physical Chemistry B* **2006,** *110* (17), 8535-8539.

53. McAllister, M. J.; Li, J.-L.; Adamson, D. H.; Schniepp, H. C.; Abdala, A. A.; Liu, J.; Herrera-Alonso, M.; Milius, D. L.; Car, R.; Prud'homme, R. K., Single sheet functionalized graphene by oxidation and thermal expansion of graphite. *Chemistry of Materials* **2007,** *19* (18), 4396-4404.

54. Williams, G.; Seger, B.; Kamat, P. V., TiO2-graphene nanocomposites. UV-assisted photocatalytic reduction of graphene oxide. *ACS Nano* **2008,** *2* (7), 1487-1491.

55. Sun, P.; Zhu, M.; Wang, K.; Zhong, M.; Wei, J.; Wu, D.; Xu, Z.; Zhu, H., Selective Ion Penetration of Graphene Oxide Membranes. *ACS Nano* **2013,** *7* (1), 428-437.

56. Sint, K.; Wang, B.; Král, P., Selective ion passage through functionalized graphene nanopores. *Journal of the American Chemical Society* **2008,** *130* (49), 16448-16449.

57. Lee, J.; Novoselov, K. S.; Shin, H. S., Interaction between metal and graphene: dependence on the layer number of graphene. *ACS Nano* **2010,** *5* (1), 608-612.

58. Neto, A. C.; Guinea, F.; Peres, N.; Novoselov, K. S.; Geim, A. K., The electronic properties of graphene. *Reviews of modern physics* **2009,** *81* (1), 109.

59. Baker, R. W., *Membrane Technology and Applications*. Wiley: 2012.

60. Wang, E. N.; Karnik, R., Water desalination: Graphene cleans up water. *Nature nanotechnology* **2012,** *7* (9), 552-554.

61. Suk, M. E.; Aluru, N., Water transport through ultrathin graphene. *The Journal of Physical Chemistry Letters* **2010,** *1* (10), 1590-1594.

62. Russo, C. J.; Golovchenko, J., Atom-by-atom nucleation and growth of graphene nanopores. *Proceedings of the National Academy of Sciences* **2012,** *109* (16), 5953-5957.

63. Garaj, S.; Hubbard, W.; Reina, A.; Kong, J.; Branton, D.; Golovchenko, J., Graphene as a subnanometre trans-electrode membrane. *Nature* **2010,** *467* (7312), 190-193.

64. Bell, D. C.; Lemme, M. C.; Stern, L. A.; Williams, J. R.; Marcus, C. M., Precision cutting and patterning of graphene with helium ions. *Nanotechnology* **2009,** *20* (45), 455301.

65. Bieri, M.; Treier, M.; Cai, J.; Aït-Mansour, K.; Ruffieux, P.; Gröning, O.; Gröning, P.; Kastler, M.; Rieger, R.; Feng, X., Porous graphenes: two-dimensional polymer synthesis with atomic precision. *Chemical communications* **2009,** (45), 6919-6921.

66. Kim, M.; Safron, N. S.; Han, E.; Arnold, M. S.; Gopalan, P., Fabrication and characterization of large-area, semiconducting nanoperforated graphene materials. *Nano letters* **2010,** *10* (4), 1125-1131.

67. Cohen-Tanugi, D.; Grossman, J. C., Water desalination across nanoporous graphene. *Nano letters* **2012,** *12* (7), 3602-3608.

68. Nair, R.; Wu, H.; Jayaram, P.; Grigorieva, I.; Geim, A., Unimpeded permeation of water through helium-leak–tight graphene-based membranes. *Science* **2012,** *335* (6067), 442-444.

69. Paul, D. R., Creating new types of carbon-based membranes. *Science* **2012,** *335* (6067), 413-414.

70. Fischbein, M. D.; Drndić, M., Electron beam nanosculpting of suspended graphene sheets. *Applied Physics Letters* **2008,** *93* (11), 113107.

71. Stampfer, C.; Güttinger, J.; Molitor, F.; Graf, D.; Ihn, T.; Ensslin, K., Tunable Coulomb blockade in nanostructured graphene. *Applied Physics Letters* **2008,** *92* (1), 012102.

72. Schrier, J., Helium separation using porous graphene membranes. *The Journal of Physical Chemistry Letters* **2010,** *1* (15), 2284-2287.

73. Jiang, D.-e.; Cooper, V. R.; Dai, S., Porous graphene as the ultimate membrane for gas separation. *Nano letters* **2009,** *9* (12), 4019-4024.

74. Du, H.; Li, J.; Zhang, J.; Su, G.; Li, X.; Zhao, Y., Separation of hydrogen and nitrogen gases with porous graphene membrane. *The Journal of Physical Chemistry C* **2011,** *115* (47), 23261-23266.

75. Bunch, J. S.; Verbridge, S. S.; Alden, J. S.; van der Zande, A. M.; Parpia, J. M.; Craighead, H. G.; McEuen, P. L., Impermeable atomic membranes from graphene sheets. *Nano letters* **2008,** *8* (8), 2458-2462.

76. Kaiser, A. B.; Gómez-Navarro, C.; Sundaram, R. S.; Burghard, M.; Kern, K., Electrical conduction mechanism in chemically derived graphene monolayers. *Nano letters* **2009,** *9* (5), 1787-1792.

77. Maheshwari, V.; Saraf, R. F., High-resolution thin-film device to sense texture by touch. *science* **2006,** *312* (5779), 1501-1504.

78. Bragg, W. L. In *The diffraction of short electromagnetic waves by a crystal*, Proceedings of the Cambridge Philosophical Society, 1913; p 4.

79. Smart, L. E.; Moore, E. A., *Solid state chemistry: an introduction*. CRC press: 2012.

80. West, A. R., *Basic solid state chemistry*. John Wiley & Sons Inc: 1999.

81. Ooi, L.-l., *Principles of X-ray Crystallography*. Oxford University Press: 2010.

82. Smart, L.; Moore, E., Solid State Chemistry: An Introduction, 2005. Taylor & Francis.

83. Bozzola, J. J., Electron microscopy. principles and techniques for biologists. **1992**.

84. Egerton, R., *Physical principles of electron microscopy: an introduction to TEM, SEM, and AEM*. Springer Science & Business Media: 2006.

85. Smith, B. C., *Fundamentals of Fourier transform infrared spectroscopy*. CRC press: 2011.

86. Perkampus, H.-H.; Grinter, H.-C.; Threlfall, T., *UV-VIS Spectroscopy and its Applications*. Springer: 1992.

87. Wiberley, S. E.; Colthup, N.; Daly, L., Introduction to infrared and Raman Spectroscopy. *ed. NB Colthup and LH Daly, Academic Press, Inc., San Diego* **1990**.

88. KRISHNAN, K., A new class of spectra due to secondary radiation Part I. *Indian J. Phys* **1928,** *2*, 399-419.

89. Zhang, S.-L., *Raman spectroscopy and its application in nanostructures*. John Wiley & Sons: 2012.

90. Denney, R. C.; Sinclair, R.; Mowthorpe, D. J., *Visible and ultraviolet spectroscopy*. Published on behalf of ACOL, Thames Polytechnic, Lo ndon, by Wiley: 1987.

91. http://teaching.shu.ac.uk/hwb/chemistry/tutorials/molspec/uvvisab1.htm.

92. Fadley, C., X-ray photoelectron spectroscopy: Progress and perspectives. *Journal of Electron Spectroscopy and Related Phenomena* **2010,** *178*, 2-32.

93. Watts, J. F.; Wolstenholme, J., An introduction to surface analysis by XPS and AES. *An Introduction to Surface Analysis by XPS and AES, by John F. Watts, John Wolstenholme, pp. 224. ISBN 0-470-84713-1. Wiley-VCH, May 2003.* **2003,** *1*.

94. Kovtyukhova, N. I.; Ollivier, P. J.; Martin, B. R.; Mallouk, T. E.; Chizhik, S. A.; Buzaneva, E. V.; Gorchinskiy, A. D., Layer-by-layer assembly of ultrathin composite films from micron-sized graphite oxide sheets and polycations. *Chemistry of Materials* **1999,** *11* (3), 771-778.

95. Eda, G.; Fanchini, G.; Chhowalla, M., Large-area ultrathin films of reduced graphene oxide as a transparent and flexible electronic material. *Nature nanotechnology* **2008,** *3* (5), 270-274.

96. Tang, H.; Ehlert, G. J.; Lin, Y.; Sodano, H. A., Highly efficient synthesis of graphene nanocomposites. *Nano letters* **2011,** *12* (1), 84-90.

97. Wang, Z.-l.; Xu, D.; Huang, Y.; Wu, Z.; Wang, L.-m.; Zhang, X.-b., Facile, mild and fast thermal-decomposition reduction of graphene oxide in air and its application in high-performance lithium batteries. *Chemical Communications* **2012,** *48* (7), 976-978.

98. Bourlinos, A. B.; Gournis, D.; Petridis, D.; Szabó, T.; Szeri, A.; Dékány, I., Graphite oxide: chemical reduction to graphite and surface modification with primary aliphatic amines and amino acids. *Langmuir* **2003,** *19* (15), 6050-6055.

99. Hofmann, U.; Frenzel, A., The reduction of graphite oxide with hydrogen sulphide. *Kolloid-Zeitschrift* **1934,** *68* (2), 149-151.

100. Xiao, P.; Xiao, M.; Liu, P.; Gong, K., Direct synthesis of a polyaniline-intercalated graphite oxide nanocomposite. *Carbon* **2000,** *38* (4), 626-628.

101. Kotov, N. A.; Dékány, I.; Fendler, J. H., Ultrathin graphite oxide–polyelectrolyte composites prepared by self-assembly: Transition between conductive and non-conductive states. *Advanced Materials* **1996,** *8* (8), 637-641.

102. Jin, Y.; Huang, S.; Zhang, M.; Jia, M.; Hu, D., A green and efficient method to produce graphene for electrochemical capacitors from graphene oxide using sodium carbonate as a reducing agent. *Applied Surface Science* **2013,** *268*, 541-546.

103. Park, S.; An, J.; Potts, J. R.; Velamakanni, A.; Murali, S.; Ruoff, R. S., Hydrazine-reduction of graphite-and graphene oxide. *Carbon* **2011,** *49* (9), 3019-3023.

104. Su, X.; Wang, G.; Li, W.; Bai, J.; Wang, H., A simple method for preparing graphene nano-sheets at low temperature. *Advanced Powder Technology* **2013,** *24* (1), 317-323.

105. YAN, J.-l.; CHEN, G.-j.; Jun, C.; Wei, Y.; XIE, B.-h.; YANG, M.-b., Functionalized graphene oxide with ethylenediamine and 1, 6-hexanediamine. *New Carbon Materials* **2012,** *27* (5), 370-376.

106. Chen, H.; Müller, M. B.; Gilmore, K. J.; Wallace, G. G.; Li, D., Mechanically strong, electrically conductive, and biocompatible graphene paper. *Advanced Materials* **2008,** *20* (18), 3557-3561.

107. Dai, Y.; Ni, S.; Li, Z.; Yang, J., Diffusion and desorption of oxygen atoms on graphene. *Journal of Physics: Condensed Matter* **2013,** *25* (40), 405301.

108. Koenig, S. P.; Wang, L.; Pellegrino, J.; Bunch, J. S., Selective molecular sieving through porous graphene. *Nature nanotechnology* **2012,** *7* (11), 728-732.

109. O'Hern, S. C.; Stewart, C. A.; Boutilier, M. S.; Idrobo, J.-C.; Bhaviripudi, S.; Das, S. K.; Kong, J.; Laoui, T.; Atieh, M.; Karnik, R., Selective molecular transport through intrinsic defects in a single layer of CVD graphene. *ACS nano* **2012,** *6* (11), 10130-10138.

110. Pei, S.; Cheng, H.-M., The reduction of graphene oxide. *Carbon* **2012,** *50* (9), 3210-3228.

111. Jeong, H.-K.; Lee, Y. P.; Jin, M. H.; Kim, E. S.; Bae, J. J.; Lee, Y. H., Thermal stability of graphite oxide. *Chemical Physics Letters* **2009,** *470* (4), 255-258.

112. Gómez-Navarro, C.; Weitz, R. T.; Bittner, A. M.; Scolari, M.; Mews, A.; Burghard, M.; Kern, K., Electronic transport properties of individual chemically reduced graphene oxide sheets. *Nano letters* **2007,** *7* (11), 3499-3503.

113. Callister, W. D.; Rethwisch, D. G., *Materials science and engineering: an introduction*. Wiley New York: 2007; Vol. 7.

114. Nightingale Jr, E., Phenomenological theory of ion solvation. Effective radii of hydrated ions. *The Journal of Physical Chemistry* **1959,** *63* (9), 1381-1387.

115. Teoh, W. Y.; Scott, J. A.; Amal, R., Progress in heterogeneous photocatalysis: from classical radical chemistry to engineering nanomaterials and solar reactors. *The Journal of Physical Chemistry Letters* **2012,** *3* (5), 629-639.

116. Fujishima, A., Electrochemical photolysis of water at a semiconductor electrode. *Nature* **1972,** *238*, 37-38.

117. An, X.; Jimmy, C. Y., Graphene-based photocatalytic composites. *Rsc Advances* **2011,** *1* (8), 1426-1434.

118. Khataee, A.; Kasiri, M. B., Photocatalytic degradation of organic dyes in the presence of nanostructured titanium dioxide: influence of the chemical structure of dyes. *Journal of Molecular Catalysis A: Chemical* **2010,** *328* (1), 8-26.

119. Chong, M. N.; Jin, B.; Chow, C. W.; Saint, C., Recent developments in photocatalytic water treatment technology: a review. *Water research* **2010,** *44* (10), 2997-3027.

120. Liu, G.; Han, C.; Pelaez, M.; Zhu, D.; Liao, S.; Likodimos, V.; Kontos, A. G.; Falaras, P.; Dionysiou, D. D., Enhanced visible light photocatalytic activity of C N-codoped TiO 2 films for the degradation of microcystin-LR. *Journal of Molecular Catalysis A: Chemical* **2013,** *372*, 58-65.

121. Liu, G.; Han, C.; Pelaez, M.; Zhu, D.; Liao, S.; Likodimos, V.; Ioannidis, N.; Kontos, A. G.; Falaras, P.; Dunlop, P. S., Synthesis, characterization and photocatalytic evaluation of visible light activated C-doped TiO2 nanoparticles. *Nanotechnology* **2012,** *23* (29), 294003.

122. Gao, Y.; Hu, M.; Mi, B., Membrane surface modification with TiO 2–graphene oxide for enhanced photocatalytic performance. *Journal of Membrane Science* **2014,** *455*, 349-356.

123. Mo, S.-D.; Ching, W., Electronic and optical properties of three phases of titanium dioxide: Rutile, anatase, and brookite. *Physical Review B* **1995,** *51* (19), 13023.

124. Iskandar, F.; Nandiyanto, A. B. D.; Yun, K. M.; Hogan, C. J.; Okuyama, K.; Biswas, P., Enhanced photocatalytic performance of brookite TiO2 macroporous particles prepared by spray drying with colloidal templating. *Advanced Materials* **2007,** *19* (10), 1408-1412.

125. Bavykin, D. V.; Friedrich, J. M.; Walsh, F. C., Protonated titanates and TiO2 nanostructured materials: synthesis, properties, and applications. *Advanced Materials* **2006,** *18* (21), 2807-2824.

126. Koelsch, M.; Cassaignon, S.; Guillemoles, J.; Jolivet, J., Comparison of optical and electrochemical properties of anatase and brookite TiO 2 synthesized by the sol–gel method. *Thin Solid Films* **2002,** *403*, 312-319.

127. Woodley, S.; Catlow, C., Structure prediction of titania phases: implementation of Darwinian versus Lamarckian concepts in an evolutionary algorithm. *Computational Materials Science* **2009,** *45* (1), 84-95.

128. MONDAL, K.; SHARMA, A., Photocatalytic Oxidation of Pollutant Dyes in Wastewater by TiO2 and ZnO nano-materials–A Mini-review. *inNanoscience & Technology for Mankind* **2014**, 36-72.

129. Özgür, Ü.; Alivov, Y. I.; Liu, C.; Teke, A.; Reshchikov, M.; Doğan, S.; Avrutin, V.; Cho, S.-J.; Morkoc, H., A comprehensive review of ZnO materials and devices. *Journal of applied physics* **2005,** *98* (4), 041301.

130. Baruah, S.; Dutta, J., Hydrothermal growth of ZnO nanostructures. *Science and Technology of Advanced Materials* **2009,** *10* (1), 013001.

131. Polsongkram, D.; Chamninok, P.; Pukird, S.; Chow, L.; Lupan, O.; Chai, G.; Khallaf, H.; Park, S.; Schulte, A., Effect of synthesis conditions on the growth of ZnO nanorods via hydrothermal method. *Physica B: Condensed Matter* **2008,** *403* (19), 3713-3717.

132. Krichevsky, O.; Stavans, J., Correlated Ostwald ripening in two dimensions. *Physical review letters* **1993,** *70* (10), 1473.

133. Yu, S.; Wang, X.; Tan, X.; Wang, X., Sorption of radionuclides from aqueous systems onto graphene oxide-based materials: a review. *Inorganic Chemistry Frontiers* **2015,** *2* (7), 593-612.

134. Bizarro, M., High photocatalytic activity of ZnO and ZnO: Al nanostructured films deposited by spray pyrolysis. *Applied Catalysis B: Environmental* **2010,** *97* (1), 198-203.

135. Joshi, B. N.; Yoon, H.; Na, S.-H.; Choi, J.-Y.; Yoon, S. S., Enhanced photocatalytic performance of graphene–ZnO nanoplatelet composite thin films prepared by electrostatic spray deposition. *Ceramics International* **2014,** *40* (2), 3647-3654.

136. Pawar, R. C.; Lee, C. S., Single-step sensitization of reduced graphene oxide sheets and CdS nanoparticles on ZnO nanorods as visible-light photocatalysts. *Applied Catalysis B: Environmental* **2014,** *144*, 57-65.

137. Miller, J. R.; Simon, P., Electrochemical capacitors for energy management. *Science Magazine* **2008,** *321* (5889), 651-652.

138. Simon, P.; Gogotsi, Y., Materials for electrochemical capacitors. *Nature Materials* **2008,** *7* (11), 845-854.

139. Kötz, R.; Carlen, M., Principles and applications of electrochemical capacitors. *Electrochimica Acta* **2000,** *45* (15), 2483-2498.

140. Service, R. F., Materials science. New'supercapacitor'promises to pack more electrical punch. *Science (New York, NY)* **2006,** *313* (5789), 902.

Appendices

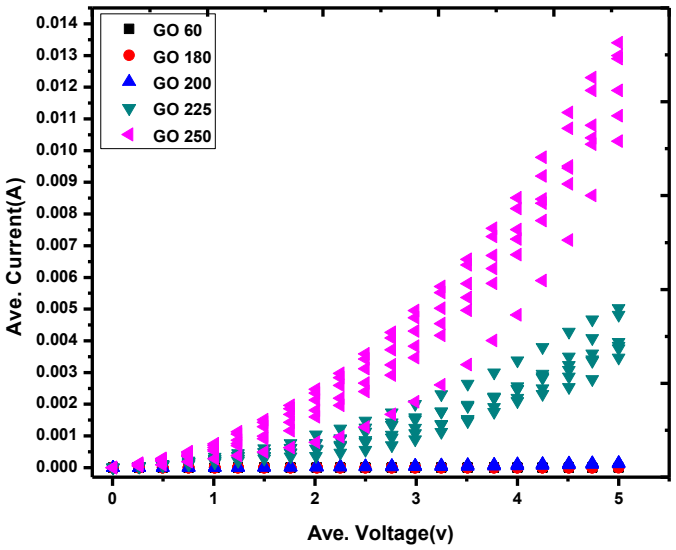

Fig. A1 (a). I-V Out-of-plane test of GO 60, GO 180, GO 200, GO 225, And GO 250 °C.

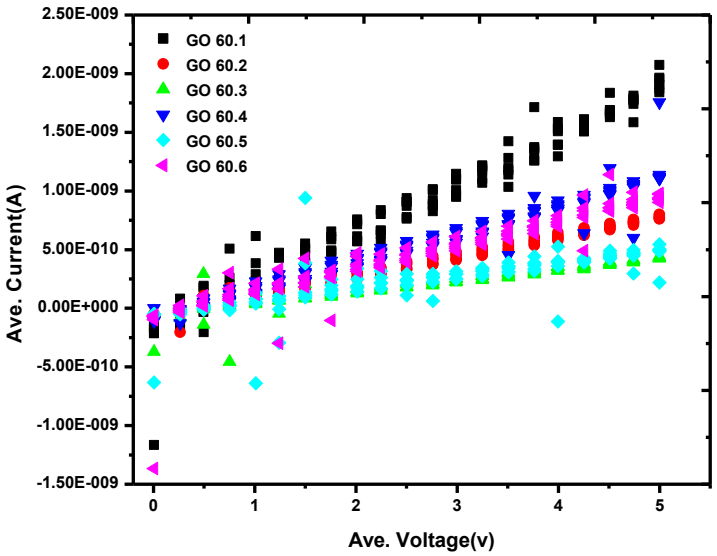

Fig. A1 (b). I-V In-plane test GO 60 °C.

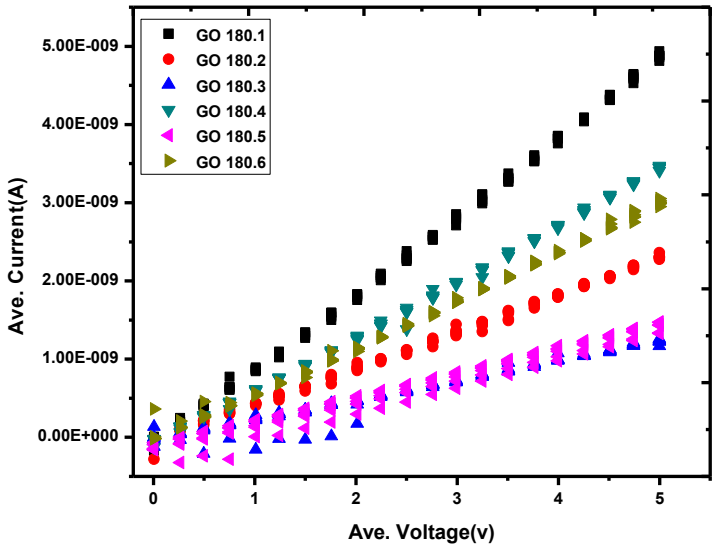

Fig. A1 (c). I-V In-plane test GO 180 °C.

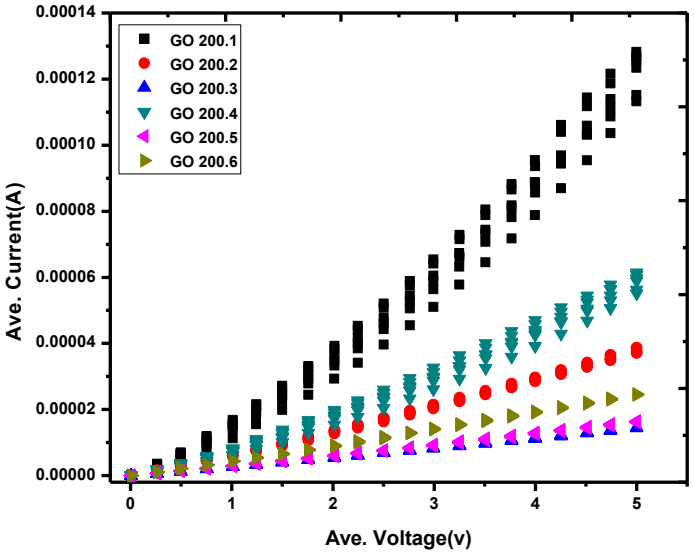

Fig. A1 (d). I-V In-plane test GO 200 °C.

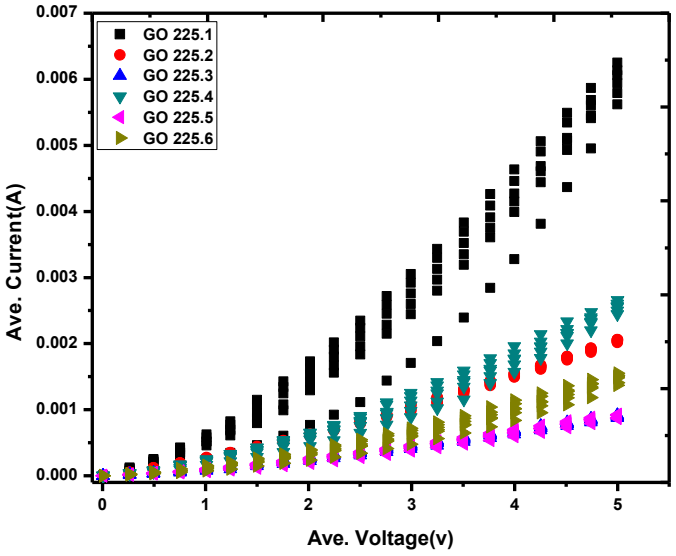

Fig. A1 (e). I-V In-plane test GO 225 °C.

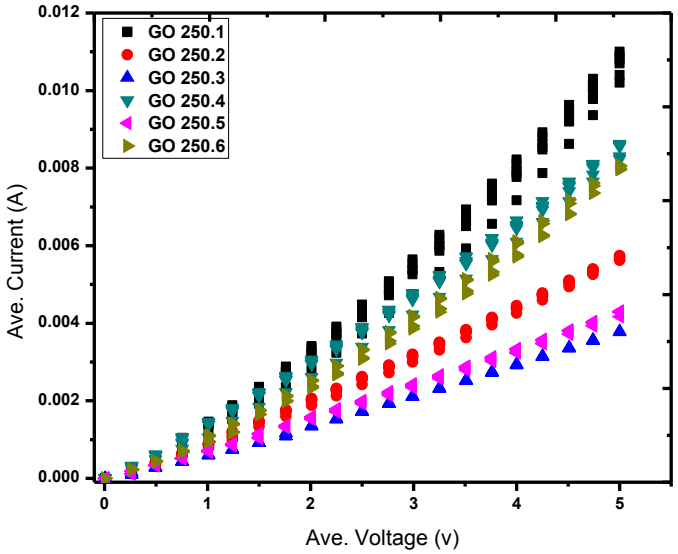

Fig. A1 (f). I-V In-plane test GO 250 °C.

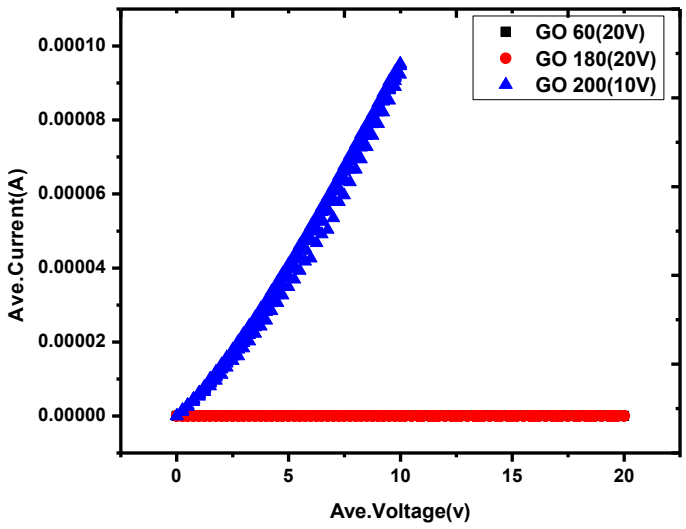

Fig. A2 (a). I-V In-plane plot of GO 60 °C, GO 180 °C, and GO 200 °C at 10 V and 20 V.

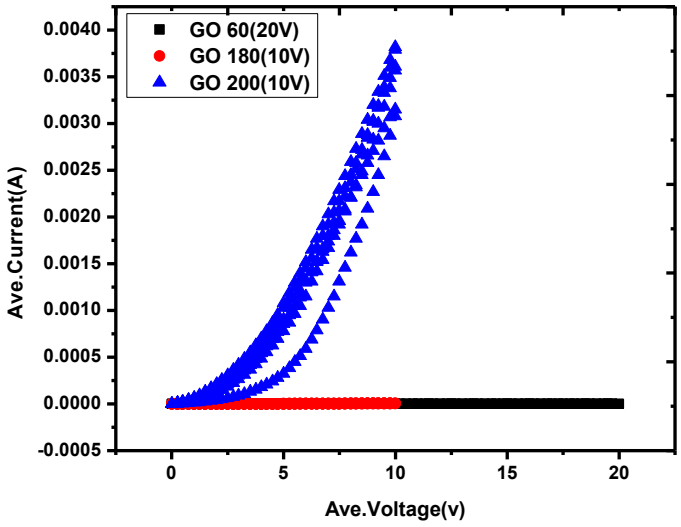

Fig. A2 (b). I-V Out-of-plane plot of GO 60 °C, GO 180 °C, and GO 200 °C at 10 V and 20 V.

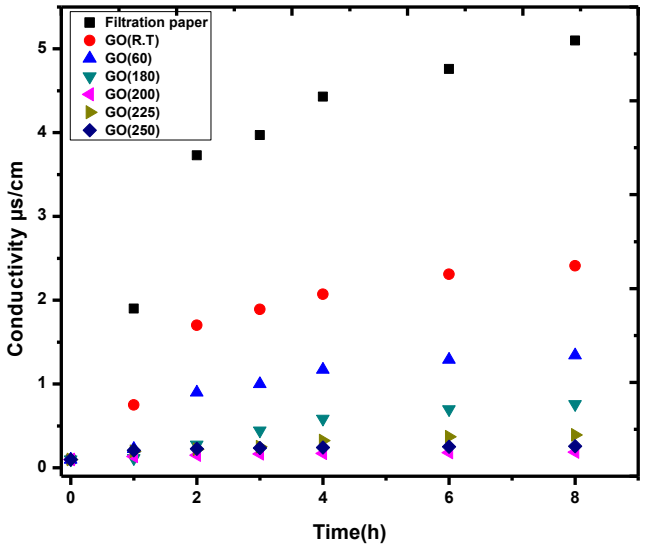

Fig. A3 (a). Diffusion studies for different films of 100 mM NaCl.

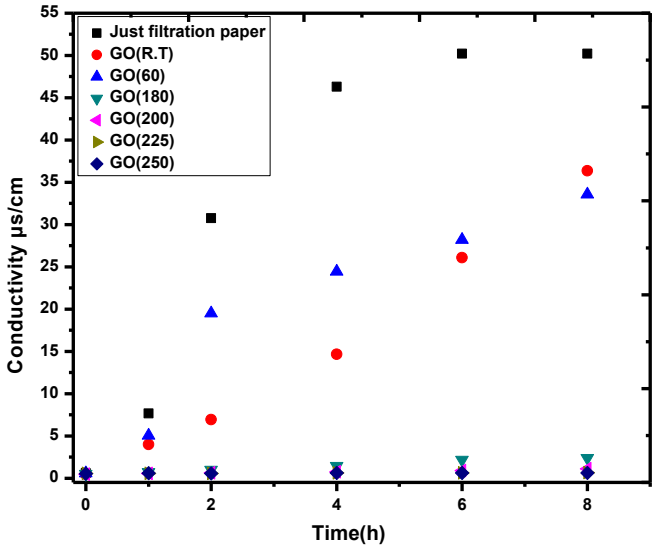

Fig. A3 (b). Diffusion studies for different films of 100 mM NaCl.

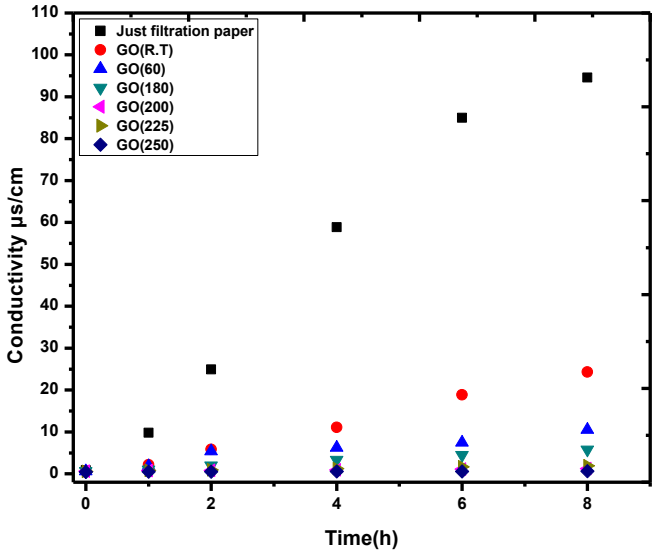

Fig. A3 (c). Diffusion studies for different films of 100 mM $CaCl_2$.

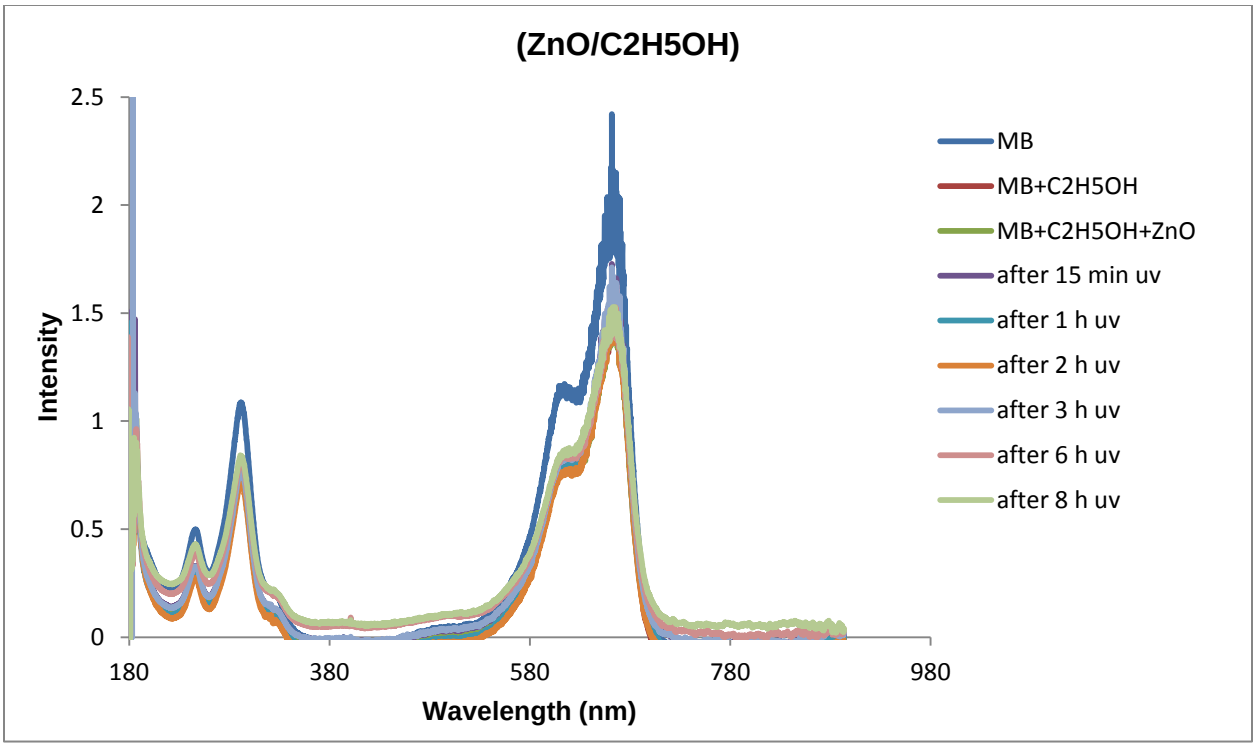

Fig. A4 (a). ZnO/C_2H_5OH.

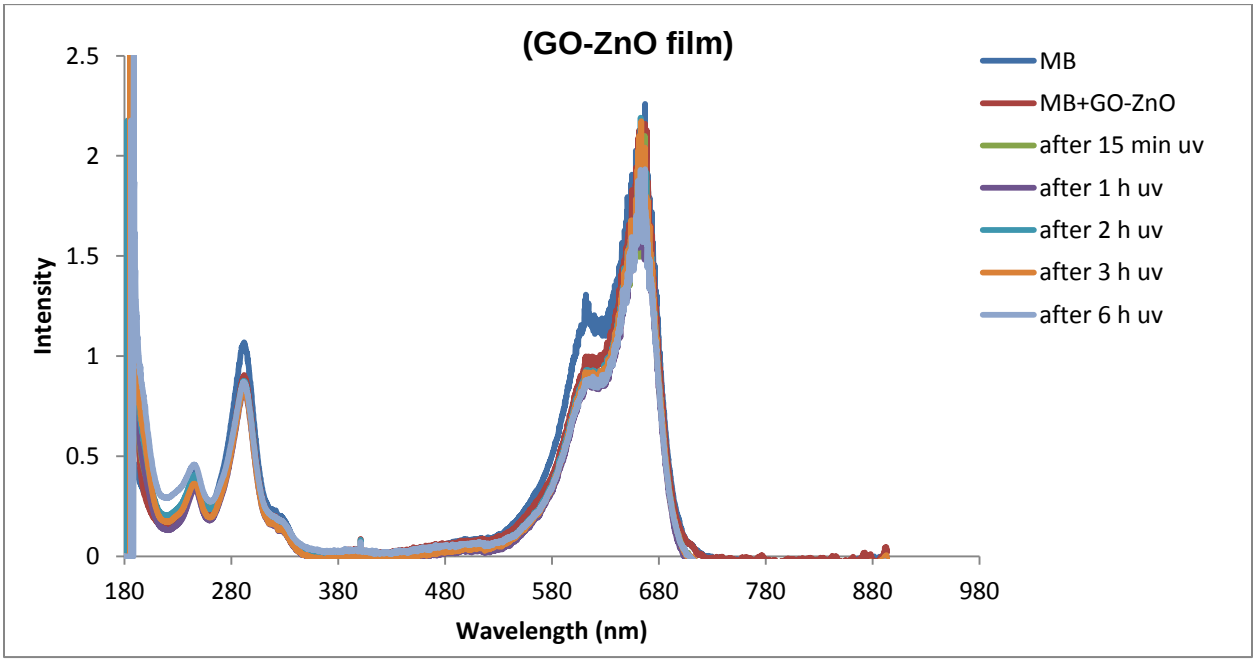

Fig. A4 (b). GO-ZnO film.

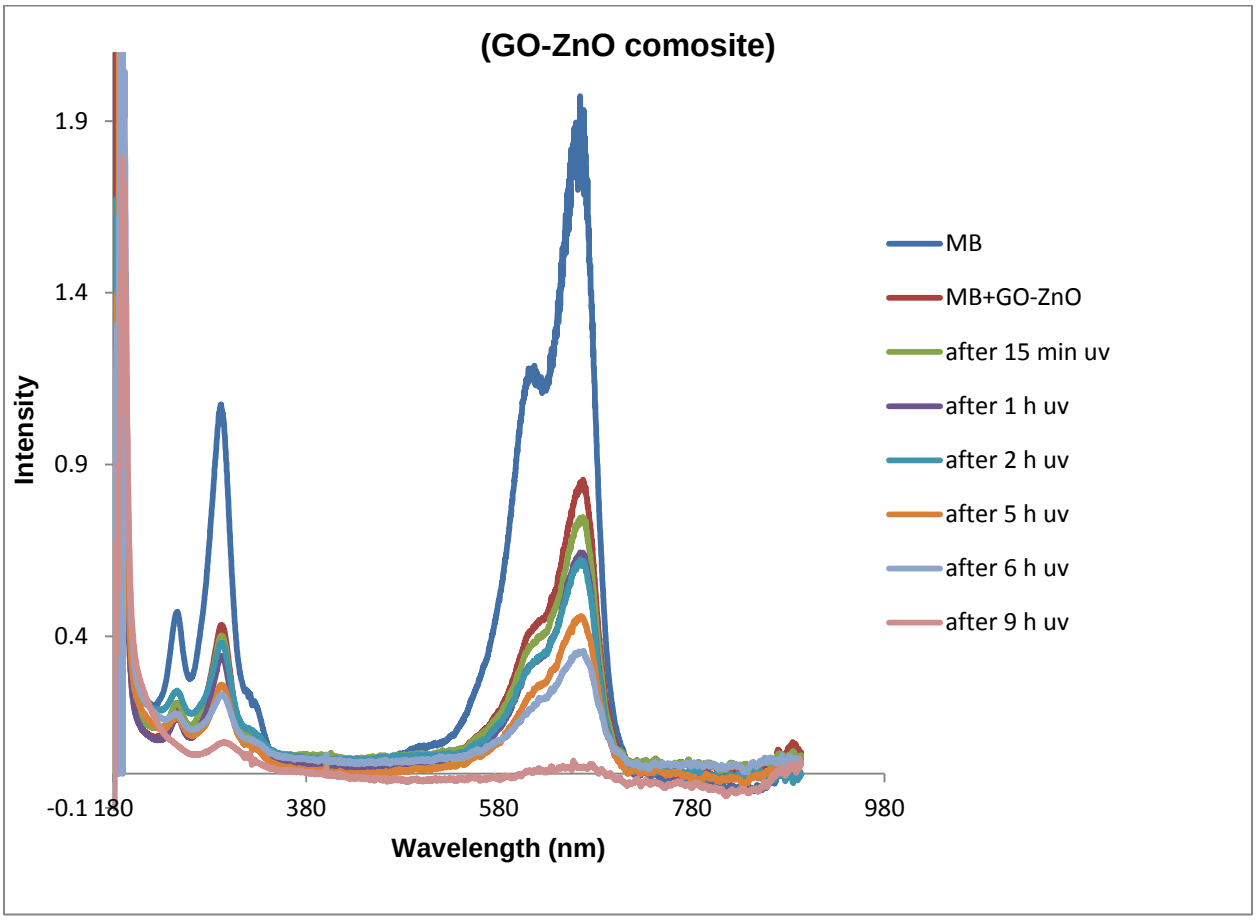

Fig. A4 (c). GO-ZnO composite.

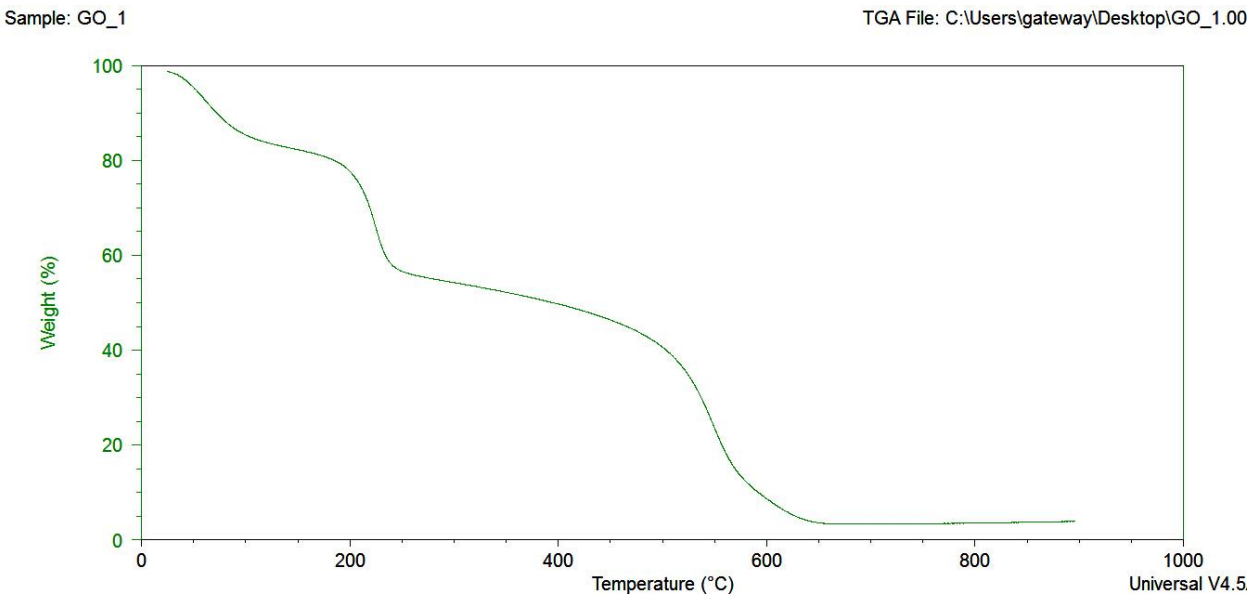

Fig. A5. TG of graphene oxide (GO).

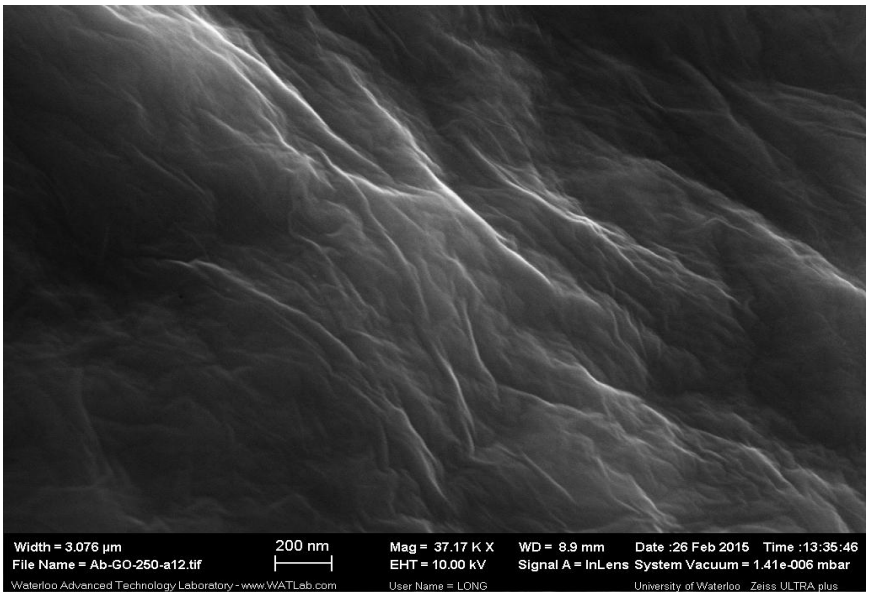

Fig. A6. (a). SEM of GO film 250 °C.

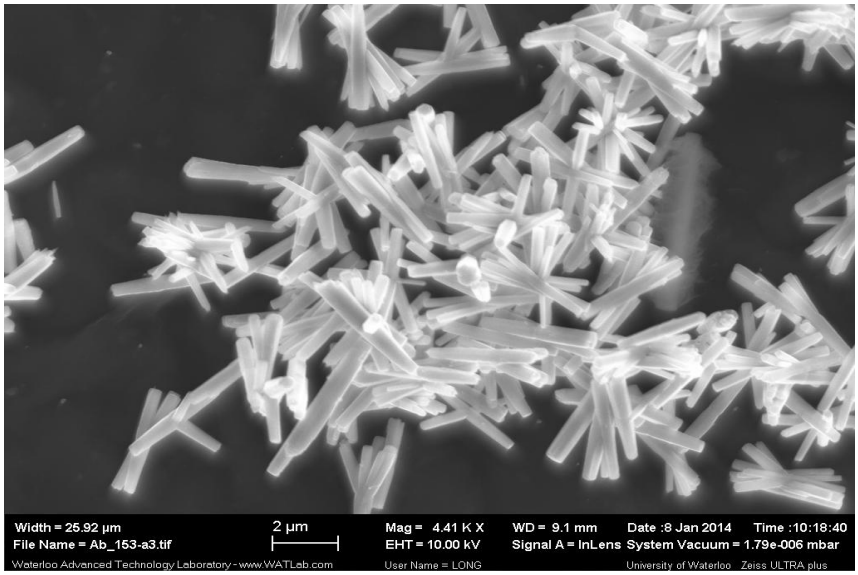

Fig. A6. (b). SEM of ZnO nanorods grown on GO film.

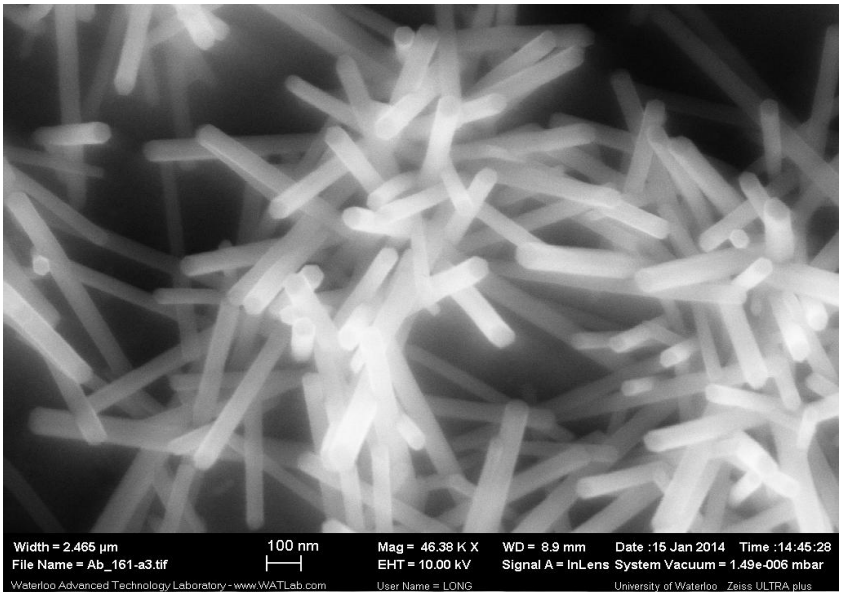

Fig. A6. (c). SEM of ZnO nanorods grown on ITO.

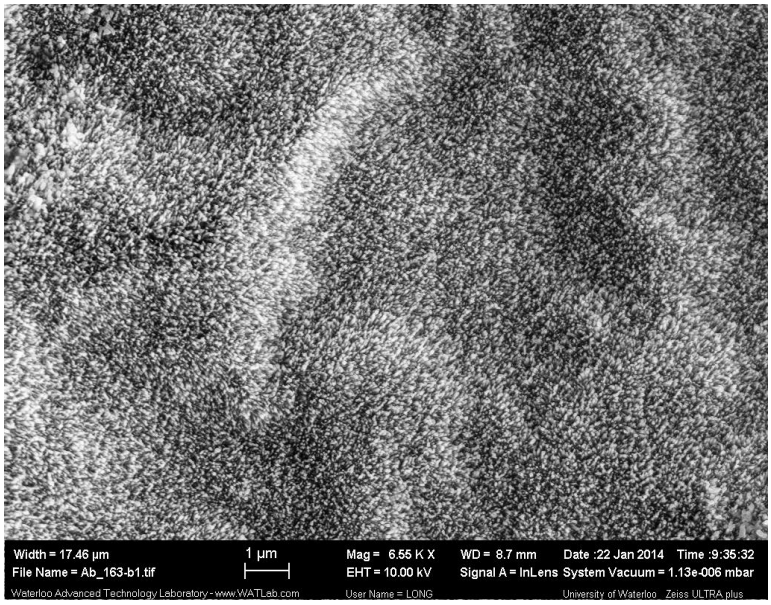

Fig. A6. (d). SEM of growth of ZnO nanorods on GO film.

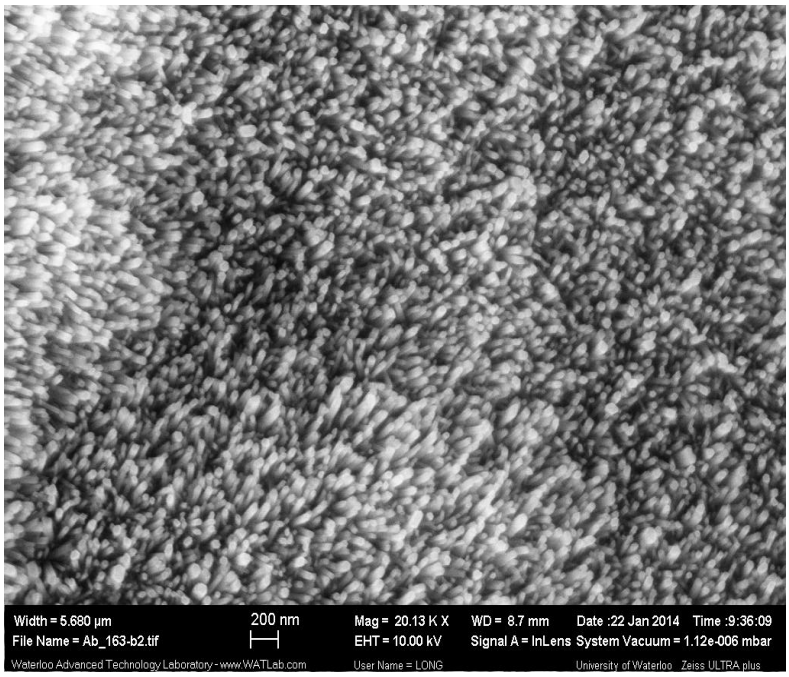

Fig. A6. (e). SEM of growth of ZnO nanorods on GO film.

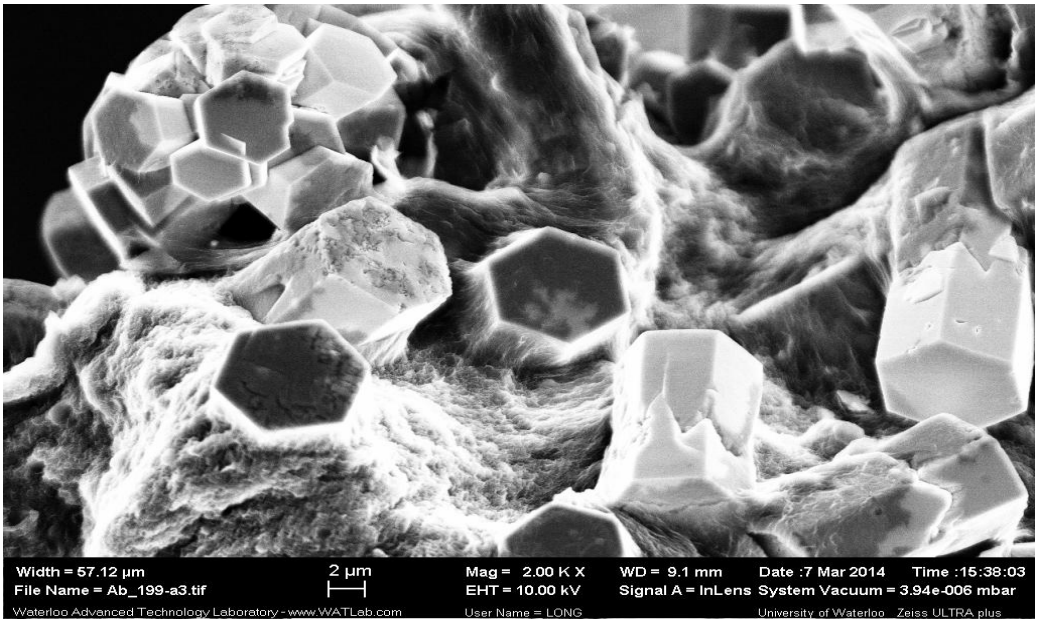

Fig. A6. (f). SEM of the synthesized ZnO nanorods in-situ in graphene oxide crosslinked by magnesium ions.

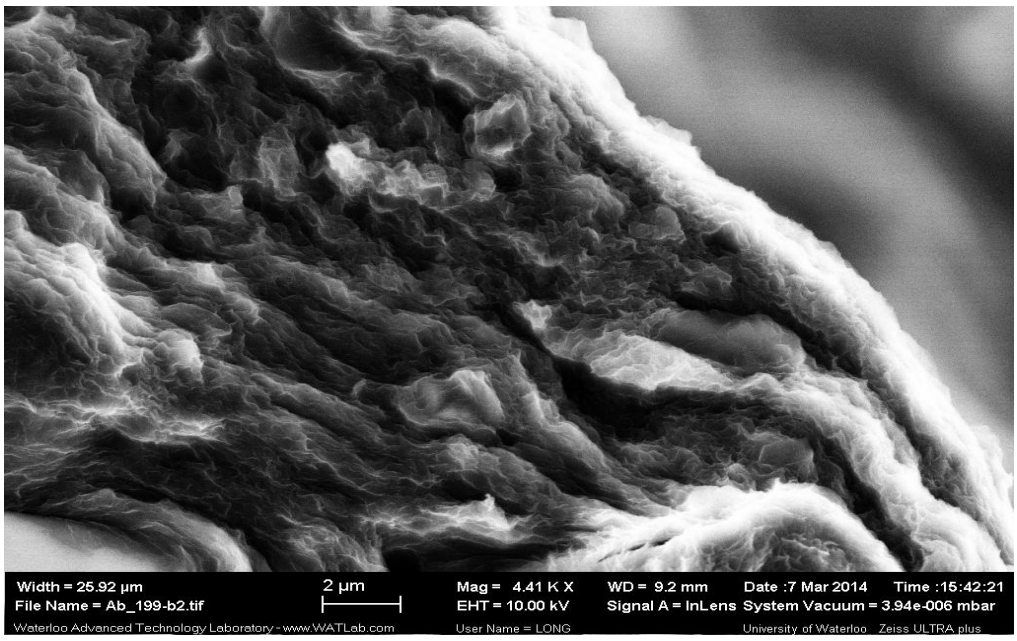

Fig. A6. (j). SEM of the cross-linked layers of graphene oxide by magnesium ions.

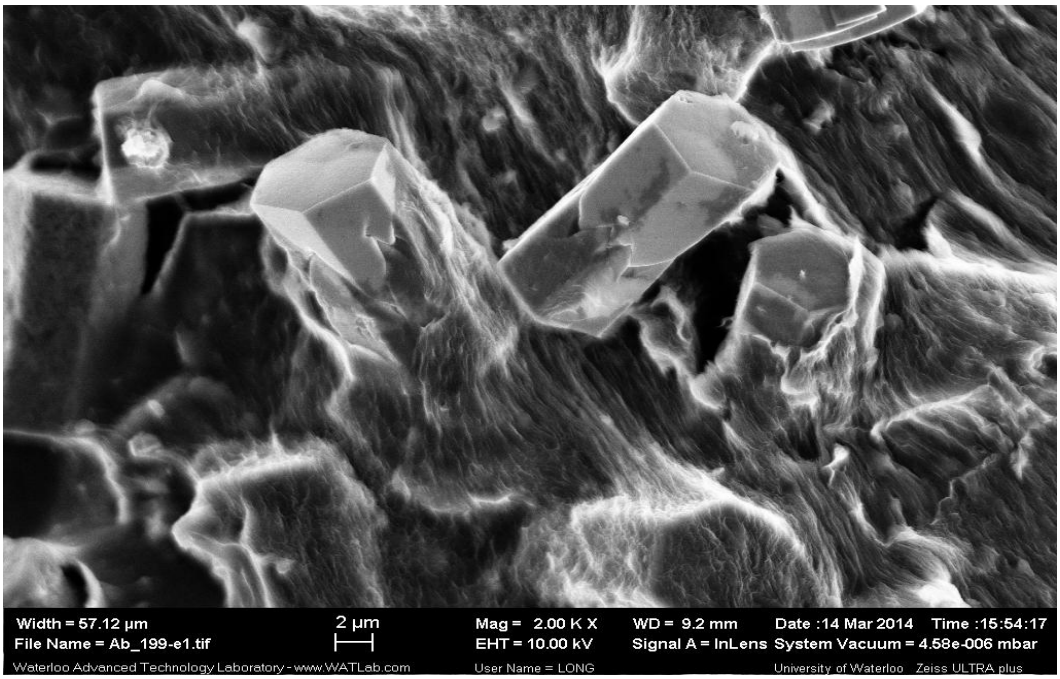

Fig. A6. (h). SEM of ZnO nanorods wrapped with graphene oxide.

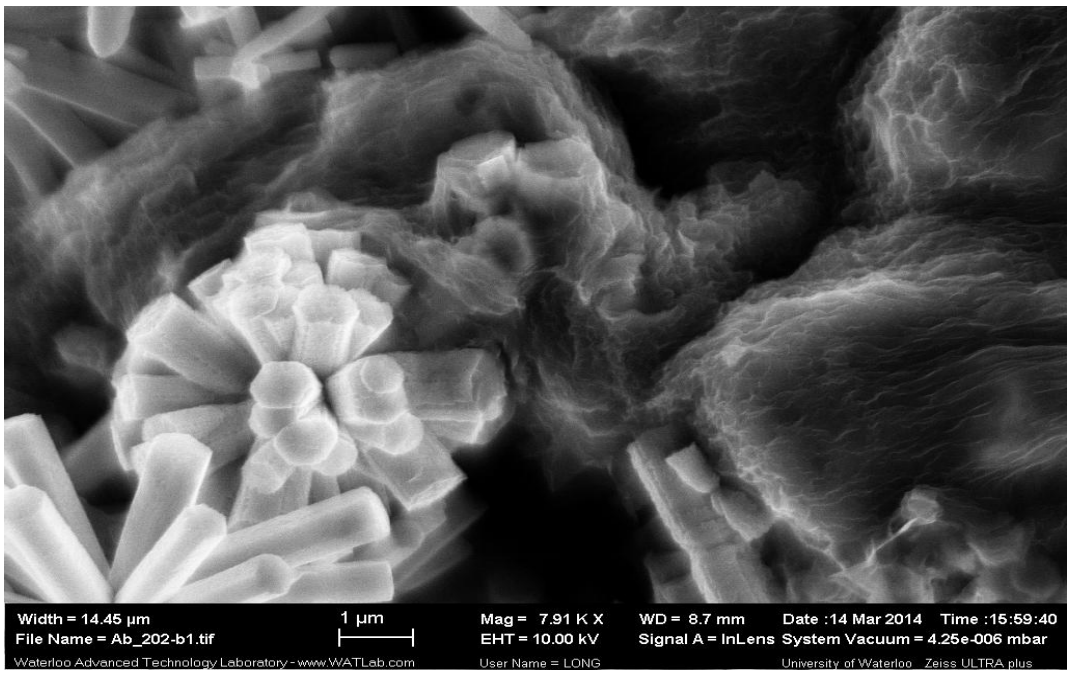

Fig. A6. (i). SEM of ZnO nanorods and cross-linked graphene oxide layers.

Title: Structure of Graphite Oxide Revisited

Author: Anton Lerf, Heyong He, Michael Forster, et al

Publication: The Journal of Physical Chemistry B

Publisher: American Chemical Society

Date: Jun 1, 1998

PERMISSION/LICENSE IS GRANTED FOR YOUR ORDER AT NO CHARGE

This type of permission/license, instead of the standard Terms & Conditions, is sent to you because no fee is being charged for your order. Please note the following:

- Permission is granted for your request in both print and electronic formats, and translations.
- If figures and/or tables were requested, they may be adapted or used in part.
- Please print this page for your records and send a copy of it to your publisher/graduate school.
- Appropriate credit for the requested material should be given as follows: "Reprinted (adapted) with permission from (COMPLETE REFERENCE CITATION). Copyright (YEAR) American Chemical Society." Insert appropriate information in place of the capitalized words.
- One-time permission is granted only for the use specified in your request. No additional uses are granted (such as derivative works or other editions). For any other uses, please submit a new request.

If credit is given to another source for the material you requested, permission must be obtained from that source.

BACK CLOSE WINDOW

Title: A new structural model for graphite oxide

Author: Heyong He,Jacek Klinowski,Michael Forster,Anton Lerf

Publication: Chemical Physics Letters

Publisher: Elsevier

Date: 24 April 1998

Review Order

Please review the order details and the associated terms and conditions. To edit billing or contact information please click on 'account info' at the top of this page.

Licensed content publisher	Elsevier
Licensed content publication	Chemical Physics Letters
Licensed content title	A new structural model for graphite oxide
Licensed content author	Heyong He,Jacek Klinowski,Michael Forster,Anton Lerf
Licensed content date	24 April 1998
Licensed content volume number	287
Licensed content issue number	1-2
Number of pages	4
Type of Use	reuse in a thesis/dissertation
Portion	figures/tables/illustrations
Number of figures/tables/illustrations	1
Format	both print and electronic
Are you the author of this Elsevier article?	No
Will you be translating?	No
Original figure numbers	Fig. 4 (a)
Title of your thesis/dissertation	Synthesis, Fabrication of Graphene Oxide Membranes, and Controlling Their Diffusion by Thermal Reduction
Expected completion date	Feb 2016
Estimated size (number of pages)	153
Elsevier VAT number	GB 494 6272 12
Permissions price	0.00 CAD
VAT/Local Sales Tax	0.00 CAD / 0.00 GBP
Total	0.00 CAD

Edit Order Details

☑ I agree to these terms and conditions.

☐ I understand this license is for reuse only and that obtaining the content is a separate transaction not involving RightsLink.

Customer Code (if supplied) APPLY

BACK DECLINE ACCEPT

Title: The chemistry of graphene oxide
Author: Daniel R. Dreyer,Sungjin Park,Christopher W. Bielawski,Rodney S. Ruoff
Publication: Chemical Society Reviews
Publisher: Royal Society of Chemistry
Date: Nov 3, 2009

Order Completed

Thank you for your order.

This Agreement between Abdulrahman Alhadhrami ("You") and Royal Society of Chemistry ("Royal Society of Chemistry") consists of your license details and the terms and conditions provided by Royal Society of Chemistry and Copyright Clearance Center.

Your confirmation email will contain your order number for future reference.

Get the printable license.

License Number	3803100448303
License date	Feb 06, 2016
Licensed Content Publisher	Royal Society of Chemistry
Licensed Content Publication	Chemical Society Reviews
Licensed Content Title	The chemistry of graphene oxide
Licensed Content Author	Daniel R. Dreyer,Sungjin Park,Christopher W. Bielawski,Rodney S. Ruoff
Licensed Content Date	Nov 3, 2009
Licensed Content Volume	39
Licensed Content Issue	1
Type of Use	Thesis/Dissertation
Requestor type	academic/educational
Portion	figures/tables/images
Number of figures/tables/images	1
Distribution quantity	3
Format	print and electronic
Will you be translating?	no
Order reference number	None
Title of the thesis/dissertation	Synthesis, Fabrication of Graohene Oxide Membranes, and Controlling Their Diffusion by Thermal Reduction
Expected completion date	Feb 2016
Estimated size	153
Requestor Location	Abdulrahman Alhadhrami H2-265 Lawrence Ave. Kitchener, ON N2M 5R1 Canada

	Attn: Abdulrahman Alhadhrami
Billing Type	Invoice
Billing address	Abdulrahman Alhadhrami H2-265 Lawrence Ave. Kitchener, ON N2M 5R1 Canada Attn: Abdulrahman Alhadhrami
Total	0.00 CAD

ORDER MORE CLOSE WINDOW

Title:	Chemical methods for the production of graphenes
Author:	Sungjin Park and Rodney S. Ruoff
Publication:	Nature Nanotechnology
Publisher:	Nature Publishing Group
Date:	Mar 29, 2009

Review Order

Please review the order details and the associated terms and conditions.

Licensed content publisher	Nature Publishing Group
Licensed content publication	Nature Nanotechnology
Licensed content title	Chemical methods for the production of graphenes
Licensed content author	Sungjin Park and Rodney S. Ruoff
Licensed content date	Mar 29, 2009
Type of Use	reuse in a dissertation / thesis
Volume number	4
Issue number	4
Requestor type	academic/educational
Format	print and electronic
Portion	figures/tables/illustrations
Number of figures/tables/illustrations	1
High-res required	no
Figures	Chemical structure of graphite oxide (Lerf model)
Author of this NPG article	no
Your reference number	None
Title of your thesis / dissertation	Synthesis, Fabrication of Graphene Oxide Films, and Controlling Their Diffusion by Thermal Reduction
Expected completion date	Feb 2016
Estimated size (number of pages)	153
Total	0.00 CAD

Edit Order Details

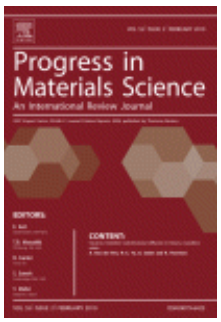

Title:	Graphene based materials: Past, present and future
Author:	Virendra Singh,Daeha Joung,Lei Zhai,Soumen Das,Saiful I. Khondaker,Sudipta Seal
Publication:	Progress in Materials Science
Publisher:	Elsevier
Date:	October 2011

Published by Elsevier Ltd.

Review Order

Please review the order details and the associated terms and conditions. To edit billing or contact information please click on 'account info' at the top of this page.

Licensed content publisher	Elsevier
Licensed content publication	Progress in Materials Science
Licensed content title	Graphene based materials: Past, present and future
Licensed content author	Virendra Singh,Daeha Joung,Lei Zhai,Soumen Das,Saiful I. Khondaker,Sudipta Seal
Licensed content date	October 2011
Licensed content volume number	56
Licensed content issue number	8
Number of pages	94
Type of Use	reuse in a thesis/dissertation
Portion	figures/tables/illustrations
Number of figures/tables/illustrations	1
Format	both print and electronic
Are you the author of this Elsevier article?	No
Will you be translating?	No
Original figure numbers	a.Oxidation of graphite to graphene oxide and reduction to reduced graphene oxide. b. A proposed reaction pathway for reduction of epoxide by hydrazine.
Title of your thesis/dissertation	Synthesis, Fabrication of Graphene Oxide Membranes, and Controlling Their Diffusion by Thermal Reduction
Expected completion date	Feb 2016
Estimated size (number of pages)	153
Elsevier VAT number	GB 494 6272 12
Permissions price	0.00 CAD
VAT/Local Sales Tax	0.00 CAD / 0.00 GBP
Total	0.00 CAD

Edit Order Details

☑ I agree to these terms and conditions.

☐ I understand this license is for reuse only and that obtaining the content is a separate transaction not involving RightsLink.

Customer Code (if supplied) APPLY

BACK DECLINE ACCEPT

Title: Synthesis of graphene-based nanosheets via chemical reduction of exfoliated graphite oxide

Author: Sasha Stankovich,Dmitriy A. Dikin,Richard D. Piner,Kevin A. Kohlhaas,Alfred Kleinhammes,Yuanyuan Jia,Yue Wu,SonBinh T. Nguyen,Rodney S. Ruoff

Publication: Carbon

Publisher: Elsevier

Date: June 2007

Review Order

Please review the order details and the associated terms and conditions. To edit billing or contact information please click on 'account info' at the top of this page.

Licensed content publisher	Elsevier
Licensed content publication	Carbon
Licensed content title	Synthesis of graphene-based nanosheets via chemical reduction of exfoliated graphite oxide
Licensed content author	Sasha Stankovich,Dmitriy A. Dikin,Richard D. Piner,Kevin A. Kohlhaas,Alfred Kleinhammes,Yuanyuan Jia,Yue Wu,SonBinh T. Nguyen,Rodney S. Ruoff
Licensed content date	June 2007
Licensed content volume number	45
Licensed content issue number	7
Number of pages	8
Type of Use	reuse in a thesis/dissertation
Portion	figures/tables/illustrations
Number of figures/tables/illustrations	1
Format	both print and electronic
Are you the author of this Elsevier article?	No
Will you be translating?	No
Original figure numbers	The C-1s XPS spectra of: (a) graphene oxide. (b) hydrazine hydrate-reduced graphene oxide.
Title of your thesis/dissertation	Synthesis, Fabrication of Graphene Oxide Membranes, and Controlling Their Diffusion by Thermal Reduction
Expected completion date	Feb 2016
Estimated size (number of pages)	153
Elsevier VAT number	GB 494 6272 12
Permissions price	0.00 CAD
VAT/Local Sales Tax	0.00 CAD / 0.00 GBP
Total	0.00 CAD

Edit Order Details

☑ I agree to these terms and conditions.

I understand this license is for reuse only and that obtaining the content is a separate transaction not involving RightsLink.

Customer Code (if supplied) APPLY

BACK DECLINE ACCEPT

Title:	Water desalination: Graphene cleans up water
Author:	Evelyn N. Wang, Rohit Karnik
Publication:	Nature Nanotechnology
Publisher:	Nature Publishing Group
Date:	Sep 5, 2012

Review Order

Please review the order details and the associated terms and conditions.

Licensed content publisher	Nature Publishing Group
Licensed content publication	Nature Nanotechnology
Licensed content title	Water desalination: Graphene cleans up water
Licensed content author	Evelyn N. Wang, Rohit Karnik
Licensed content date	Sep 5, 2012
Type of Use	reuse in a dissertation / thesis
Volume number	7
Issue number	9
Requestor type	academic/educational
Format	print and electronic
Portion	figures/tables/illustrations
Number of figures/tables/illustrations	1
High-res required	no
Figures	Fig. nanoporous graphene membranes.
Author of this NPG article	no
Your reference number	None
Title of your thesis / dissertation	Synthesis, Fabrication of Graohene Oxide Membranes, and Controlling Their Diffusion by Thermal Reduction
Expected completion date	Feb 2016
Estimated size (number of pages)	153
Total	0.00 CAD

Edit Order Details

I agree to these terms and conditions.

I understand this license is for reuse only and that obtaining the content is a separate transaction not involving Rightslink.

Customer Code (if supplied) APPLY

BACK DECLINE ACCEPT

Please click accept only once.

Comments? We would like to hear from you. E-mail us at customercare@copyright.com

Title: Water Desalination across Nanoporous Graphene

Author: David Cohen-Tanugi, Jeffrey C. Grossman

Publication: Nano Letters

Publisher: American Chemical Society

Date: Jul 1, 2012

PERMISSION/LICENSE IS GRANTED FOR YOUR ORDER AT NO CHARGE

This type of permission/license, instead of the standard Terms & Conditions, is sent to you because no fee is being charged for your order. Please note the following:

- Permission is granted for your request in both print and electronic formats, and translations.
- If figures and/or tables were requested, they may be adapted or used in part.
- Please print this page for your records and send a copy of it to your publisher/graduate school.
- Appropriate credit for the requested material should be given as follows: "Reprinted (adapted) with permission from (COMPLETE REFERENCE CITATION). Copyright (YEAR) American Chemical Society." Insert appropriate information in place of the capitalized words.
- One-time permission is granted only for the use specified in your request. No additional uses are granted (such as derivative works or other editions). For any other uses, please submit a new request.

If credit is given to another source for the material you requested, permission must be obtained from that source.

Science AAAS

Title:	Unimpeded Permeation of Water Through Helium-Leak–Tight Graphene-Based Membranes
Author:	R. R. Nair,H. A. Wu,P. N. Jayaram,I. V. Grigorieva,A. K. Geim
Publication:	Science
Publisher:	The American Association for the Advancement of Science
Date:	Jan 27, 2012

Order Completed

Thank you very much for your order.

This is a License Agreement between Abdulrahman Alhadhrami ("You") and The American Association for the Advancement of Science ("The American Association for the Advancement of Science"). The license consists of your order details, the terms and conditions provided by The American Association for the Advancement of Science, and the payment terms and conditions.

Get the printable license.

License Number	3811490916695
License date	Feb 17, 2016
Licensed content publisher	The American Association for the Advancement of Science
Licensed content publication	Science
Licensed content title	Unimpeded Permeation of Water Through Helium-Leak–Tight Graphene-Based Membranes
Licensed content author	R. R. Nair,H. A. Wu,P. N. Jayaram,I. V. Grigorieva,A. K. Geim
Licensed content date	Jan 27, 2012
Volume number	335
Issue number	6067
Type of Use	Thesis / Dissertation
Requestor type	Scientist/individual at a research institution
Format	Print and electronic
Portion	Figure
Number of figures/tables	1
Order reference number	None
Title of your thesis / dissertation	Synthesis, Fabrication of Graohene Oxide Membranes, and Controlling Their Diffusion by Thermal Reduction
Expected completion date	Feb 2016
Estimated size(pages)	153
Total	0.00 CAD

ORDER MORE... CLOSE WINDOW

Title: Selective Ion Passage through Functionalized Graphene Nanopores

Author: Kyaw Sint, Boyang Wang, Petr Král

Publication: Journal of the American Chemical Society

Publisher: American Chemical Society

Date: Dec 1, 2008

PERMISSION/LICENSE IS GRANTED FOR YOUR ORDER AT NO CHARGE

This type of permission/license, instead of the standard Terms & Conditions, is sent to you because no fee is being charged for your order. Please note the following:

- Permission is granted for your request in both print and electronic formats, and translations.
- If figures and/or tables were requested, they may be adapted or used in part.
- Please print this page for your records and send a copy of it to your publisher/graduate school.
- Appropriate credit for the requested material should be given as follows: "Reprinted (adapted) with permission from (COMPLETE REFERENCE CITATION). Copyright (YEAR) American Chemical Society." Insert appropriate information in place of the capitalized words.
- One-time permission is granted only for the use specified in your request. No additional uses are granted (such as derivative works or other editions). For any other uses, please submit a new request.

If credit is given to another source for the material you requested, permission must be obtained from that source.

Title: Creating New Types of Carbon-Based Membranes
Author: Donald R. Paul
Publication: Science
Publisher: The American Association for the Advancement of Science
Date: Jan 27, 2012

Order Completed

Thank you very much for your order.

This is a License Agreement between Abdulrahman Alhadhrami ("You") and The American Association for the Advancement of Science ("The American Association for the Advancement of Science"). The license consists of your order details, the terms and conditions provided by The American Association for the Advancement of Science, and the payment terms and conditions.

Get the printable license.

License Number	3802811139725
License date	Feb 05, 2016
Licensed content publisher	The American Association for the Advancement of Science
Licensed content publication	Science
Licensed content title	Creating New Types of Carbon-Based Membranes
Licensed content author	Donald R. Paul
Licensed content date	Jan 27, 2012
Volume number	335
Issue number	6067
Type of Use	Thesis / Dissertation
Requestor type	Scientist/individual at a research institution
Format	Print and electronic
Portion	Figure
Number of figures/tables	1
Order reference number	None
Title of your thesis / dissertation	Synthesis, Fabrication of Graohene Oxide Membranes, and Controlling Their Diffusion by Thermal Reduction
Expected completion date	Feb 2016
Estimated size(pages)	153
Total	0.00 CAD

ORDER MORE... CLOSE WINDOW

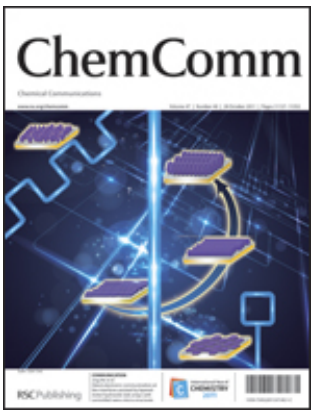

Title: Facile, mild and fast thermal-decomposition reduction of graphene oxide in air and its application in high-performance lithium batteries

Author: Zhong-li Wang,Dan Xu,Yun Huang,Zhong Wu,Li-min Wang,Xin-bo Zhang

Publication: Chemical Communications (Cambridge)

Publisher: Royal Society of Chemistry

Date: Nov 24, 2011

Title:	Photocatalytic degradation of organic dyes in the presence of nanostructured titanium dioxide: Influence of the chemical structure of dyes
Author:	A.R. Khataee,M.B. Kasiri
Publication:	Journal of Molecular Catalysis A: Chemical
Publisher:	Elsevier
Date:	3 August 2010

Order Completed

Thank you very much for your order.

This is a License Agreement between Abdulrahman Alhadhrami ("You") and Elsevier ("Elsevier"). The license consists of your order details, the terms and conditions provided by Elsevier, and the payment terms and conditions.

Get the printable license.

License Number	3814840680203
License date	Feb 23, 2016
Licensed content publisher	Elsevier
Licensed content publication	Journal of Molecular Catalysis A: Chemical
Licensed content title	Photocatalytic degradation of organic dyes in the presence of nanostructured titanium dioxide: Influence of the chemical structure of dyes
Licensed content author	A.R. Khataee,M.B. Kasiri
Licensed content date	3 August 2010
Licensed content volume number	328
Licensed content issue number	1-2
Number of pages	19
Type of Use	reuse in a thesis/dissertation
Portion	figures/tables/illustrations
Number of figures/tables/illustrations	1
Format	both print and electronic
Are you the author of this Elsevier article?	No
Will you be translating?	No
Original figure numbers	Fig.2 General mechanism of the photocatalysis on TiO2 nanoparticles
Title of your thesis/dissertation	Synthesis, Fabrication of Graohene Oxide Membranes, and Controlling Their Diffusion by Thermal Reduction
Expected completion date	Feb 2016
Estimated size (number of pages)	153
Elsevier VAT number	GB 494 6272 12
Permissions price	0.00 CAD
VAT/Local Sales Tax	0.00 CAD / 0.00 GBP
Total	0.00 CAD

Comments? We would like to hear from you. E-mail us at customercare@copyright.com

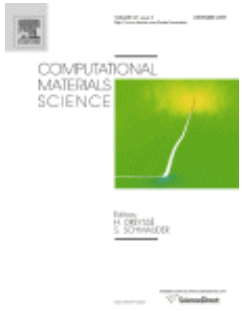

Title: Structure prediction of titania phases: Implementation of Darwinian versus Lamarckian concepts in an Evolutionary Algorithm

Author: S.M. Woodley,C.R.A. Catlow

Publication: Computational Materials Science

Publisher: Elsevier

Date: March 2009

Order Completed

Thank you very much for your order.

This is a License Agreement between Abdulrahman Alhadhrami ("You") and Elsevier ("Elsevier"). The license consists of your order details, the terms and conditions provided by Elsevier, and the payment terms and conditions.

Get the printable license.

License Number	3811540189999
License date	Feb 17, 2016
Licensed content publisher	Elsevier
Licensed content publication	Computational Materials Science
Licensed content title	Structure prediction of titania phases: Implementation of Darwinian versus Lamarckian concepts in an Evolutionary Algorithm
Licensed content author	S.M. Woodley,C.R.A. Catlow
Licensed content date	March 2009
Licensed content volume number	45
Licensed content issue number	1
Number of pages	12
Type of Use	reuse in a thesis/dissertation
Portion	figures/tables/illustrations
Number of figures/tables/illustrations	3
Format	both print and electronic
Are you the author of this Elsevier article?	No
Will you be translating?	No
Original figure numbers	Fig. 1 (d) brookite. Fig. 9 (f) rutile. Fig. 10 (a) anatase.
Title of your thesis/dissertation	Synthesis, Fabrication of Graohene Oxide Membranes, and Controlling Their Diffusion by Thermal Reduction
Expected completion date	Feb 2016
Estimated size (number of pages)	153
Elsevier VAT number	GB 494 6272 12
Permissions price	0.00 CAD
VAT/Local Sales Tax	0.00 CAD / 0.00 GBP
Total	0.00 CAD

ORDER MORE... CLOSE WINDOW

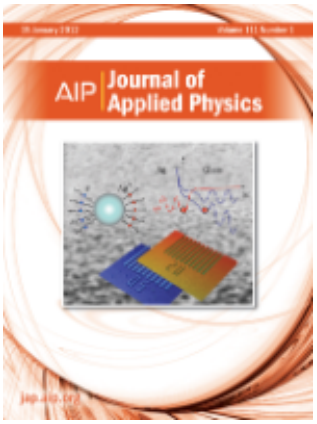

Title:	A comprehensive review of ZnO materials and devices
Author:	Ü. Özgür,Ya. I. Alivov,C. Liu, et al.
Publication:	Journal of Applied Physics
Volume/Issue	98/4
Publisher:	AIP Publishing LLC
Date:	Aug 30, 2005
Page Count:	103

Order Completed

Thank you very much for your order.

Click here for Payment Terms and Conditions.

Get a printable version for your records.

License Number	3803140118980
Order Date	Feb 06, 2016
Publisher	AIP Publishing LLC
Publication	Journal of Applied Physics
Article Title	A comprehensive review of ZnO materials and devices
Author	Ü. Özgür,Ya. I. Alivov,C. Liu, et al.
Online Publication Date	Aug 30, 2005
Volume number	98
Issue number	4
Type of Use	Thesis/Dissertation
Requestor type	Student
Format	Print and electronic
Portion	Figure/Table
Number of figures/tables	1
Title of your thesis / dissertation	Synthesis, Fabrication of Graohene Oxide Membranes, and Controlling Their Diffusion by Thermal Reduction
Expected completion date	Feb 2016
Estimated size (number of pages)	153
Total	0.00 CAD

ORDER MORE... CLOSE WINDOW

nature publishing group

Title:	Materials for electrochemical capacitors
Author:	Patrice Simon and Yury Gogotsi
Publication:	Nature Materials
Publisher:	Nature Publishing Group
Date:	Nov 1, 2008

Order Completed

Thank you very much for your order.

This is a License Agreement between Abdulrahman Alhadhrami ("You") and Nature Publishing Group ("Nature Publishing Group"). The license consists of your order details, the terms and conditions provided by Nature Publishing Group, and the payment terms and conditions.

Get the printable license.

License Number	3803140857675
License date	Feb 06, 2016
Licensed content publisher	Nature Publishing Group
Licensed content publication	Nature Materials
Licensed content title	Materials for electrochemical capacitors
Licensed content author	Patrice Simon and Yury Gogotsi
Licensed content date	Nov 1, 2008
Type of Use	reuse in a dissertation / thesis
Volume number	7
Issue number	11
Requestor type	academic/educational
Format	print and electronic
Portion	figures/tables/illustrations
Number of figures/tables/illustrations	1
High-res required	no
Figures	A Ragone plot (power vs specific energy) for various electrical energy storage devices.
Author of this NPG article	no
Your reference number	None
Title of your thesis / dissertation	Synthesis, Fabrication of Graohene Oxide Membranes, and Controlling Their Diffusion by Thermal Reduction
Expected completion date	Feb 2016
Estimated size (number of pages)	153
Total	0.00 CAD

ORDER MORE... CLOSE WINDOW

Title:	Materials for electrochemical capacitors
Author:	Patrice Simon and Yury Gogotsi
Publication:	Nature Materials
Publisher:	Nature Publishing Group
Date:	Nov 1, 2008

Order Completed

Thank you very much for your order.

This is a License Agreement between Abdulrahman Alhadhrami ("You") and Nature Publishing Group ("Nature Publishing Group"). The license consists of your order details, the terms and conditions provided by Nature Publishing Group, and the payment terms and conditions.

Get the printable license.

License Number	3803150322189
License date	Feb 06, 2016
Licensed content publisher	Nature Publishing Group
Licensed content publication	Nature Materials
Licensed content title	Materials for electrochemical capacitors
Licensed content author	Patrice Simon and Yury Gogotsi
Licensed content date	Nov 1, 2008
Type of Use	reuse in a dissertation / thesis
Volume number	7
Issue number	11
Requestor type	academic/educational
Format	print and electronic
Portion	figures/tables/illustrations
Number of figures/tables/illustrations	1
High-res required	no
Figures	Fig. 2 (e) Cyclic voltammetry of a two-electrode laboratory EDLC cell.
Author of this NPG article	no
Your reference number	None
Title of your thesis / dissertation	Synthesis, Fabrication of Graohene Oxide Membranes, and Controlling Their Diffusion by Thermal Reduction
Expected completion date	Feb 2016
Estimated size (number of pages)	153
Total	0.00 CAD

ORDER MORE... CLOSE WINDOW

Title: Evolution of Surface Functional Groups in a Series of Progressively Oxidized Graphite Oxides

Author: Tamás Szabó, Ottó Berkesi, Péter Forgó, et al

Publication: Chemistry of Materials

Publisher: American Chemical Society

Date: May 1, 2006

PERMISSION/LICENSE IS GRANTED FOR YOUR ORDER AT NO CHARGE

This type of permission/license, instead of the standard Terms & Conditions, is sent to you because no fee is being charged for your order. Please note the following:

- Permission is granted for your request in both print and electronic formats, and translations.
- If figures and/or tables were requested, they may be adapted or used in part.
- Please print this page for your records and send a copy of it to your publisher/graduate school.
- Appropriate credit for the requested material should be given as follows: "Reprinted (adapted) with permission from (COMPLETE REFERENCE CITATION). Copyright (YEAR) American Chemical Society." Insert appropriate information in place of the capitalized words.
- One-time permission is granted only for the use specified in your request. No additional uses are granted (such as derivative works or other editions). For any other uses, please submit a new request.

If credit is given to another source for the material you requested, permission must be obtained from that source.

BACK CLOSE WINDOW

Title: Graphene Oxide Papers Modified by Divalent Ions—Enhancing Mechanical Properties via Chemical Cross-Linking

Author: Sungjin Park, Kyoung-Seok Lee, Gulay Bozoklu, et al

Publication: ACS Nano

Publisher: American Chemical Society

Date: Mar 1, 2008

PERMISSION/LICENSE IS GRANTED FOR YOUR ORDER AT NO CHARGE

This type of permission/license, instead of the standard Terms & Conditions, is sent to you because no fee is being charged for your order. Please note the following:

- Permission is granted for your request in both print and electronic formats, and translations.
- If figures and/or tables were requested, they may be adapted or used in part.
- Please print this page for your records and send a copy of it to your publisher/graduate school.
- Appropriate credit for the requested material should be given as follows: "Reprinted (adapted) with permission from (COMPLETE REFERENCE CITATION). Copyright (YEAR) American Chemical Society." Insert appropriate information in place of the capitalized words.
- One-time permission is granted only for the use specified in your request. No additional uses are granted (such as derivative works or other editions). For any other uses, please submit a new request.

If credit is given to another source for the material you requested, permission must be obtained from that source.

BACK CLOSE WINDOW

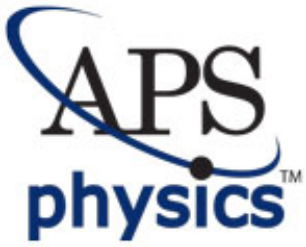

Title: The electronic properties of graphene
Author: A. H. Castro Neto et al.
Publication: Reviews of Modern Physics
Publisher: American Physical Society
Date: Jan 14, 2009

Order Completed

Thank you for your order.

This Agreement between Abdulrahman Alhadhrami ("You") and American Physical Society ("American Physical Society") consists of your license details and the terms and conditions provided by American Physical Society and Copyright Clearance Center.

Your confirmation email will contain your order number for future reference.

Get the printable license.

License Number	3802791281797
License date	Feb 05, 2016
Licensed Content Publisher	American Physical Society
Licensed Content Publication	Reviews of Modern Physics
Licensed Content Title	The electronic properties of graphene
Licensed Content Author	A. H. Castro Neto et al.
Licensed Content Date	Jan 14, 2009
Licensed Content Volume	81
Type of use	Thesis/Dissertation
Requestor type	Student
Format	Print, Electronic
Portion	image/photo
Number of images/photos requested	2
Portion description	Fig. 2 (a) Honeycomb lattice. (b) Reciprocal lattice vectors. Fig. 3 Electronic dispersion in the honeycomb lattice.
Rights for	Main product
Duration of use	Life of Current Edition
Creation of copies for the disabled	no
With minor editing privileges	no
For distribution to	Worldwide
In the following language(s)	Original language of publication
With incidental promotional use	yes
Lifetime unit quantity of new product	0 to 499
The requesting person/organization	Abdulrahman Alhadhrami
Order reference number	None

Title of your thesis / dissertation	Synthesis, Fabrication of Graohene Oxide Membranes, and Controlling Their Diffusion by Thermal Reduction
Expected completion date	Feb 2016
Expected size (number of pages)	153
Requestor Location	Abdulrahman Alhadhrami H2-265 Lawrence Ave. Kitchener, ON N2M 5R1 Canada Attn: Abdulrahman Alhadhrami
Billing Type	Invoice
Billing address	Abdulrahman Alhadhrami H2-265 Lawrence Ave. Kitchener, ON N2M 5R1 Canada Attn: Abdulrahman Alhadhrami
Total	0.00 CAD

ORDER MORE CLOSE WINDOW

WILEY

Book: Membrane Technology and Applications, Third Edition
Chapter: Overview of Membrane Science and Technology
Author: Richard W. Baker
Publisher: John Wiley and Sons
Date: Jul 18, 2012

Order Completed

Thank you for your order.

This Agreement between Abdulrahman Alhadhrami ("You") and John Wiley and Sons ("John Wiley and Sons") consists of your license details and the terms and conditions provided by John Wiley and Sons and Copyright Clearance Center.

Your confirmation email will contain your order number for future reference.

Get the printable license.

License Number	3802800367600
License date	Feb 05, 2016
Licensed Content Publisher	John Wiley and Sons
Licensed Content Publication	Wiley oBooks
Licensed Content Title	Overview of Membrane Science and Technology
Licensed Content Author	Richard W. Baker
Licensed Content Date	Jul 18, 2012
Licensed Content Pages	14
Type of use	Dissertation/Thesis
Requestor type	University/Academic
Format	Print and electronic
Portion	Figure/table
Number of figures/tables	2
Original Wiley figure/table number(s)	Fig. Schematic diagram of the principal types of membranes. Fig. The nominal pore size and the best theoretical model for the principal membrane separation processes.
Will you be translating?	No
Title of your thesis / dissertation	Synthesis, Fabrication of Graohene Oxide Membranes, and Controlling Their Diffusion by Thermal Reduction
Expected completion date	Feb 2016
Expected size (number of pages)	153
Requestor Location	Abdulrahman Alhadhrami H2-265 Lawrence Ave. Kitchener, ON N2M 5R1 Canada Attn: Abdulrahman Alhadhrami
Billing Type	Invoice
Billing address	Abdulrahman Alhadhrami H2-265 Lawrence Ave.

Kitchener, ON N2M 5R1
Canada
Attn: Abdulrahman Alhadhrami

Total 0.00 CAD

CLOSE WINDOW

Title: Selective Ion Penetration of Graphene Oxide Membranes

Author: Pengzhan Sun, Miao Zhu, Kunlin Wang, et al

Publication: ACS Nano

Publisher: American Chemical Society

Date: Jan 1, 2013

PERMISSION/LICENSE IS GRANTED FOR YOUR ORDER AT NO CHARGE

This type of permission/license, instead of the standard Terms & Conditions, is sent to you because no fee is being charged for your order. Please note the following:

- Permission is granted for your request in both print and electronic formats, and translations.
- If figures and/or tables were requested, they may be adapted or used in part.
- Please print this page for your records and send a copy of it to your publisher/graduate school.
- Appropriate credit for the requested material should be given as follows: "Reprinted (adapted) with permission from (COMPLETE REFERENCE CITATION). Copyright (YEAR) American Chemical Society." Insert appropriate information in place of the capitalized words.
- One-time permission is granted only for the use specified in your request. No additional uses are granted (such as derivative works or other editions). For any other uses, please submit a new request.

If credit is given to another source for the material you requested, permission must be obtained from that source.